STUDIES ON GROWTH, OPTICAL AND ELECTRICAL PROPERTIES OF DOPED AND UNDOPED ZINC OXIDE THIN FILMS

Thesis
Submitted in partial fulfillment of the requirements for the degree of
DOCTOR OF PHILOSOPHY
by
NAGARAJA K. K.

DEPARTMENT OF PHYSICS
NATIONAL INSTITUTE OF TECHNOLOGY KARNATAKA,
SURATHKAL, MANGALORE-575 025
October, 2013

Declaration

by the Ph.D. Research Scholar

I hereby declare that the Research Thesis entitled **Studies on Growth, Optical and Electrical Properties of Doped and Undoped Zinc Oxide Thin Films** which is being submitted to the National Institute of Technology Karnataka, Surathkal in partial fulfillment of the requirements for the award of the **Doctor of Philosophy** in **Physics** is a bonafide report of the research work carried out by me. The material contained in this Research Thesis has not been submitted to any University or Institution for the award of any degree.

NAGARAJA K. K.
(Reg. No: 080834PH08F02)
Department of Physics

Place: NITK-Surathkal
Date:

Certificate

This is to certify that the Research Thesis entitled **Studies on Growth, Optical and Electrical Properties of Doped and Undoped Zinc Oxide Thin Films** submitted by **Nagaraja K. K.** (Register Number: **080834PH08F02**) as the record of the research work carried out by him, is *accepted as the Research Thesis submission* in partial fulfillment of the requirements for the award of degree of **Doctor of Philosophy.**

DR. H. S. NAGARAJA
Research Guide

Chairman-DRPC

Acknowledgments

I would like to express my sincere gratitude to my research guide Dr. H. S. Nagaraja for his guidance, support and encouragement throughout my research work.

I am grateful to National Institute of Technology Karnataka for giving me the opportunity for doing research and Ministry of Human Resource Department (MHRD)-Government of India for awarding research scholarship.

I thank the members of my Research Progress Assessment Committee (RPAC) Dr. B. Ramachandra Bhat and Dr. Ravikiran Kadoli, for their suggestions during every stage of my research work. I also thank HOD, Physics department and all faculty members of the department for their constant support and encouragement.

I sincerely thank Department of Chemistry, Chemical Engineering, Civil Engineering and Materials & Metallurgical Engineering for providing the research facilities whenever I was in need.

I take this opportunity to acknowledge the constant and often exhaustive support and encouragement extended to me by my fiance Pramodini, my parents and all my family members.

Finally, I would like to express my gratitude to my friends, Sanjay, Guru, Sanjith, Ramesh, Jaya, Prasanna, Sreenivas, Shivaraj, Ganesh, Padaki, Aravind, Choudhari, Garuda, Saravan, Santhosh, Venkat, Kishore, Manjunath, Balaji and all research scholars of NITK for their encouragements. Special thanks to Mr. J. Khan, he always helped me in every possible way. I thank everyone who helped me directly or indirectly to finish this work. For sure I would not have been able to come to an end without them and the energy I got from all the activities I could undertake with them.

NAGARAJA K. K.

Abstract

In recent years zinc oxide (ZnO) has attracted the researchers because of its excellent optical and electrical properties. The primary aim of this work is to deposit undoped and doped ZnO thin films by sputtering techniques and to study the structural, optical and electrical properties. The thin films were deposited on glass and quartz substrates at room temperature using DC and RF magnetron sputtering. The studies on the effects of annealing on the structural and third-order nonlinear optical properties of ZnO thin films deposited on quartz substrates has been carried out under cw He-Ne laser irradiation at 633 nm wavelength using z-scan technique. The enhanced nonlinear response of the films was observed with the increase in the annealing temperature. X-ray diffraction (XRD) patterns show the appearance of crystalline phases of SiO_2 at higher annealing temperatures. The appearance of extraneous phase was confirmed by atomic force microscope (AFM) images and optical transmittance spectra. Multiple diffraction rings due to the refractive index change and thermal lensing were observed when the samples were exposed to laser beam. Also, the films exhibited strong optical limiting properties. Transparent conducting aluminum doped zinc oxide (AZO) films were deposited on glass substrates. Variation of stress values and the lattice parameters confirms the presence of Al^{3+} ions in the ZnO matrix. Electrical resistivity of the deposited films was found to be as low as $0.5 \times 10^{-4}\Omega$-cm. XRD patterns of the ZnO/Al/ZnO multilayers show only reflections corresponding to Wurtzite ZnO. The sheet resistance of the multilayers found to decrease with the increase in the Al interlayer thickness. But, the average transmittance in the visible region decreases. The XRD results of manganese doped ZnO (MZO) films deposited using compound targets show the decrease of lattice parameters a and c after doping of Mn into ZnO. The third-order nonlinear optical susceptibility $\chi^{(3)}$ is found to be of the order of 10^{-3} esu for MZO films.

Keywords: ZnO; magnetron sputtering; XRD; TCO; AFM; CW laser; NLO

Contents

List of Tables

List of Figures

List of Abbreviations

XRD : X-ray Diffraction
SEM : Scanning Electron Microscope
EDX : Energy Dispersive X-ray Analysis
DMS : Dilute Magnetic Semiconductors
BMP : Bound Magnetic Polaron
HCP : Hexagonal Close Packed
TTFT : Transparent Thin Film Transistor
TCO : Transparent Conducting Oxide
ICDD : International Centre for Diffraction Data
JCPDS : Joint Committee on Powder Diffraction Standards
RF : Radio Frequency
DC : Direct Current
SAW : Surface Acoustic Wave
UV : Ultra-violet

Nomenclature

d : interplanar spacing

θ : Bragg angle

a, b, c : Lattice parameters

c_{ij} : Elastic coefficients

ϵ_{film} : Film strain

σ_{film} : Film stress

V : Voltage

I : Current

ρ : Resistivity

h : Planck’s constant

ν : Frequency

I_0 : Input intensity

T : Transmittance

T_{max} : Transmittance maximum

T_{min} : Transmittance manimum

α : Absorption coefficient

n : Refractive index

n_2 : Nonlinear refractive index

β : Nonlinear absorption coefficient

$\chi^{(3)}$: Third order optical nonlinearity

E_g : Energy bandgap

E_o : Eurbach energy

z_R : Rayleigh length

Chapter 1

Introduction

This Chapter presents the introduction of the thesis, which includes overview, objectives and organization of the thesis.

1.1 Overview

Inventions of semiconductor transistor by the scientists at Bell Labs lead to the enormous growth of semiconductor industry since 4-5 decades. The need for faster, powerful, smaller devices triggered invention of new materials which can be used for various applications. Although the first semiconducting transistor was made by germanium (Ge), silicon (Si) emerged as the material of choice due to its properties which overcome the problems with Ge. Si continues to be dominating in many applications due its matured fabrication technology. For high power and faster optoelectronics devices, gallium arsenide (GaAs) is the material of choice as it exhibit a wide direct band gap, higher carrier mobility etc. However, for high temperature applications and UV/blue LED applications, both Si and GaAs are not suitable due to lack of physical properties which are needed. It is essential to investigate alternative materials and their growth and processing techniques in order to achieve these devices (Jagadish and Pearton 2006). Wide bandgap semiconductors exhibit inherent properties such as larger bandgap, higher electron mobility and higher breakdown field strength. Therefore, they are suitable for high-power, high-temperature electronic devices and short-wavelength optoelectronics.

ZnO is a wide bandgap semiconductor with a direct bandgap around 3.3 eV. The advantages associated with a large band gap include high-temperature and high-power operation, lower noise generation, higher breakdown voltages, and ability to sustain large electric fields. Its exciton binding energy is 60 meV which is high compared to that of gallium nitride (GaN) (25 meV) and gallium arsenide (GaAs) (4 meV) which are used in many optoelectronics applications. The higher exciton binding energy enhances the luminescence efficiency of light emission. The room-temperature electron Hall mobility in single-crystal ZnO is 200 cm^2 V^{-1}, slightly lower than that of GaN, but ZnO has higher saturation velocity. ZnO is also much more resistant to radiation damage than other common semiconductor materials, such as Si, GaAs, CdS, and even GaN (Look et al. 1999). ZnO can be grown on inexpensive substrate, such as glass, at relatively low temperatures. Recent works shows ferromagnetism in ZnO by doping with transition metal, e.g. Mn, with practical Curie temperatures for spintronic devices (Pearton et al. 2003). One attractive feature of ZnO is the ability to bandgap tuning via divalent substitution on the cation site to form heterostructures. Bandgap energy of ~ 3.0 eV can be achieved by doping with Cd^{2+}, while Mg^{2+} increases the bandgap energy to ~ 4.0 eV (Ozgur et al. 2005).

In recent years zinc oxide (ZnO) is gaining interest because of its excellent optical and electrical properties which are suitable to variety of electronic and optoelectronic applications such as varistors, transparent high-power electronics, surface acoustic wave devices, piezoelectric transducers, chemical and gas sensing and transparent conducting electrodes (Pearton et al. 2008). It has now received increasing attention and recognized as a promising candidate for applications related to its optoelectronic possibilities in the UV range (Sun et al. 2010). Its piezoelectric properties could also allow developing surface acoustic wave (SAW) filters to be integrated in future analog circuits for portable electronics for which there is a strong need. Furthermore, ZnO transparent thin-film transistors (TTFTs) are a recent and important development in the emerging field of transparent electronics. These potential applications have boosted research related to the growth of high quality ZnO thin films by a lot of different techniques.

1.2 Objectives of the Thesis

As a technologically important material, ZnO has attracted many researchers due to its unique properties (semiconducting, piezoelectric, magnetic etc.). One of the key requirements for many of these applications is the doping of ZnO with various elements for enhancing and controlling its electrical and optical properties. The aim of the present work is to grow undoped and doped ZnO thin films and to probe the material properties. The following objectives have been set:

1. To grow ZnO thin films and study the optical and electrical properties.
2. To deposit Al doped ZnO thin films with different dopant concentrations and to deposit multilayered film for TCO (transparent conducting oxide) electrode applications.
3. To deposit Mn doped ZnO thin films with different dopant concentrations.
4. To investigate the optical (linear and nonlinear) properties of the deposited films.
5. To study the effect of annealing temperature on structural and optical properties of ZnO thin films.

1.3 Organization of the Thesis

The thesis is organized as follows:

- Chapter 1 gives the overview and objectives of the thesis.
- Chapter 2 contains a brief introduction to the fundamental properties of ZnO and related materials. A detailed literature survey of experimental and theoretical studies on ZnO thin films is presented. The scope of the present research work is mentioned at the end.
- Chapter 3 gives the brief experimental and theoretical description of the deposition methods. It contains a detailed description of DC and RF sputtering technique which is employed to deposit thin films in the present work. This is followed by a concise description of different characterization techniques, including

optical power limiting and the z-scan technique employed to measure the nonlinear optical properties.

- Chapter 4 begins with a discussion of the optimization of deposition parameters for ZnO thin films using DC and RF magnetron sputtering. Also, it contains studies on the effect on annealing on structural and nonlinear optical properties of undoped ZnO thin films.
- Chapter 5 starts with an overview of transparent conducting oxides and multilayered TCOs and its importance in optoelectronics. The growth of aluminum doped zinc oxide (AZO) transparent conducting thin films deposited by radio frequency (RF) magnetron sputtering employing zinc oxide and aluminum coaxial targets at room temperature and ZnO/Al/ZnO multilayers by simultaneous RF and DC sputtering have been discussed.
- Chapter 6 presents the preparation of manganese doped zinc oxide thin films and the effect of Mn concentration on the properties of ZnO thin films. The chapter also includes the effect of Mn concentration on the optical properties of the deposited thin films.
- Chapter 7 gives the conclusions of the present work. The scope for further research work in this area is also discussed.

Chapter 2

Background and Literature Review

This Chapter gives the basic properties of ZnO and briefly reviews the state of art in the field of growth and properties of ZnO thin films.

2.1 History of Zinc Oxide

Zinc oxide was known for a long time, since it was a by-product of copper smelting. It is one of the most important materials that we come across in our day-to-day lives. Zinc white is used as a pigment in paints and in coatings for paper. Chinese white is a special grade of zinc white used in artists' pigments. One type ZnO called "philosophers wool", prepared in a special type of furnace was used as ointment by many of our ancestors. The Persians used a similar process to make zinc oxide suitable for medical and other purposes.

The modern history of ZnO started in the middle of 18th century with the discovery of new and easy method for preparing it by burning a metallic Zn in air by a German scientist Cramer. The Chinese however used ZnO commercially for several centuries before that. ZnO was used by paint industries as pigment and in ceramic goods due to its whiteness, fine texture and opacity. ZnO in sufficient quantities helped to hasten the development of rubber and protects it from fungi and UV light. Soon after the first radio broadcasting stations started transmitting in the 1920s, ZnO crystals came into popular demand for their semiconductor properties. Using an antenna and a fine copper whisker (cats whisker), the RF signal was rectified at the junction of the wire and the crystal. Research in ZnO intensified in the 1950s and peaked up in the 1970s, then faded as it was not possible to obtain a p-type ZnO, so the interest moved to other structures in the III-V system, such as GaN and GaAs. However, the advent of modern analysis tools enabled more in-depth analysis of ZnO. Combined with the possibility to grow epitaxial layers, quantum wells and nano-rods, this led to a renewed interest in the 1990s. The ultimate goal for now is still p-type doping, which has not been fully achieved and remains controversial.

The applications of zinc oxide powder are numerous, and the principal ones are summarized below. Most applications exploit the reactivity of the oxide as a precursor to other zinc compounds. For material science applications, zinc oxide has high refractive index, high thermal conductivity, binding, antibacterial and UV-protection properties. Consequently, it is added into materials and products including plastics, ceramics, glass, cement, rubber, lubricants, paints, ointments, adhesive, sealants, pigments, foods, batteries, ferrites, fire retardants, etc. In summary, much of our current industries and daily life is critically reliant upon this compound.

2.2 Properties of Zinc Oxide

ZnO crystallizes in Wurtzite structure in normal conditions with the two lattice parameters in the ratio of c/a = 1.633 and belongs to the space group $P6_3mc$. The lattice constants range from 3.2475 to 3.2501 Å for the a-parameter and from 5.2042 to 5.2075 Å for the c-parameter (Lide 1992). The structure is composed of two interpenetrating hexagonal close packed (hcp) lattices. The Zn atoms are tetrahedrally coordinated with four oxygen atoms, where the Zn d-electrons hybridize with the O p-electrons (Figure 2.1). This tetrahedral coordination gives rise to polar symmetry along the hexagonal axis. This polarity is responsible for a number of the properties of ZnO, including its piezoelectricity and spontaneous polarization, and is also a key factor in crystal growth, etching and defect generation. Bonding between the Zn atoms and O atoms is highly ionic, due to the large difference in their electronegative values (1.65 for Zn and 3.44 for O). In an ideal Wurtzite crystal, the axial ratio c/a and the u parameter (which is a

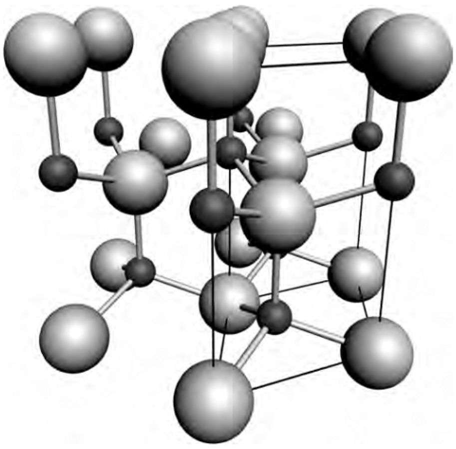

Figure 2.1: Wurtzite structure of ZnO, O atoms are shown as white (large) spheres, Zn atoms as black (small) spheres.

measure of the amount by which each atom is displaced with respect to the next along the c-axis) are correlated by the relationship uc/a = $(3/8)^{1/2}$, where c/a = $(8/3)^{1/2}$, and u = 3/8 for an ideal crystal. ZnO crystals deviate from this ideal arrangement as there is a change in both of these values. This deviation occurs such that the tetrahedral distances are kept roughly constant in the lattice. Experimentally, for Wurtzite ZnO, the real values of u and c/a were determined in the range u = 0.3817-0.3856 and c/a = 1.593-1.6035 (Kisi and Elcombe 1989; Gerward and Olsen 1995). ZnO also crystallizes

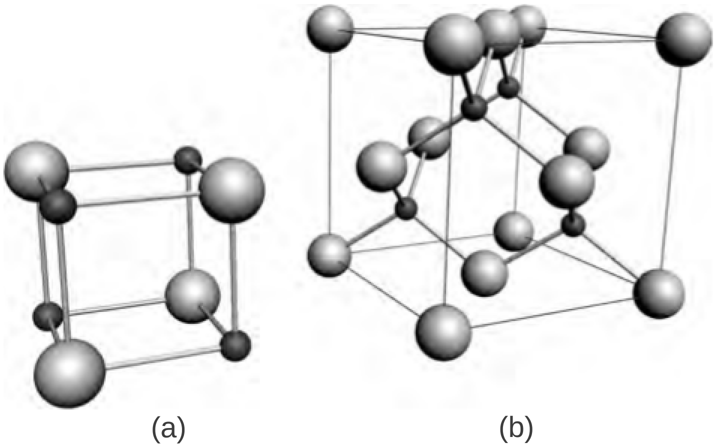

(a) (b)

Figure 2.2: Unit cells of (a) Zinc blende (b) Rock salt structures of ZnO, O atoms are shown as white (large) spheres, Zn atoms as black (small) spheres.

Table 2.1: Properties of Wurtzite ZnO

Property	Value
Lattice parameters	$a_0 = 0.32495\ nm$
	$c_0 = 0.52069\ nm$
	$a_0/c_0 = 0.32495\ nm$
Density	$5.606\ g/cm^3$
Melting point	$1975\ ^0C$
Thermal conductivity	$0.6 - 1.2$
Linear expansion co-efficient	$a_0 : 6.5 \times 10^{-6}$
	$c_0 : 3.0 \times 10^{-6}$
Static dielectric constant	8.565
Refractive index	$2.008 - 2.209$
Energy gap	3.37 eV, direct
Intrinsic carrier concentration	$< \times 10^{16} cm^{-3}$
Exciton binding energy	$60\ meV$
Electron effective mass	0.24
Hole effective mass	0.59
Electon hall mobility	$200\ cm^2/V\ s$
Hole hall mobility	$5 - 50\ cm^2/V\ s$

in other forms as Zinc blend (stable only by growth on cubic structures) and rocksalt (structure is a high-pressure metastable phase forming at ~10 GPa) which are not stable and are seen only in special conditions (Figure 2.2). Undoped ZnO with a Wurtzite structure naturally becomes an n-type semiconductor due to the presence of intrinsic or extrinsic defects, which were generally attributed to native defects, such as the Zn-on-O antisite, the zinc interstitial, and the oxygen vacancy. The highest room-temperature electron mobility for a bulk ZnO single crystal grown by vapor-phase transport method is reported to be about 205 $cm^2V^{-1}s^{-1}$ with a carrier concentration of $6.0 \times 10^{16} cm^{-3}$ (Jagadish and Pearton 2006). ZnO is a relatively soft material, with a hardness of ~5 GPa at a plastic penetration 300 nm. The thermal conductivity (k) of a semiconductor is an important property when considering high-power/high temperature devices. It is a kinetic property influenced by the vibrational, rotational and electronic degrees of freedom, and is predominately limited by phonon-phonon scattering in a pure crystal. ZnO, like most other semiconductors, contains a large number of point defects, and these have a significant effect on the thermal conductivity. The values typically fall in the range 0.6 - 1 W cm^{-1} K^{-1} (Jagadish and Pearton 2006).

Basic physical properties of ZnO are shown in Table 2.1 (Pearton et al. 2004). Some of the values compiled in the table remain uncertain; the disparity originates from the inhomogeneity of the materials. Robust, reproducible p-type ZnO remains elusive, thus the hole mobility and effective masses are still in debate. Crystal defects, such as dislocations, may contribute to variation in thermal conductivity, as observed in GaN.

2.3 Literature review

2.3.1 Growth of ZnO thin films by sputtering

As a technologically important material, ZnO has attracted many researchers due to its unique properties (semiconducting, piezoelectric, magnetic etc.). Many methods were tried to deposit good quality ZnO films such as spin coating, spray pyrolysis, pulsed laser deposition, molecular beam epitaxy, chemical bath deposition, dip coating, sputtering etc. Among all, sputtering technique has several advantages; a) low substrate temperature (down to room temperature); b) good adhesion of films on substrates; c) very good thickness uniformity; d) directive deposition from elemental targets by reactive sputtering in rare/reactive gas mixtures (Hong et al. 2005; Ayadi et al. 2007). Lai and Lee showed that the resistivity of the undoped ZnO films decreased with the increase in working pressure (2009). Obtained films were shown preferred orientation along with c-axis and the deposition rate decreased with the working pressure which is given by Keller-Simmons relation. The decrease in the energy gap with the increase in working pressure is attributed to the decrease in the density of oxygen vacancies and increase in Zn-O bonds. Zhang et al. reported the influence of plasma power on direct current reactively sputtered ZnO films on BK-7 glass substrates (2009). The grain size and RMS roughness value for the films increased with increase in plasma power. Same trend was associated with the band gap of the films. The films deposited under higher plasma power show weaker emission, this may be related with sub stoichiometric composition. Ning et al. showed that the different RF power in sputtering process had different effects on the quality of films in different growth conditions (2009). When the working pressure was low, the quality of the films would increase with the increase in power. But this was not true when the working pressure is high. Crystalline ZnO films with very smooth surface were deposited by off-axis RF magnetron sputtering by Zhu et al. (2000). The resistivity was found to increase drastically when oxygen was introduced with argon. The X-ray diffraction pattern of sputtered films usually show only (0 0 2) peaks indicating a strong preferred orientation. This is because the surface energy density of the (0 0 2) orientation in ZnO crystal is lowest (Major et al. 1983). Grains with lower surface will become larger as the film grows. Then the growth orientation develops into one crystallographic direction of the lowest surface energy.

The structural and optical properties of sputtered films are strongly influenced by gas composition. Lee et al. investigated the changes of structural properties, especially crystallographic orientation and microstructural evolution of ZnO films deposited by RF-magnetron sputtering with different deposition parameters (1996). The properties of the films were profoundly dependent on substrate position, which may be attributed to bombardment of high energetic oxygen species on the growing film surface. As substrate temperature and/or oxygen partial pressure increased, (0 0 2) preferred orientation was significantly reduced and the film had rather mixed orientations. The microstructure of the films was also profoundly modified. With increasing temperature and/or oxygen partial pressure, a fine and smooth texture surface was changed to an elongated faceted textured structure (Lee et al. 1996). With increasing film thickness, preferred orientation was changed from (0 0 2) to (1 0 1), and became (1 1 0) for the film deposited in the region facing the eroded target area. Thus the driving force of orientation development was presumably changed from minimization of surface energy to minimization of energy loss per unit area with increasing thickness. The change of crystallographic orientation is closely related to the modified microstructure (Lee et al. 1996). In case of DC reactive sputtering from elemental targets, the thin films of controllable stoichiometry can be produced. Hong et al. studied the effect of oxygen pressure on structural and emission characteristics of the ZnO thin films deposited by DC reactive sputtering (2005). The results show that the ZnO phase was absent at very low oxygen partial pressure and the structure of the films transforms to single phase Wurtzite structure as the oxygen partial pressure increased. Intensity of visible emission is reduced with the oxygen partial pressure, may be due to the decrease of number of oxygen vacancies and/or Zn interstitials. The films were opaque at low oxygen partial pressure, while transparent for the oxygen concentration more than 40% (Ma et al. 2007). Different post treatments influence on the properties of sputtered ZnO films. The properties were studied after bombarding by a mixture of argon (40%) and oxygen (60%) by a RF source and also by annealing at 700 °C for 8 hours. Both thermal annealing and ion bombardment have the effects of narrowing the diffraction peak, indicating that the grain growth has occurred. Shifting of 2θ values to the higher side is an indication of partial relief from the residual stresses within as treated films (Hong et al. 2005).

2.3.2 Optical properties of ZnO thin films

Jayaraj et al. reported a shift in the absorption edge in off axis RF sputtered ZnO films (2002). The shift is due to increase in carrier concentration and blocking of low energy transitions which causes a Burstain Moss effect, which enhances band gap. Generally, ZnO photoluminescence spectrum consists mainly of two emission bands. One is in ultraviolet (UV) region and corresponds to near-band-edge (NBE) emission which is attributed to exciton states (Kang et al. 2004) and the other one is in visible region and is due to structural defects and impurities (Bagnall et al. 1997). The visible photoluminescence in undoped ZnO films can be controlled with the control in preparation conditions. Wang et al. reported the suppression of visible emission in RF sputtered ZnO by annealing it in N_2 atmosphere (2009). Annealing the same samples in air did not show any suppression. In spite of the complexity in the microstructure of ZnO, great efforts have been made to tune and control the visible photoluminescence of ZnO by modifying the preparation conditions (van Dijiken et al. 2000; Fujihara et al. 2001; Kang et al. 2004). Ahn et al. investigated the photoluminescent properties of RF sputtered ZnO films (2008). The UV emission intensity increases with decrease in the oxygen contents in the gas mixture. The deep level emission in the visible region which is very weak compared to UV emission also shows similar behavior. However the ZnO thin films grown by PLD have showed comparatively strong deep level emission (Im et al. 2000). Zhang et al. observed a red shift in the fundamental absorption edge with the increase of plasma power in DC reactively sputtered ZnO thin films (2009). The intensive UV arises in Ag doped ZnO films after annealing (Kryshtab et al. 2007). Dong et al. found that using low temperature buffer-layer, the surface morphology and the UV emission could be improved greatly without sacrificing the crystallanity of the film (2008). It was ascribed to the stress releasing by using the buffer layers. They also found that ambience during a cooling process to room temperature after the deposition is another important factor to improve the PL properties; namely defect-related PL disappears and the free exciton PL with a sharp width was observed.

2.3.3 Electrical and mangnetic properties

A key requirement for advancing the technological uses of ZnO is improved control of doping Pearton et al. 2004. As grown ZnO thin films were generally n-type and this can be controlled by oxygen partial pressure. The transparent conducting oxide thin films were characterized by their low specific resistivity and high optical transmission. Indium tin oxide is currently, the most commonly used TCO. However, there is much interest in the use of an alternative to ITO, which provide longer environmental stability, larger deposition rate and low cost. ZnO thin films doped with group III elements such as B, Al, Ga, In have been considered as transparent conducting films. Al doped ZnO is a most important material due to its low cost, high conductivity and high transmittance (Venkatachalam et al. 2008). Liu et al. reported the deposition of Al doped ZnO with an oblique target relative to the substrate (2009a). The deposited films had columnar grains. The carrier transport mechanism was Motts variable hopping in the temperature range below 100 K and the thermally activated band conduction above 215 K. Preparation of Al doped ZnO (AZO) films by nano sized aerogel powders was reported by Ben Ayadi et al. (2007). Sol-gel derived aerogel powders were sputtered using a RF power. Lowest resistivity of 1.17 $\times 10^{-5} \Omega-$cm with a carrier concentration of 7.61 $\times 10^{20}$ cm^{-3} was obtained for a nanopowder annealed at 300 °C in O_2 atmosphere. The insertion of undoped ZnO as a buffer layers affected the electrical properties of AZO thin films. Hall mobility, carrier concentration of double layers was increased and resistivity of these double layers was lower than the single layered AZO. The results demonstrated that RF sputtered AZO/i-ZnO layered films are suitable for the application in low cost copper indium gallium selenide (CIGS) solar cells as transparent conductive electrodes (Shi et al. 2010). Deng et al. investigated the effect of Al content on various properties of AZO (2010). Thin films of AZO were deposited using magnetron co-sputtering of Al_2O_3 and ZnO ceramic targets (Deng et al. 2010). EDX results showed that the Al content in the AZO was linearly increased with the RF power to Al_2O_3. The grain size of pure ZnO and AZO films was quite different indicated by FESEM studies. Increase in the Al content in the AZO film resulted in increase in the roughness of the films. The electrical conductivity and mobility of the AZO films increased with Al content upto 4.50 at.%. AZO thin films with good electrical and optical properties can be prepared by nonreactive DC magnetron sputtering at room temperature. As the argon gas pressure increases from 0.6 to 3.0 Pa, the AZO thin films change from polycrystalline to preferred c-axis-orientation. The electrical conductivity and mobility increased with the Al content in the films till 3.0 at. % (Wang et al. 2010). Same behavior was reported in AZO films grown using pulsed laser deposition (PLD) (Venkatachalam et al. 2008). The rapid thermal annealing of the AZO thin films could have a lowest electrical resistivity of 5.1 $\times 10^{-4} \Omega-$cm and a highest optical transmittance of 88.7%. (Wang et al. 2010). Similar results were obtained in spray deposited AZO films (Caglar et al. 2008). The study of ZnO:Al films prepared at higher working pressures reveal that the films with smaller grain size have more grain boundary scattering that lowers the electrical conductivity. Moreover, the chemisorption of oxygen atoms at the surface of ZnO:Al thin films is an another possible factor to affect the resistivity (Bai and Tseng 2009). Jiang and Liu reported the growth of Bi doped ZnO thin films by RF sputtering (2009). Sputtering followed by vacuum annealing at 400 °C for 3 hours resulted in the (1 0 0) oriented films. Ti doped ZnO films showed good optical transmission above 80% and resistivity of the order $8.78\times10^{-4}\Omega-$cm (Jiang et al. 2009). Thin films of AZO single layer, AZO and Ag multilayer such as AZO/Ag/AZO, AZO/Ag/AZO/Ag/AZO structures were reported by Sahu and Huang (2009). E-beam evaporation method was used to develop multilayers on glass substrates. AZO ceramic target and Ag flakes were the source materials for evaporation. The films with three layers (AZO/Ag/AZO) showed optical transmittance as high as 85% and resistivity of the order $10^{-5}\Omega-$cm, five layered coatings were also shown considerable transmittance about 75%. Similar studies were carried out by Lee et al. (2008). They used RF and DC co-sputtering to develop IZO/Al/GZO/ZnO multilayers on glass substrates. The resistivity of the deposited films found to decrease with the % of Al in the films till 2% Al. Further increase in Al concentration resulted in sudden increase of resistivity of films. Yim and Lee studied suitability of ZnO:Ga thin films as a TCO (2007). Ga has several advantages over other dopants. First one of them is that Ga has higher oxidation resistance than Al. Another is that defect generation minimized when ZnO is doped with Ga since the radius of Ga^{3+} (0.062 nm) is close to that of Zn^{2+} (0.060 nm) than that of Al^{3+} (0.053 nm). The third is that it makes less diffusion-related problems since the diffusivity of Ga is lower than that of Al at room temperature. Shin et al.(2009) investigated influence of the substrate temperature on the properties of the Ga doped ZnO (GZO) films grown by PLD.

Some semiconductor materials known as diluted magnetic semiconductors (DMS) combine two interesting properties: semiconducting and magnetic. Many DMS of III-V (GaAs) or II-VI (CdTe) types have been obtained by doping semiconductors with magnetic impurities. But most of them have a very low curie temperature. A theoretical prediction by Dietl et al. demonstrated that the curies temperature can be increased above room temperature in a p-type semiconductor based DMS (2000). The calculations also reveal that the ferromagnetism is stable in a wide band gap semiconductor based DMS. Many encouraging results lead to intensive experimental work on oxide DMS including ZnO (Prellier et al. 2003). The curie temperatures above room temperature can be obtained by the controlled growth of the transition metal doped ZnO. Interesting view point in ZnO based DMS is, forming a transparent ferromagnetic material (Prellier et al. 2003). Theoretical work on ZnO done by Sato and Yoshida showed, using first principle calculations, that doping by 3d transition metal atoms, such as V, Cr, Fe, Co, and Ni, in the ZnO matrix exhibits a ferromagnetic ordering without any additional carrier doping. But, doping with Ti and Cu result in a paramagnetic state (2000). In the case of Mn the ferromagnetic state is induced by hole doping. Many studies were done on transition metal doped ZnO films which are deposited either by radio frequency sputtering, magnetron co sputtering (Elanchezhiyan et al. 2008), pulsed laser deposition using a KrF laser (Jeon et al. 2006) or a sol-gel method (Bhatti et al. 2005). Many reports showed room temperature ferromagnetism in ZnO. Pandey et al. reported synthesis of transparent magnetic semiconductor by incorporating Ni into ZnO (2008). The thin films of Ni:ZnO were prepared by ion beam sputtering which were ferromagnetic, having coercivity (H_c) values 192, 310 and 100 Oe and saturation magnetization (M_s) values of 6.22, 5.32 and 4.73 emu/g at 5, 15 and 300K, respectively. Similar studies were carried out by Yin et al. (2005), Snure et al. (2009) and many others. Most of the work has been concentrated on Mn doped ZnO thin films prepared by different methods (Sharma et al. 2003; Xu et al. 2006; Yan et al. 2007; Jin et al. 2010; Chikoidze et al. 2007; Martin-Gonzalez et al. 2010; Singh et al. 2009; Liu et al. 2009b). Ferromagnetism was observed in many reports at room temperature. Zhang et al. investigated the ferromagnetic behavior in bulk Mn doped ZnO (2005). As sintered bulk pellets show room temperature ferromagnetism. Doping with other transition metals like Cr, Fe, Cu and Co also exhibited ferromagnetism in ZnO (Zhuge et al. 2009; Soumahoro et al. 2010; Zou et al. 2010; Kittilstved et al. 2006). Mandal et al. reported ferromagnetism in nanocrystalline powders of Mn doped ZnO (2006). Recently, Sundaresan and Rao (2009) reported the ferromagnetism in metal oxides is due to surface defects. Almost all inorganic oxides show ferromagnetism when they are in nano scale (Sundaresan and Rao 2009). The group further concluded ferromagnetism as a universal feature of inorganic nanoparticles. The reported ferromagnetism seems to be weak (10^{-4} emu/g) which casts doubts about the origin of magnetism that also include the contamination of samples while handling them. It is possible that the origin of the magnetism in some of these materials may be related to the surface ferromagnetism of nanoparticles associated with the point defects. Ferromagnetism in ZnO is not well understood till now although extensive work has already been carried out. This area may open new vistas in future due to its widespread applications in IC industry.

In summary, the optical, electrical and magnetic properties of ZnO thin films are throughly investigated by the researchers. Doping of transition metal ions has also been tried to improve the properties of ZnO. Although low resistive ZnO films are achieved by doping Al for their use as transparent electrodes, there is a need to develop better techniques to control the dopant's concentration. As Al is one of the easily available and cost effective dopants, further research towards the effective doping of Al for the improvement of the properties of ZnO thin films is highly desirable. Multilayered structures of ZnO, Al and doped ZnO are need to be studied to understand the conduction mechanism in these type of structures. As per as the optical properties are concerned, the nonlinear optical properties of doped ZnO are not explored much.

Chapter 3

Experimental Methods

This Chapter presents a brief introduction to the experimental techniques which are employed in the present work.

3.1 Introduction

Every material is composed of atoms which decide their basic properties. The specialty of the thin films lies in the fact that a material could be deposited in its atomic scale using the technology available. The atoms and free radicals of the materials in their gas phase react with themselves or with other substances at high temperature to condense or deposit on a surface (substrate) relieving their high energies. The material coating thus formed if in the range of few micrometers or less is called a thin film. The thin films possess properties that are completely different from the bulk material and vary according to the deposition conditions and the thickness of the film. These unique properties of thin films have enabled them to be used in various applications such as hard coatings and wear resistant films, optical devices and various other applications.

3.2 Thin Film Deposition

In a general way, for the production of thin films of a certain material, the choice of the deposition technique is normally based on fulfilling the requirements put forth by the sample properties as well on practical limitations such as cost, area of coverage and vacuum requirements. In this study, magnetron sputtering has been employed for depositing the ZnO samples. Numerous thin film deposition techniques are available for the fabrication of electronic devices of oxide semiconductor. The commonality between these techniques is the goal of forming a high-quality thin-film (in terms of optical, electrical, and mechanical properties) onto the desired substrate. However, the details of the source material, material transport mechanisms (from source to substrate), and thin film formation differ for each technique. Within these differences, distinct advantages and disadvantages arise. The processes which interact with the substrate to form a film (e.g., thermal oxidation) are not commonly employed for the fabrication of integrated oxide semiconductor devices, as the substrate typically acts only as a carrier and does not contribute to device functionality. The thin film deposition techniques relevant to the fabrication of oxide semiconductors are discussed below. These techniques can be separated into two categories: vacuum and non-vacuum techniques. Vacuum techniques are performed in a controlled chamber and/or pressure. Thus, films fabricated with vacuum techniques generally have a lower impurity concentration than those fabricated with non-vacuum techniques. Examples of vacuum techniques include evaporation, sputtering, and chemical vapor deposition. The benefit of non-vacuum techniques is minimal capital equipment investment. From this perspective, non-vacuum techniques are generally considered to be low cost. From a manufacturing viewpoint, the cost benefit may be reduced, as many non-vacuum processes can require extended curing cycles, which would reduce throughput. Examples of non-vacuum techniques are spin-coating, printing, chemical methods using suitable precursors etc.

3.2.1 Vacuum deposition techniques

Vacuum techniques can be further sub categorized into physical vapor deposition (PVD) and chemical vapor deposition (CVD). In PVD techniques, atoms or molecules are physically removed from a source material. They are then transported through vacuum and condense onto the substrate to form a thin film. CVD techniques utilize gas-phase chemicals that are transported to the substrate and react to form a thin film. In these processes, the pressure affects the extent of impurity incorporation in growing thin films and transport of atoms from the source to substrate (Wolf and Tauber 2000). Atoms undergo a larger number of collisions as the pressure in the chamber is increased. The mean free path (λ) is the average distance an atom that travels between collisions and is inversely proportional to pressure,

$$\lambda = \frac{1}{\sqrt{2}\pi d_o^2 n} \Longrightarrow \frac{0.05}{P} \tag{3.1}$$

where d_o is the atomic diameter and n is the gas concentration. The simplification of equation 3.1 is obtained assuming that the ambient is air at 300 K and P is pressure (Torr); this results in the mean free path expressed in millimeters.

Thin film deposition by Evaporation Methods

Evaporation is a basic thin film deposition technique which involves heating of a source material such that the vapor pressure (i.e. the equilibrium pressure created by the rate difference of condensed molecules evaporating and vaporized molecules condensing) is greater than 13 mbar (Maissel and Glang 1970). To increase the mean free path of vaporized molecules and reduce the amount of contamination incorporated in the thin-film during deposition, this heating process is typically performed under high vacuum ($< 5 \times 10^{-6}$ mbar). Since the vapor pressure varies for different chemical elements, stoichiometric compounds and alloys can be difficult to fabricate by evaporation. Compensation for this variation can be accomplished by modifying the source material or by using multiple evaporation sources. The complexity of a multicomponent evaporation process is further increased if the differing sticking coefficients of the deposited adatoms are considered.

Thermal evaporation method

In thermal evaporation, a source material is placed in a refractory crucible, boat, or wire basket and heated using an electric current. A crucible composed of an insulating material, such as Al_2O_3, is indirectly heated by placing it in (or on) a conductive element. In contrast, boats and wire baskets (which are often made of W or Mo) are directly heated. Extremely refractory materials cannot be evaporated thermally for multiple reasons: there is a limit to the amount of current that can be sourced, possible cross-contamination from the boat/basket, and possible physical damage to the boat/basket from overheating. For these materials, electron beam evaporation is a possible solution.

Electron beam evaporation (EBE) method

Electron beam evaporation (EBE) utilizes a high energy (5-30 keV) electron beam to heat a source material, which is normally a compressed pellet that has been sintered at high temperature (Maissel and Glang 1970). One requirement for EBE is that the source material be a poor conductor of heat; the beam cannot supply enough energy to offset the heat loss of a source material which is a good conductor of heat. Alternatively, the hearth/pocket which the source sits upon may be insulated when EBE is used to deposit materials that are good conductors of heat. One of the drawbacks for EBE is possible X-ray damage to the deposited thin-film from the electron beam.

3.2.2 Growth of Thin Films by Sputtering

The Sputtering technique is used to deposit the films on substrates of glass and quartz which are cost effective and available easily. Through the application of a negative potential to the targets (creating a voltage between the target material and the grounded substrate plate), the target material is bombarded with ions extracted from an electropositive plasma. A small current is created by the small number of charge carriers initially present in the sputtering gas when the voltage is applied to the electrodes. An increase of the applied negative potential of the target leads to an increase in the current density. This is in part of a result from the creation of a large density of charge carriers, e.g. secondary electrons. The electrons move towards the anode (sample) while an ion flux is generated towards the cathode (target). This behavior continues for voltages up to the breakdown voltage and is named as Townsend discharge region. Once electrical breakdown occurs, the concurrent increased charge-carrier density increases the current density and decreases the electrode voltage. The applied voltage is now so high that the number of Ar^+ ions produced by collisions with a secondary electron is enough to produce another secondary electron. In this way the plasma is self-sustaining (normal discharge region). One of the important parameter is an excess of positive charge carriers in the space near to the negative cathode. This is related to the attraction (repulsion) of the ions (electrons) and leads to a sheath voltage that is about the same as the electrode voltage, V_{CA}. The total difference in a potential between the electrodes is confined to this sheath close to the cathode, which is named the cathode sheath or Crookes dark space. The Ar^+ ions are accelerated through this sheath, gaining an energy of eV_{CA}, and create secondary electrons upon colliding with the target material. The electrons are accelerated back through the Crookes dark space before they ionise or excite the Ar atoms in the negative glow space. Only parts of the cathode area in the low-current end of the normal discharge region are covered by the negative glow discharge space. This coverage increases as the applied voltage is increased until the entire cathode-area is covered, which is the end of the normal discharge region.

A high ion current is necessary in order to have a reasonable sputtering rate, which explains why the abnormal discharge region is used for sputtering. The collision of Ar^+ ions with the target surface causes:

- sputtering of the target material,
- emission of secondary electrons,
- electron capture and backscattering of neutral Ar atoms,
- implantation of Ar^+ ions into the target.

The number of gas atoms between the sample and the cathode should be low allowing the sputtered atoms to arrive at the sample without any major collisions that would redirect the sputtered atoms away from the sample and thus decrease the deposition rate.

A simple sputtering system is based on a cathode (the target) and an anode facing each other (planar diode glow discharge sputter deposition). The target is not only the source of coating material but also the source of secondary electrons sustaining the glow discharge (the target is normally water-cooled). Several factors determine the deposition rate such as: the power density at the target surface, source-substrate distance, working gas pressure, size of the erosion area, and source material. The various factors are interrelated, such as pressure and power density. Consequently, the optimum operating condition is achieved by controlling the parameters to get the maximum power which can be applied to the target without causing cracking, sublimation or melting of the target.

Magnetron Sputtering

In order to increase significantly the ionisation efficiency near the target, magnetic fields are frequently employed for the diode sputtering process (magnetron sputter deposition). Due to the fact that ions are generated relatively far from the target in the conventional planar diode process, the probability for ions to lose their energy to the chamber walls is large. Additionally, the number of primary electrons hitting the anode at high energies without experiencing collisions is increased as the pressure decreases, thus reducing ionisation efficiency. In the magnetron sputter deposition process, an applied magnetic field parallel to the cathode surface forms electron traps and restricts the primary electron motion to the vicinity of the cathode. The magnetic field strength is in the range of a few hundred gauss and consequently, it can influence the plasma electrons but not the ions. The electrons trapped on a given field line can advance across the magnetic field to an anode or walls by making collisions (mainly with gas atoms). As a result, their chances of being lost to the walls or anode without collisions are very little. Due to the higher efficiency of this ionisation procedure, the process can be operated at low pressures (around 1×10^{-3} mbar) with high current densities at low voltages, hence providing high sputtering rates.

RF magnetron sputtering

Conductive materials like metals can be easily deposited by using DC magnetron sputtering. In the case of insulating materials DC sputtering cannot work because positive charge built on the target surface rejects the ion flux and stop the sputtering process. The solution is to quickly reverse the polarity before the positive ions hitting the insulating target generate a positive repulsive charge. Upon polarity reversal, electrons will hit the target and neutralize any previous charge. For this purpose a RF power source with the frequency in the range of 10 MHz is used to sputter. During the first few complete cycles more electrons than ions are collected at each electrode (due to high mobility of an electron), and cause negative charge to buildup on the electrodes. Thus, both electrodes maintain a steady-state DC potential that is negative with respect to plasma voltage, Vp. A positive Vp aids the transport of the slower positive ions and slow down the negative electrode. The induced negative biasing of the target due to RF powering means that continuous sputtering of the target occurs throughout the RF cycle. But it is also means that this occurs at both electrodes. The substrate will be sputtered at the same rate as the target since the voltage drops would be the same at both electrodes for symmetric system. It would thus be very difficult to deposit any material in that way. But smaller electrode requires a higher RF current density to maintain the same total current as the larger electrode. By making the area of the target electrode smaller than the other electrode (substrate), the voltage drop at the target electrode will be much greater than at the other electrode. Therefore almost all the sputtering will occur at the target electrode.

We propose to deposit doped and undoped films of ZnO by sputtering. We propose to use a ceramic target which is prepared by a solid state reaction technique. To deposit films by ceramic target, radio frequency (RF) magnetron sputtering will be used. We also used direct current (DC) magnetron sputtering to obtain films using elemental targets. A combination of RF and DC magnetron sputtering is also proposed. We also prepare the films with different dopant concentration by RF magnetron sputtering using compound targets. The compound targets with required dopant concentration were prepared by solid state reaction technique. The optimization of different parameters has been done to get the good quality films.

3.2.3 Description of the Sputtering System

The sputtering sytstem used in the present work is a home built, versatile and front-loading thin film system for research & development. This system has a RF and DC planar magnetron sources configured in a sputter down geometry. Each source is manufactured by High Vacuum India (HVI), Bangalore, and is designed for a 5 cm target diameter, and has a separate power supply. The targets can have a typical thickness of 2-4 mm. The RF supply include a RF generator with a manual matching network (Omicron Instruments, New Delhi), it operates at a frequency of 13.56 MHz with an output impedance of 50 Ω. DC power supply is provided by HVI, Bangalore. The sources have power ratings of 500 and 1000 watts, respectively. The vacuum necessary

Figure 3.1: The DC and RF sputtering system

for sputtering is generated inside a stainless steel box type chamber. The box chamber allows an easy and smooth operation. A HVI 6 inch diffusion pump and HVI rotary vane pump provide the high vacuum and rough pumping, respectively. A liquid nitrogen cooled cryo-trap and a throttle valve are between the system and the diffusion pump. This system has two separate needle valves for Ar and O_2, which are used to introduce high pure sputter gas into the system. The system consists of one pirani and one penning gauges.

3.2.4 Annealing furnace

The furnace used for this research is a muffle furnace with programmable controller. To achieve good temperature uniformity within the heating zone for a wide temperature range a PID controller was used. The temperature ramping can be programmed.

Figure 3.2: Muffle furnace with programmable temparature controller.

3.2.5 Substrate Cleaning

Soda-lime float glass and quartz were used as the substrates for the deposited films. The glass substrates were purchased from Polar Scientific Corp., Mumbai, India, and were cut into 2.5 cm and 1 cm square pieces from larger sheets. The first step of the procedure of cleaning the substrates involves cleaning with Labolin detergent and double distilled water (DDW). The substrates were scrubbed using a clean room wipe in a manner similar to polishing a specimen. The substrates were rinsed in a spray of DDW water and dried in oven. The substrates were rinsed again in a spray of double distilled water. These glass slides are further cleaned by a solvent, followed by a DDW rinse, followed by a mild acid clean, DDW rinse and blow dry. The solvents can clean oils and organic residues which appear on glass surfaces. Unfortunately, solvents themselves (especially acetone) leave their own residues. This is why a two-solvent method is used. The solvents used were acetone and methanol. After the slides cleaned using solvent, they were then cleaned using hydrochloric acid as it cleans the glass by mildly etching the surface. In this process the slides were dipped in 30% HCl solution for 30 mins. Further, nitric acid is used as it cleans by leeching the ions from within the surface of the glass. In this process the slides were dipped in 30% HNO_3 solution for 30 mins. Finally, the glass substrates were dipped in Aqua Regia (royal etch) a HCl-HNO_3 (3:1) etchant which is used to etch many metals, including gold. In this process the glass substrates were soaked in the bath for 30 minutes. For extra clean surfaces, soaking was continued for several hours. The substrates were finally rinsed in DDW, then dried in oven. The total process takes approximately 50 minutes.

The quartz substrates with sizes 1 cm×1cm were cleaned using laboratory detergent followed by DDW rinse. Further these quartz substrates were cleaned by acetone and methonol. Finally these substrates were dipped in piranha solution (A typical mixture of 3:1 concentrated sulfuric acid to 30% hydrogen peroxide solution) for 30 minutes.

3.3 Characterization Techniques

3.3.1 Electrical Characterization

The measurements were carried out using four point probe technique. A probe head with tungsten carbide tips with a point radius of 0.05 mm, a probe spacing of 2 mm, and a appropriate probe pressure was used for all measurements. The current was supplied by a Keithley model 2400 source meter with a range between 1μA to 100 mA. The voltages were measured by a Keithley model 2000 voltmeter with an input impedance of greater than 1 giga-ohm. Equation 3.2 and 3.3 were used to determine sheet resistance (R_S in units of Ω/sq.) and resistivity (ρ in units of Ω-cm), respectively.

$$R_S = 4.532\frac{V}{I} \tag{3.2}$$

$$\rho = 4.532\frac{Vt}{I} \tag{3.3}$$

Based on the dimensions of the sample and probe head, no geometrical correction factors were applied. The term t is film thickness (cm), and V is the voltage measured at the supplied current (I).

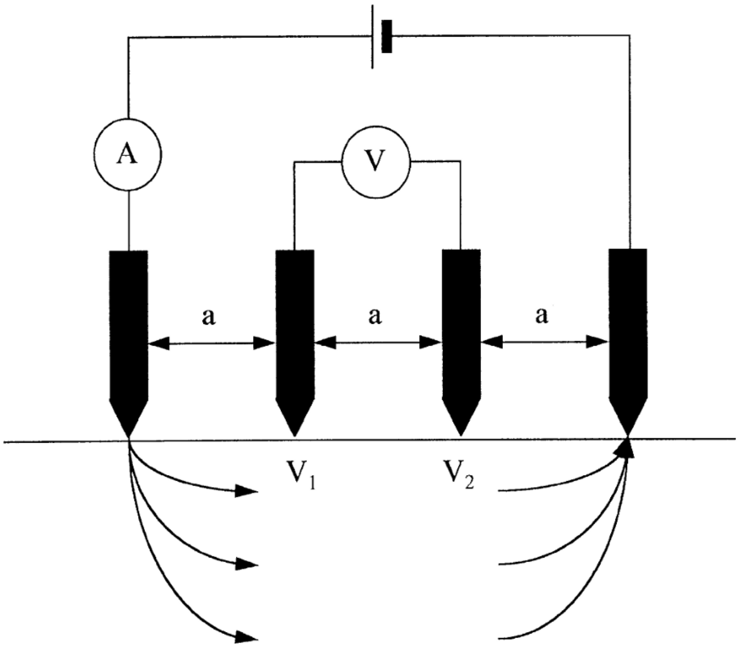

Figure 3.3: Schematic diagram of collinear four point probe method.

3.3.2 X-Ray Diffraction

X-ray diffraction (XRD) is a versatile, non-destructive analytical technique for identification and quantitative determination of the various crystalline compounds, known as 'phases', present in solid materials and powders. Since the wavelength of X-rays (0.5-2.5 Å) is of the same order of magnitude as the interatomic distances in solids, X-rays are frequently used to study the crystalline structure of materials. When X-ray photons interact with electrons, some photons from the incident beam will be deflected away from their original direction and may interfere with each other (3.4). The conditions for constructive interference given by the Bragg law:

$$2\lambda = 2d_{hkl}sin\theta \tag{3.4}$$

where, d$_{hkl}$ is the distance between the lattice planes, λ the X-ray wavelength, θ

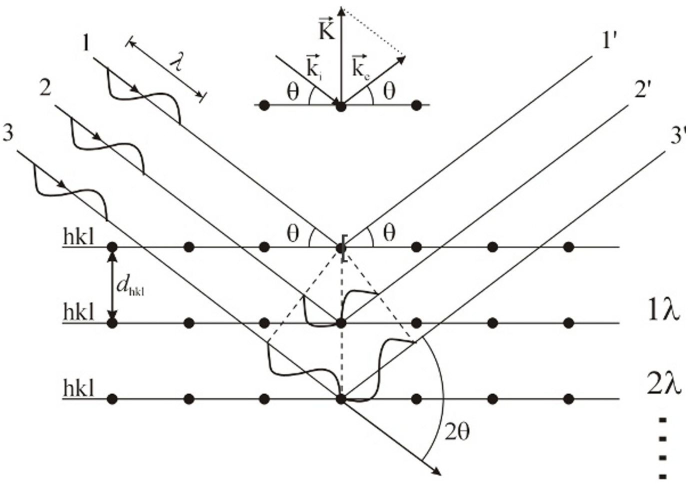

Figure 3.4: Reflection of X-rays from different atomic planes, illustrating Bragg's law. The scattering vector, is defined in the inset

the angle of the incident beam with respect to equidistant (h k l) lattice-planes, and n the order of diffraction. By varying the angle θ, the Braggs law conditions are satisfied by different d-spacings. Plotting the angular positions and intensities of the resultant diffracted peaks forms XRD pattern, which is characteristic of the sample. About 95% of all solid materials can be described as crystalline. When X-rays interact with a crystalline substance (phase), an unique diffraction pattern is received. The X-ray diffraction pattern of a pure substance is, therefore, like a fingerprint of the substance. The powder diffraction method is ideally suited for characterisation and identification of polycrystalline phases. Today about 7,60,000 diffraction patterns of variety of materials have been collected and stored as PDF (powder diffraction file) standards. The main use of powder diffraction is to identify components in a sample by a search/match procedure. Furthermore, the areas under the peak are related to the amount of each phase present in the sample.

3.3.2.1 Powder X-ray Diffractomenter

The essential features of a powder diffractometer are shown in Figure 3.5 (Cullity 1978). A monochromatic radiation is used and the X-ray detector (film or counter) is placed on the circumference of a circle centered on the powder/thin film specimen.

A specimen C, in the form of a flat plate, is supported on a table H, which can be rotated about an axis O perpendicular to the plane of the drawing. The X-ray source S, the line focal spot on the target T of the X-ray tube; S is also normal to the plane of the drawing and therefore parallel to the diffractometer axis O. X-rays diverge from this source and are diffracted by the specimen to form a convergent diffracted beam which comes to a focus at the slit F and then enters the counter G. A and B are special slits which define and collimate the incident and diffracted beams. The filter is usually placed in a special holder (not shown) in the diffracted, rather than the incident, beam; a filter in the diffracted beam not only serves its primary function (suppression of K_β radiation) but also decreases background radiation originating in the specimen. The receiving slits and counter are supported on the carriage E, which may be rotated about the axis O and whose angular position 2θ may be read on the graduated scale K. The supports E and H are mechanically coupled so that a rotation of the counter through 2θ degrees is automatically accompanied by rotation of the specimen through θ degrees. This coupling ensures that the angles of incidence on, and reflection from, the flat specimen

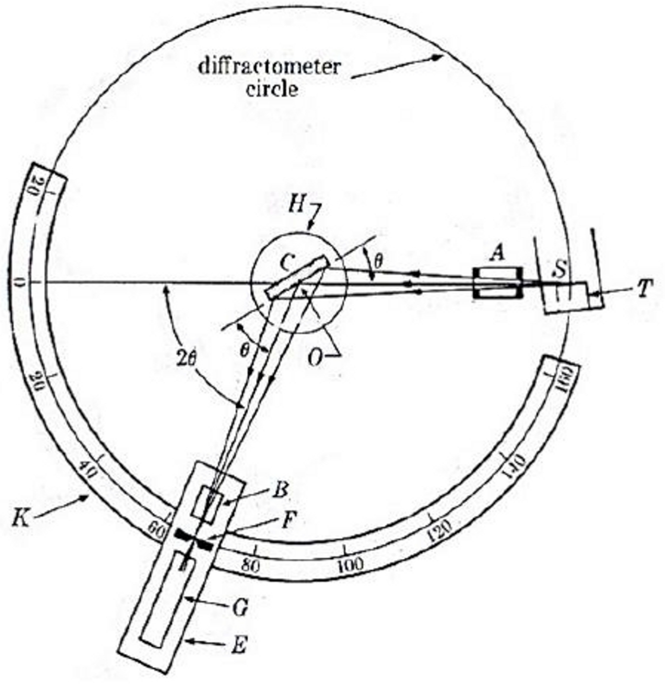

Figure 3.5: Schematic diagram of X-ray diffractometer.

will always be equal to one another and equal to half the total angle of diffraction, an arrangement is necessary to preserve focusing conditions. The counter may be power-driven at a constant angular velocity about the diffractometer axis or moved by hand to any desired angular position. The way in which a diffractometer is used to measure a diffraction pattern depends on the kind of circuit used to measure the rate of production of pulses in the counter. The pulse rate may be measured in two different ways:

1. The succession of current pulses is converted into a steady current, which is measured on a meter called a counting-rate meter, calibrated in such units as counts (pulses) per second (c/s or cps). Such a circuit gives a continuous indication of X-ray intensity.

2. The pulses of current are counted electronically in a circuit called a scaler, and the average counting rate is obtained simply by dividing the number of pulses counted by the time spent in counting. This operation is essentially discontinuous because of the time spent in counting, and a scaling circuit cannot be used to follow continuous changes in X-ray intensity.

Corresponding to these two kinds of measuring circuits, there are two ways in which the diffraction pattern of an unknown substance may be obtained with a diffractometer (3.5):

Phase identification or $2\theta - \theta$ scan

The counter is set near 2θ=0°and connected to a counting-rate meter. The counter is then driven at a constant angular velocity through increasing values of 2θ until the whole angular range is scanned. The result is a plot which gives a record of counts per second (proportional to diffracted intensity) vs. diffraction angle 2θ. The scanning speed is typically given in x°per minute and it can set according to the sample type. In the symmetric 2θ-θ scan, the angle θ of the incoming beam with respect to the sample surface is varied while simultaneously keeping the detector at an angle of 2θ, with respect to the incoming beam (3.4). The scattering vector will always be perpendicular to the sample surface and only the interplanar distances for planes that are parallel to the sample surface can be determined. For a poly-crystalline film, different lattice planes will be parallel to the sample surface and different diffraction peaks will appear. For an epitaxial film, there is only one set of planes parallel to the sample surface and only the peaks for these planes will be observed. A 2θ-θ scan allows to determine the interplanar distance d_{hkl} . This interplanar distance is characteristic for a crystal and 2θ-θ scans thus allow the identification of the crystalline phases in a thin film.

Orientation or ϕ-scan

In a 2θ-θ scan, only those planes that are parallel to the surface will be detected. The number of peaks in an experimental 2θ-θ XRD spectrum and their relative intensity give an indication of the texture of the film. However, the complete texture of a thin film is accessible only with pole figure measurements. A pole figure is measured at a fixed scattering angle (constant d spacing) and consists of a series of ϕ-scans (in-plane rotation around the center of the sample) at different tilt or azimuth angles, as described below. In this kind of measurement, a certain set of hkl-planes is selected. This fixes d_{hkl} in equation 3.4, which is achieved by fixing the detector (2θ) and incident beam (θ) angle. Hence, the scattering vector is fixed in space. Diffraction will only occur if the normal to the selected hkl-planes is parallel to the diffraction vector. Therefore, the sample has to be tilted and rotated in space. For a random orientation of the grains in the thin film, the pole figure will be featureless. No preferred orientation for the normal to the hkl-planes is observed. For epitaxial like (crystallographically oriented) nanocrystals, the pole figure is characterized by a small, discrete number of spots depending on the crystalline symmetry. Powder X-ray diffraction studies were carried out using Jeol X-ray diffractometer with the CuK$_\alpha$ radiation ($\lambda = 1.540562$ Å) in the range of 20°-80°, with a sampling rate of 1°/min.

3.3.3 Scanning Electron Microscopy

Scanning electron microscopy (SEM) is a widely used surface analytical technique. It is versatile having many other imaging modes available in it. Such as specimen current imaging using the intensity of the electrical current induced in the specimen by the illuminating electron beam to produce an image. It can often be used to show subsurface defects. High resolution images of surface topography, with excellent depth of field are produced using a highly-focused, scanning (primary) electron beam. The primary electrons enter a surface with high energy and generate many low energy secondary electrons. The intensity of these secondary electrons is largely governed by the surface topography of the sample. An image of the sample surface can thus be constructed by measuring secondary electron intensity as a function of the position of the scanning primary electron beam. High spatial resolution is possible because the primary electron beam can be focused to a very small spot (diameter $<$10 nm). High sensitivity to topographic features on the outermost surface ($<$5 nm) is achieved when using a primary electron beam with an energy of $<$1 keV. In addition to low energy secondary electrons, backscattered electrons and X-rays are also generated by primary electron bombardment. Backscatter imaging uses high energy electrons that emerge nearly 180 degrees from the illuminating beam direction. The backscatter electron yield is a function of the average atomic number of each point on the sample, and thus can give compositional information. Scanning electron microscopes are often coupled with X-ray analyzers e.g energy dispersive X-ray spectrometer (EDS or EDX). When energetic electron beam is incident on the sample, X-rays are generated that are characteristic of the elements present in the sample. The X-rays are collected by an X-ray detector. Therefore, the identification of the elements present in the specimens can be made by the qualitative and quantitative elemental analysis using Energy Dispersive X-ray analysis (EDX). The JEOL/JSM-6380LA SEM is used for most of our samples.

In a SEM (3.6), an electron gun emits a beam of electrons, which passes through a condenser lens and is refined into a thin stream (Egerton 2005). From there the objective lens focuses the electron beam onto the specimen. This objective lens contains a set of coils, which are energised with varying voltages. The coils create an electromagnetic field that exerts a force upon the electrons in the electron beam, which in turn redirects the electrons to scan the specimen in a controlled pattern called raster. The electromagnetic field of the coils also causes a spot of light on a cathode-ray tube to move along at the same rate as the scanning electron beam. When the electrons from the beam hit the specimen, a series of interactions deflect secondary particles to a de-

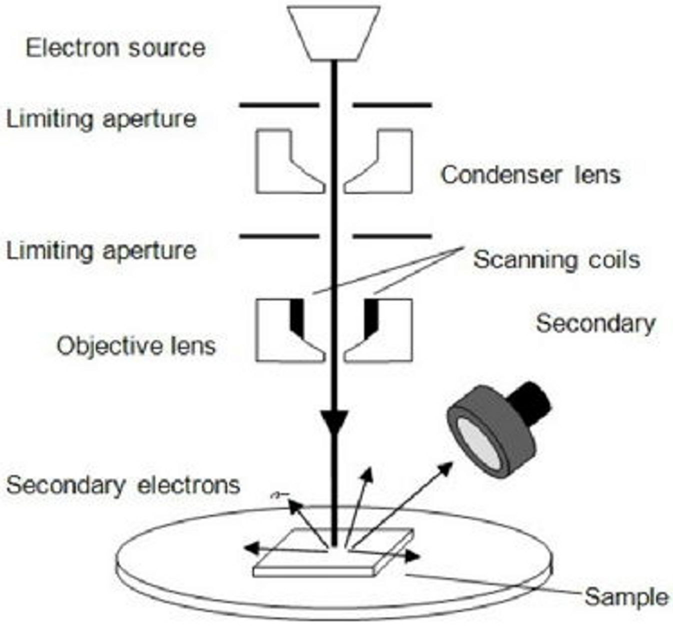

Figure 3.6: Schematic diagram of scanning electron microscope.

tector, which then converts the signal voltage and amplifies it. This voltage is then applied to a cathode-ray tube and converted to an image. The intensity of the image (brightness) is determined by the number of secondary particles that hit the detector, which is dependent upon the angle the electrons bounce off the specimen. Thus the image of the specimen depends on its topography. When an electron from the beam encounters a nucleus in the specimen, the resultant attraction produces a deflection in the electrons path, known as Rutherford elastic scattering. A few of these electrons will be completely backscattered, re-emerging from the surface of the sample. Since the scattering angle is strongly dependent on the atomic number of the nucleus involved, the primary electrons arriving at a given detector position can be used to yield images containing information on both topology and atomic composition. Some of the beam's electrons can also interact with the electrons in the sample. The amount of energy given to these secondary electrons as a result of the interactions is small, and so they have a very limited range in the sample of a few nanometers and often do not escape. The electrons at a very short distance from the surface are able to escape and are observed by the detector. The images from these secondary particles contain a lot of detailed information. This means that using secondary particles as imaging data boosts higher-resolution topographical images, making this the most widely used detection method of the SEM imaging options. SEM can produce images of greater clarity and three-dimensional quality and requires less sample preparation which include coating of a very thin layer (few Å) of non reacting conducting layer (gold) on the sample to avoid charging effect (for semiconducting and insulating samples). It has a large depth of field, that is, more of the image being magnified is in focus. In addition, SEM has an extremely wide range of magnification, producing images in the rage of 10 to 100 000 times their normal size. The SEM produces a sharp, three dimensional view of a specimen, and is very helpful in analysing its shape and structure.

3.3.4 Atomic Force Microscopy

In the atomic force microscope (AFM) a sharp tip (at the end of a cantilever) is brought sufficiently close to the surface of a specimen, so that it essentially touches it and senses an interatomic force. For many years, this principle had been applied to measure the roughness of surfaces or the height of surface steps, with a height resolution of a few nanometers. But in the 1990s, the instrument was refined to give near-atomic resolution. Initially, the z-motion of the cantilever was detected by locating an STM tip immediately above. Nowadays it is usually achieved by observing the angular deflection of a reflected laser beam while the specimen is scanned in the x- and y-directions. AFM cantilevers can be made (from silicon nitride) in large quantities, using the same kind of photolithography process that yields semiconductor integrated circuits, so they are easily replaced when damaged or contaminated. The scanning-force images must be examined critically to avoid misleading artifacts such as multiple-tip effects. The mechanical force is repulsive if the tip is in direct contact with the sample, but at a small distance above, the tip senses an attractive (van der Waals) force. Either regime may be used to provide images. Alternatively, a 4-quadrant photodetector can sense torsional motion (twisting) of the AFM cantilever, which results from a sideways frictional force, giving an image that is essentially a map of the local coefficient of friction. Also, with a modified tip, the magnetic field of a sample can be monitored, allowing

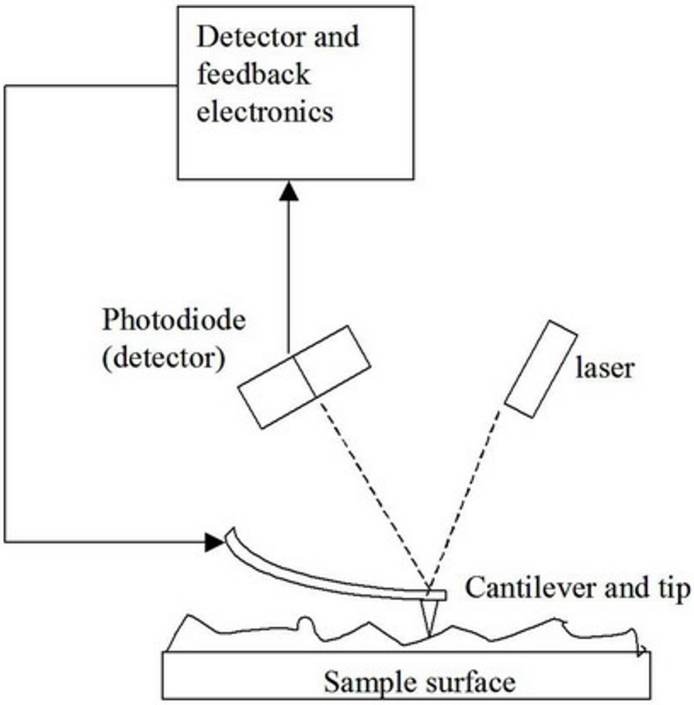

Figure 3.7: Schematic diagram of an atomic force microscope.

the direct imaging of magnetic data-storage media materials for example. Although is more difficult to obtain atomic resolution than with an STM, the AFM has the advantage that it does not require a conducting sample. In fact, the AFM can operate with its tip and specimen immersed in a liquid such as water, making the instrument valuable for imaging biological specimens. This versatility, combined with its high resolution and relatively moderate cost, has enabled the scanning probe microscope to take over some of the applications previously reserved for the SEM and TEM. However, mechanically scanning large areas of specimen is very time-consuming; it is less feasible to zoom in and out (by changing magnification) than with an electron-beam instrument. Also, there is no way of implementing elemental analysis in the AFM. An STM can be used in a spectroscopy mode but the information obtained relates to the outer-shell electron distribution and is less directly linked to chemical composition. And except in special cases, a scanning-probe image represents only the surface properties of a specimen and not the internal structure that is visible using a TEM.

An atomic force microscope (AFM) utilises a sharp probe moving over the surface of a sample in a raster scan. The probe is basically a tip at the end of a cantilever which bends in response to the force between the tip and the sample. The tip is raster-scanned across the surface of the specimen in x- and y-directions, again using piezoelectric drives. As the cantilever flexes, the light from a laser is reflected onto a split photodiode. By measuring the difference signal, changes in the bending of the cantilever can be measured. Since the cantilever obeys Hooke's law for small displacements, the interaction force between the tip and the sample can be determined. The movement of the tip or sample is performed by an extremely precise positioning device made from piezo-electric ceramics, most often in the form of a tube scanner. The scanner is capable of sub-angstrom resolution in x-, y- and z-directions. However, some limiting factors have to be taken in to account. Depending on the tip shape, the resolution will be limited as a tip is not able to profile sides of surfaces steeper than the sidewall angle of the tip. The details are available in (Egerton 2005). In this work, commercially available AFM system (Veeco, Innova) in contact mode was used. Nanoscope software was used to examine the three dimensional features on AFM image.

3.3.5 Transmission spectroscopy

The absorption/ transmission measurements are done on a material to determine the different electronic and optical transitions in the material and the band gap of the material. When an incident light falls on a material a part of it is reflected, a part transmitted and the rest absorbed. The absorption occurs when the energy of the incident photon is absorbed by the electron that is then promoted to a higher energy level. The absorption coefficient α of any material can be defined in terms of change in intensity of a monochromatic beam as a function of the distance traversed in the medium:

$$I(\lambda) = I_0(\lambda)e^{\alpha(\lambda)t} \tag{3.5}$$

The absorption coefficient is dependent on the wavelength of the incident light. All the light is transmitted when the energy of the incident beam is less than the energy of available transitions (e.g. transitions associated the band gap E$_g$ or a mid-gap states). As soon as the energy of the incident photon is equal to that of a transition, the beam is absorbed by the material. When reflection is negligible, the most common method to determine the absorption coefficient as a function of the wavelength is to measure the transmittance of the film as a function of the wavelength of the incident beam in the optical range of interest. The transmittance, T(λ), of the film is defined as the ratio of intensity of the transmitted beam to that of the incident beam:

$$T(\lambda) = \frac{I(\lambda)}{I_0(\lambda)} \tag{3.6}$$

Using equations 3.5 and 3.6 we get

$$T(\lambda) = e^{\alpha(\lambda)t} \tag{3.7}$$

Thus, if the thickness of the film, t, is known, then the absorption coefficient can be determined. In this work, the transmission measurements of the films were done in the range 200-900 nm using a Ocean Optics UV 2000 UV-Vis spectrophotometer. Figure 3.8 shows the schematic layout of the single beam spectrophotometer. The spectrophotometer has two continuous light sources:1) W lamp for the visible range (320-900 nm) and a deuterium lamp for the UV range (200-320 nm). A bare substrate is used as a reference to obtain the transmittance spectra of the film relative to the substrate.

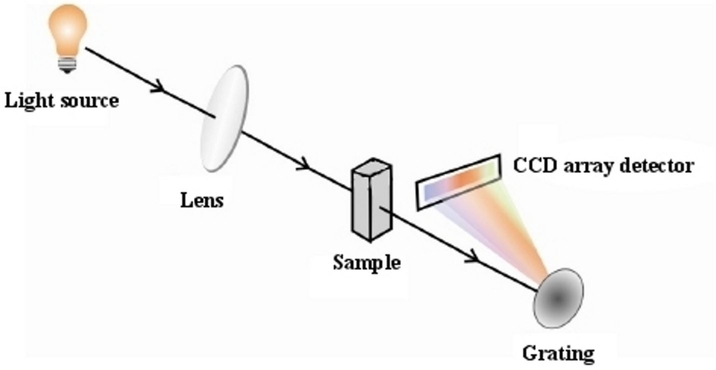

Figure 3.8: Schematic diagram of single beam UV-Visible spectrometer.

3.3.6 Nonlinear Optics and Optical Limiting

The invention of the laser gave rise to the study of optics at high intensities, leading to new phenomena not seen with ordinary light. The high degree of coherence of laser radiation can change the optical properties of a medium. i.e., a laser with wavelength 1 μm when focused on an area A~λ^2, gives electric field E~10^{10}V/m, which is within the range of atomic fields. At such high fields, the relationship between the electric polarization P and the field strength E ceases to be linear and some interesting nonlinear effects come in to act (Laud 1991). Inherent charges in the material interact with the electromagnetic field of the incident laser causing its phase, frequency, amplitude or polarization to be altered. The study of these interactions is known as nonlinear optics. Thus nonlinear optics is the study of phenomena in which modifications of the optical properties of a material system takes place due to intense light (Boyd 2008). Nonlinear properties was been strikingly demonstrated by the harmonic generation of light observed by Franken & co workers in 1961 (Franken et al. 1961). They observed ultraviolet light at twice the frequency of a ruby laser light, when the light was made to traverse a quartz crystal. This experiment attracted widespread attention and marked the beginning of the experimental and theoretical investigation on nonlinear optical properties (Laud 1991). When the monochromatic radiation of frequency ω and electric field E(t), propagate in a material, the atoms and molecules oscillate at the frequency of the electric field applied. Dipoles are created because of the displacement of charges, and the dipole moment per unit volume describes the induced or linear polarization P(t) of the medium. The linear polarization is given by,

$$P = \varepsilon_0 \cdot \chi^{(1)} \cdot E \tag{3.8}$$

With sufficiently intense electric fields, such as lasers, as the applied field strength increases, the polarization has a nonlinear dependence and can be expressed as a power series:

$$P(t) = \varepsilon_0[\chi^{(1)} \cdot E(t) + \chi^{(2)} \cdot E^2(t) + \chi^{(3)} \cdot E^3(t) + ...] \tag{3.9}$$

$$P = P^{(1)(t)} + P^{(2)(t)} + P^{(3)(t)} + ... \tag{3.10}$$

where, $\chi^{(1)}$ is the linear susceptibility, $\chi^{(2)}$ is the second-order nonlinear susceptibility, and $\chi^{(3)}$ is the third-order nonlinear susceptibility. $\chi^{(2)}$, $\chi^{(3)}$,..... define the degree of nonlinearity and are known as nonlinear susceptibilities. They are not significant in the linear regime because of their relative strengths (Laud 1991; Boyd 2008; Sutherland

2003). Nonlinear optical materials have been evoking worldwide interest in researchers owing to their vast potential for applications in opto-electronic devices, high speed optical communication networks, display technologies, optical information storage, photonics, optical limiting devices, etc. (Frobel et al. 2011).

Third-order Nonlinear Optical Processes

Consider the third-order contribution to the nonlinear polarization

$$P^{(3)}(t) = \varepsilon_0 \chi^{(3)} E^3(t) \tag{3.11}$$

For the general case in which the field E(t) is made up of several different frequency components, the expression for $P^{(3)}(t)$ is very complicated. For this reason, first consider the simple case in which the applied field is monochromatic and is given by

$$E(t) = \boldsymbol{\varepsilon} cos\omega t \tag{3.12}$$

Then we can express the nonlinear polarization as

$$P^{(3)}(t) = \frac{1}{4}\varepsilon_0 \chi^{(3)} \boldsymbol{\varepsilon}^3 cos\omega t + \frac{3}{4}\varepsilon_0 \chi^{(3)} \boldsymbol{\varepsilon}^3 cos\omega t \tag{3.13}$$

The first term in equation 3.13 describes a response at frequency 3ω that is created by an applied field at frequency ω. This term leads to the process of third harmonic generation, which is illustrated in Figure 3.9 . According to the photon description of this process, shown in part (b) of the Figure 3.9, three photons of frequency ω are destroyed and one photon of frequency 3ω is created in the microscopic description of this process. The second term in equation 3.13 describes a nonlinear contribution to the polarization at the frequency of the incident field; this term hence leads to a nonlinear contribution to the refractive index experienced by a wave at frequency ω. The refractive index in the presence of this type of nonlinearity can be represented as

$$n = n_0 + n_2 I \tag{3.14}$$

where n_0 is the linear refractive index, and

$$n_2 = \frac{3}{2n_0^2 \omega_0 c}\chi^{(3)} \tag{3.15}$$

is an optical constant that characterizes the strength of the optical nonlinearity, and where I = $\frac{1}{2} n_0 \omega_0 c \boldsymbol{\varepsilon}^2$ is the intensity of the incident wave.

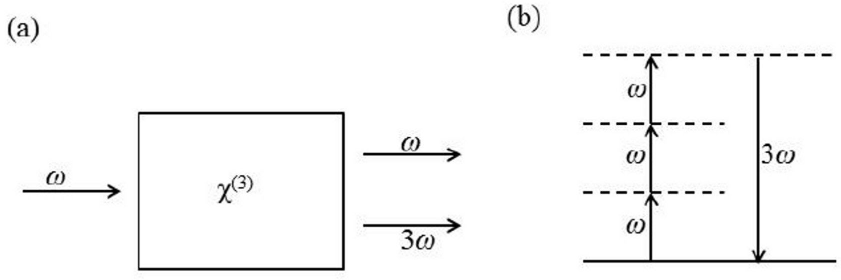

Figure 3.9: Third-harmonic generation (a) geometry of the interaction (b) energy- level description.

Two-photon Absorption (TPA)

The two-photon absorption is a nonparametric process described by a complex susceptibility. In this process, which is illustrated in Figure 3.10 , an atom makes a transition from its ground state to an excited state by the simultaneous absorption of two laser photons. The absorption cross section σ describing this process increases linearly with laser intensity according to the relation

$$\sigma_2 = \beta I \tag{3.16}$$

where β is a coefficient that describes strength of the two-photon absorption process (In conventional linear optics the absorption cross section σ is a constant). Consequently,

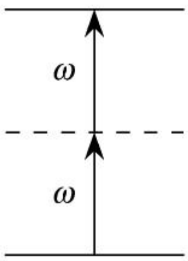

Figure 3.10: Two-photon absorption.

the atomic transition rate R due to two-photon absorption scales as the square of the laser intensity. To justify this conclusion, we note that $R = \frac{\sigma I^2 2\pi}{h\omega}$, and consequently that

$$R = \frac{\beta I^2 2\pi}{h\omega} \tag{3.17}$$

Two-photon absorption is a useful spectroscopic tool for determining the positions of energy levels that are not connected to the atomic ground state by a one-photon transition. Two-photon absorption was first observed experimentally by Kaiser and Garrett (1961).

3.3.6.1 Z-Scan Technique

There are numerous techniques for measuring the nonlinear refraction in materials. Among them the z-scan technique developed by Mansoor Sheik-Bahae et al. (1989; 1990) is the most simplest and sensitive technique for measuring the sign and magnitude of refractive nonlinearities. Z-scan works on the principle of moving the sample under investigation through the focus of a tightly focused Gaussian laser beam. The interaction of the sample with the laser light changes as the sample is moved. This is because the sample experiences different intensities, dependent on the sample position relative to focus (z=0). The power transmitted through the sample is measured by translating the sample along the z-direction through the beam waist of a focused beam and hence the name z-scan. The two measurable quantities connected with z-scan are, Nonlinear Absorption (NLA) and Nonlinear Refraction (NLR) from which one can determine the nonlinear absorption coefficient β and nonlinear index of refraction n_2 of the sample (Sheik-Bahae et al. 1990). Figure 3.11 shows the z-scan experimental set up. The transmittance of a nonlinear sample using a single Gaussian laser beam is explained by an example: consider a material with a negative nonlinear index of refraction and thickness less than the Rayleigh length Z_R, of the focused laser beam. The sample

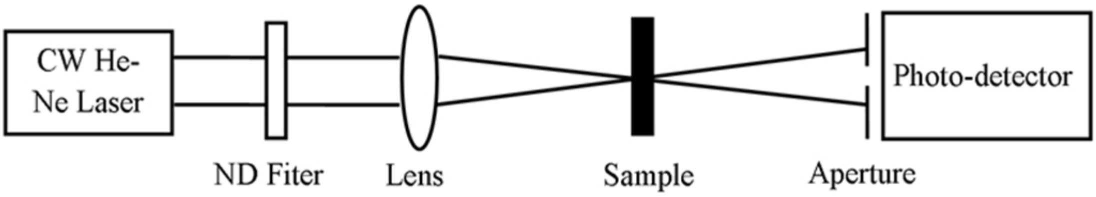

Figure 3.11: Schematic diagram of z-scan experimental set up.

exhibits negligible nonlinear refraction when it is far from the focus [negative z], because of the low intensity of the laser beam at this position. As the sample is moved towards the focus it starts acting as a negative lens (diverges the incident beam), collimating the beam and shifting the waist of laser beam. The result is a smaller spot size at the aperture placed in front of the detector D_2 and thus a higher transmittance through the aperture. This effect increases as the sample is moved towards the focus due to the increase in intensity. The maximum transmittance through the aperture will occur when the sample is just in front of the focus. The maximum in transmittance [peak] will drop to minimum [valley] as the sample is moved to the right [+ve z], self defocusing increases the beam divergence, leading to beam broadening at the aperture and thus decrease in transmittance. The transmittance through the aperture will again return to the linear value as the sample is further moved from the focus. This is analogous to placing a thin lens at or near the focus, resulting in a minimal change of the far field pattern of the beam. This can be regarded as a thin lens of variable focal length. The result of a scan is a prefocal transmittance maximum (peak) followed by post focal transmittance (Sheik-Bahae et al. 1989) minimum (valley), is the signature of -ve refractive nonlinearity. Similarly, for the sample having +ve nonlinear index of refraction, the graph is

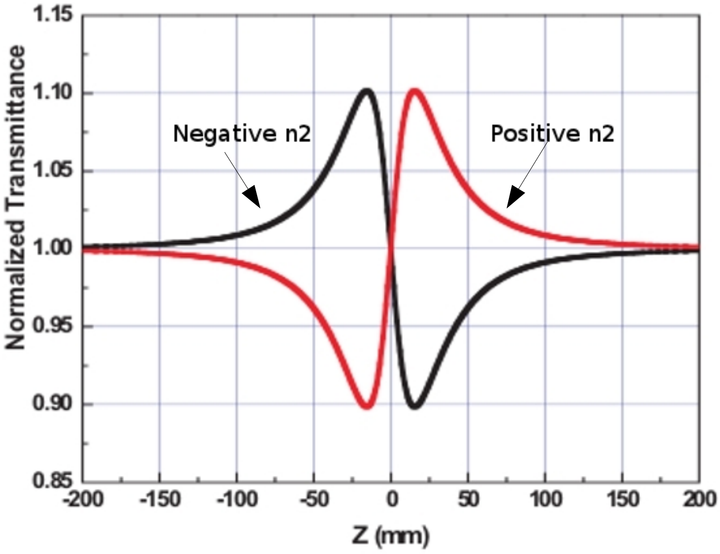

Figure 3.12: A schematic diagram showing closed aperture z-scan traces for samples with a positive and a negative nonlinear index of refraction n_2.

inverted as shown in Figure 3.12. The sign of the nonlinear index of refraction n_2 of a sample is thus immediately clear from the shape of graph. The sensitivity to nonlinear refraction is entirely due to aperture, and removal of aperture completely eliminates the effect. It is important to note that in most of the cases nonlinear refraction does not occur on its own, but usually in conjunction with nonlinear absorption. This implies that the data from a z-scan will contain both nonlinear refraction and nonlinear absorption. To extract the nonlinear index of refraction, it is necessary to perform a z-scan without the aperture in order to measure the total transmittance of the sample [open aperture]. The measured transmittance of an open aperture trace is then independent of nonlinear refraction and only dependent on nonlinear absorption. Figure 3.13 shows the open aperture data curve. Once the open aperture z-scan is performed, the nonlinear absorption coefficient β can be determined. Since the closed aperture z-scan contains both nonlinear refraction and nonlinear absorption, one can extract pure nonlinear refraction by dividing the closed aperture z-scan trace by the open aperture z-scan trace, using the closed aperture z-scan traces, one can determine the nonlinear index of refraction n_2. Thus by using the z-scan technique we can determine the sign and magnitude of nonlinear index of refraction n_2 and nonlinear absorption coefficient β of materials. By

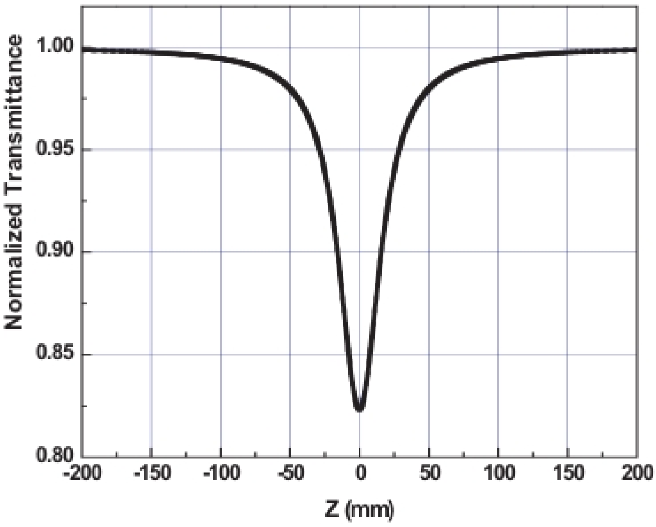

Figure 3.13: A schematic diagram showing an open aperture z-scan trace.

using the values of the nonlinear index of refraction n$_2$ and the nonlinear absorption coefficient β, the third-order nonlinear susceptibility is determined. The third-order nonlinear susceptibility is given by,

$$\chi^{(3)} = \chi_R^{(3)} + i\chi_I^{(3)} \tag{3.18}$$

where, the real part is related to n$_2$ or γ (in esu) through the relation,

$$\chi_R^{(3)} = 2n_0^2\varepsilon_0 c\gamma \tag{3.19}$$

and the imaginary part is related to β (in esu) through the relation,

$$\chi_I^{(3)} = \frac{n_0^2\varepsilon_0 c^2}{\omega}\beta \tag{3.20}$$

3.3.6.2 Optical Power Limiting

With the extensive use of continuous wave lasers at power levels ranging from µW to kW in various applications, the need for protecting the human eye and the sensors like range finders, night vision equipment, etc., has become increasingly important. All optical sensors have a threshold intensity above which they can be damaged. This necessitates the protection of these sensors from the high intensity laser light. Optical limiter transmits light of low intensities (ambient light) but absorbs high intensity light (laser). By using the appropriate materials as optical limiters, one can extend the dynamical range of the sensors, allowing them to function at higher input intensities. Optical limiters are gaining importance as the intense lasers are used commonly, in both commercial and domestic applications. The minimum criteria identified for a material to act as an effective optical limiter are,

- low limiting threshold & large dynamic range,
- high optical damage & stability,
- sensitive broadband response to long & short pulses,
- fast response time,
- high linear transmittance throughout the sensor bandwidth,

- optical clarity and
- robustness (good mechanical, temperature, humidity stability).

Although there is not yet any material that can provide all these requirements alone, devices can be assembled from combinations of various optical limiters (Neethling 2005). Optical limiting can be achieved by means of various nonlinear optical mechanisms including self-focusing, self-defocusing, excited state absorption, two photon absorption, free- carrier absorption, photo refraction, induced scattering, induced-refraction and induced aberration, in nonlinear optical media (Neethling 2005). The optical power limiting experimental set up is similar to standard z-scan geometry. The optical power limiting measurements will be carried out by placing the sample at or near the focus of the laser beam and by varying the input laser intensity using neutral density filter and the change in the output intensity is measured using a photo detector. The response of an ideal optical power limiter is shown in Figure 3.14. As the incident power/intensity of light increases, the transmitted power/intensity of light reaches a threshold value (limiting threshold value) at which point it is clamped. The limiting threshold is defined as the incident power at which the sample transmittance falls to 50% of the linear transmittance. The optical limiting results from irradiance dependent nonlinear optical properties of materials. When considering a material as an optical power limiter, two

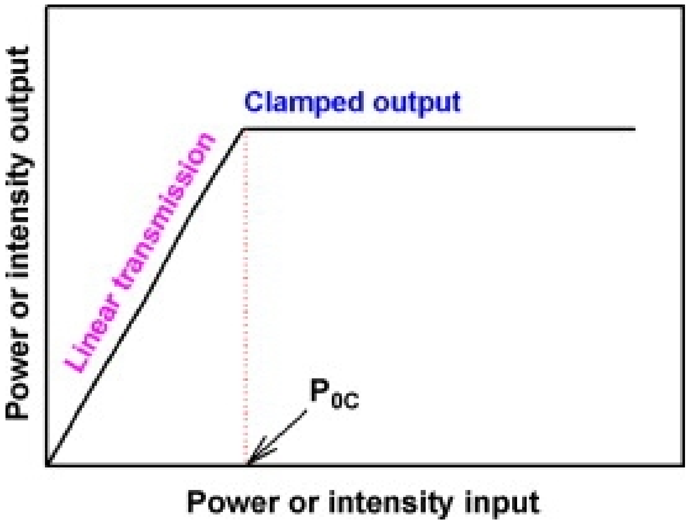

Figure 3.14: Response of an ideal optical limiter.

of the properties that are of particular interest are the materials nonlinear absorption coefficient β and its nonlinear index of refraction n_2. Both change the intensity of light in a nonlinear way as it passes through the medium. By measuring these nonlinear properties of materials, the materials can be identified as possible optical power limiter (Neethling 2005).

Chapter 4

Growth, characterization and properties of ZnO thin films

In this Chapter, growth of undoped ZnO thin films by direct current (DC) reactive magnetron sputtering and radio (RF) frequency magnetron sputtering has been discussed. It also presents the results and discussions on structural, linear and nonlinear optical properties of deposited films.

4.1 Inroduction

Extensive research has been focussed on the various properties of ZnO by many researchers since many decades (Pearton et al. 2004). Still it is gaining the researchers attention due to its potential properties. ZnO can be considered as an 'old' semiconductor which has been compelling research attention for a long time because of its applications in many scientific and industrial areas such as piezoelectric transducers, optical waveguides, acousto-optic media, conductive gas sensors, transparent conductive electrodes, light emmitters, varistors etc., (Pearton et al. 2008, 2004; Look et al. 2004). These potential applications have boosted research related to the growth of high quality ZnO thin films by a lot of different techniques. Many methods were employed to deposit good quality ZnO films such as spin coating, spray pyrolysis, pulsed laser deposition, molecular beam epitaxy, chemical bath deposition, dip coating, sputtering etc. Among all, sputtering has several advantages a) low substrate temperature (down to room temperature); b) good adhesion of films on substrates; c) very good thickness uniformity; d) directive deposition from elemental targets by reactive sputtering in rare/reactive gas mixtures (Hong et al. 2005; Ayadi et al. 2007).

Non-toxicity and better radiation resistance of ZnO are added advantages in many applications leading to devices. Considering the nonlinear optical properties of ZnO, it is reported that ZnO exhibits second and third order nonlinear optical behavior, both in crystals and thin films (Mitra and Thareja 2001; Wang et al. 2002; Neumann et al. 2004; Bolger et al. 1993; Cao et al. 1998). The third order susceptibility $\chi^{(3)}$ is of particular interest because of its importance in applications such as nonlinear propagation in fibers, fast optical switching and optical limiting. The study of photo physical and optical characteristics such as nonlinearity, magnitude, response time, etc., must be carried out to spot the material suitability for nonlinear applications. Inorganic nanomaterials such as, carbon nanotubes (CNTs), nanoparticles and metal complexes and clusters have been playing increasingly important roles in the laser protection field (Wang and Blau 2009). Also, the properties of thin films are strongly dependent on the post deposition processes, in particularly annealing. Hence, this requisites the knowledge and study of optical nonlinearity of ZnO thin films working under cw laser regime also as power limiter in the visible range. In this chapter, the growth of ZnO thin films with different sputtering techiniques has been discussed. The effect of post deposition annealing on nonlinear optical properties of ZnO thin films prepared by RF magnetron sputtering on quartz substrates has also been discussed. To the best of our knowledge, the study of nonlinear optical properties of ZnO thin films under continuous wave laser regime has not been investigated.

Table 4.1: Parameters used for the deposition of undoped ZnO thin films on glass substrates using RF sputtering

Sputter power	100-300 W
Working pressure	$1X10^{-2}mbar$
Duration	60 $minutes$
Substrate to target distance	50 mm
Substrates	cleaned glass slides

4.2 Experimental

4.2.1 Growth of ZnO thin films using DC reactive sputtering of Zn target

Thin films of ZnO were grown by reactive DC sputtering using a 2 inch diameter Zn disc (99.999, Alfa Aesar) on cleaned glass substrates at room temperature. The glass plates were cleaned using a procedure described in chapter 3. Argon and oxygen were used as sputtering and reactive gases respectively. The target to substrate distance was adjusted to 50 mm. The cathode was mounted on a water cooled copper plate. In all the experiment the base pressure was less than 10^{-6} mbar. The deposition is done under different working pressures and different sputtering pressures keeping one of them as constant. Before each run, target was pre-sputtered in pure argon for 15 minutes to remove contaminations on the target surface if any.

4.2.2 Preparation of compound sputtering target

In a typical experiment, high purity ZnO powder was taken in the required weight (approx. 30 gms) and ground thoroughly using agate mortar and pestle. The powder was calcinated to remove moisture and other contaminations. After calcination the resulting powder was mixed with few drops 10% polyvinyl alcohol solution and mixed till homogenous mixture was obtained. This mixture was pressed using a hydrolic press at a pressure around 25 MPa to form a compacted disc. Sintering of these discs will

Table 4.2: Parameters used for the deposition of undoped ZnO thin films on quartz substrates using RF sputtering

Sputter power	200 W
Total working pressure (Ar+O_2)	$6X10^{-3}mbar$
Ar to O_2 ratio	5
Duration	100 $minutes$
Substrate to target distance	50 mm
Substrates	cleaned quartz

give rise to dense pellets and used as targets. The parameters for the preparation of targets include calicination temperature, pressure and sintering temperature.

4.2.3 Growth of ZnO thin films using RF sputtering of ZnO compound target

ZnO thin films were deposited by employing a sintered ZnO pellet as target. The substrates were cleaned glass slides and quart substrates with a thickness around 1 mm. Glass and quartz substrates are cost effective and available easily. To study the effect of high temperature annealing the films are deposited on quartz as it is stable at high temperatures. Radio frequency power supply of frequency 13.56 MHz was used to ionise the sputter gas. The deposition parameters used for the films deposited on glass substrates are tabulated in Table 4.1. Table 4.2 gives the deposition parameters for the films deposited on quartz substrates.

4.2.4 Characterizations

The X-ray diffraction studies of the prepared films and the compound targets were carried out using JOEL, DX-GE-2P and Rigaku miniflex X-ray diffractometer using a Cu-K_α radiation. Optical microscope images were taken using LABEN optical microscope. The SEM and EDX studies were carried out using a JOEL/JSM-6380LA analytical scanning electron microscope. Optical absorption spectra were recorded using

Ocean Optics USB-2000 and USB-4000 fiber optics spectrometer. Electrical resistance measurements were done using a Keithley-2400 sourcemeter.

4.2.5 Z-scan and Optical limiting

Z-scan technique developed by Sheik Bahae et al. (1989) has been employed for evaluating the nonlinear refractive index n_2, the nonlinear absorption coefficient β_{eff}, the magnitude and sign of the real and imaginary parts of third-order nonlinear optical susceptibility $\chi^{(3)}$ of as deposited and annealed ZnO thin films. Z-scan technique is known for its simplicity and sensitivity, relies on the distortions induced in spatial and temporal profile of the input beam on passing through the sample. In the present experiment, a polarized Gaussian laser beam is focused to a narrow waist and the sample is mounted on the micro meter translation stage. The sample is translated between +z and -z positions along the z-direction, the transmitted intensity through the sample is measured, without and with the presence of aperture at far field in front of the photo detector. As the sample moves through the beam focus (z=0), self- focusing or self-defocusing modifies the wave front phase, there by modifying the detected beam intensity. Z-scan experiments for as-deposited and annealed (in the range 400-1000 °C) films were performed separately using Thor labs He-Ne (Model: HRP350-EC-1) continuous wave (CW) laser at 633 nm wavelength as an excitation source. The laser beam was focused to a spot size of 36.78 μm and the Rayleigh length Z_R of 6.71 mm using a 5 cm focal length lens with input power 18.9 mW.

Optical power limiting measurements were performed for all the film samples. The samples were placed at the focal plane of the lens. The input power of the laser beam was varied using neutral density filter and the resultant output power through the samples was recorded using a photo-detector which is fed to Thor labs dual channel optical power and energy meter (Model: PM320E).

4.3 Properties of reactively sputtered ZnO thin films

4.3.1 Structure and morphology

X-ray diffraction studies have been performed in order to determine the crystal structure of the thin films. The powder diffraction patterns for as-deposited ZnO thin films under different growth conditions are shown in Figure 4.1 and 4.2. Using ICDD database, the observed characteristic peaks of ZnO were identified (JCPDS card 00-001-1136). The X-ray spectrogram shows a single peak ($2\ \theta = 34^o$) corresponding to the (0 0 2) planes of Wurtzite ZnO. This shows a preferred orientation of the films along c-axis. All the films grown by reactive sputtering showed preferred orientation along c-axis. This is because the surface energy density of the (0 0 2) orientation in ZnO crystal is lowest (Major et al. 1983). Grains with lower surface will become larger as the film grows. Then the growth orientation develops into one crystallographic direction of the lowest surface energy. Figure 4.1 shows X-ray diffraction spectra of the films deposited with different sputter powers and constant working pressure (9×10^{-3} mbar). Table 4.3 shows summary of the parameters obtained for the thin films grown using reactive DC sputtering under different growth conditions.

The intensity of (0 0 2) peak is increasing with the increase of sputter power indicating good crystallinity of the films. The full width at half maxima (FWHM) of the films decrease with the increase of sputter power. It is associated with the grain size of the thin films. The film deposited with lower power has high FWHM indicating a smaller grain size. As the sputter power increased the grains become larger. The grain size of the films can be estimated by Scherrer formula (Cullity 1978).

$$t = \frac{0.9\lambda}{B\ cos\theta} \tag{4.1}$$

where, λ is the wavelength of the X-ray 0.1540 nm, B is FWHM in radians and θ is Bragg diffraction angle. The calculated values of t were tabulated in the Table 4.3. As the sputter power increases grain size also increase. The films deposited with the constant sputter power (50 W) did not show any particular trend with the increase in

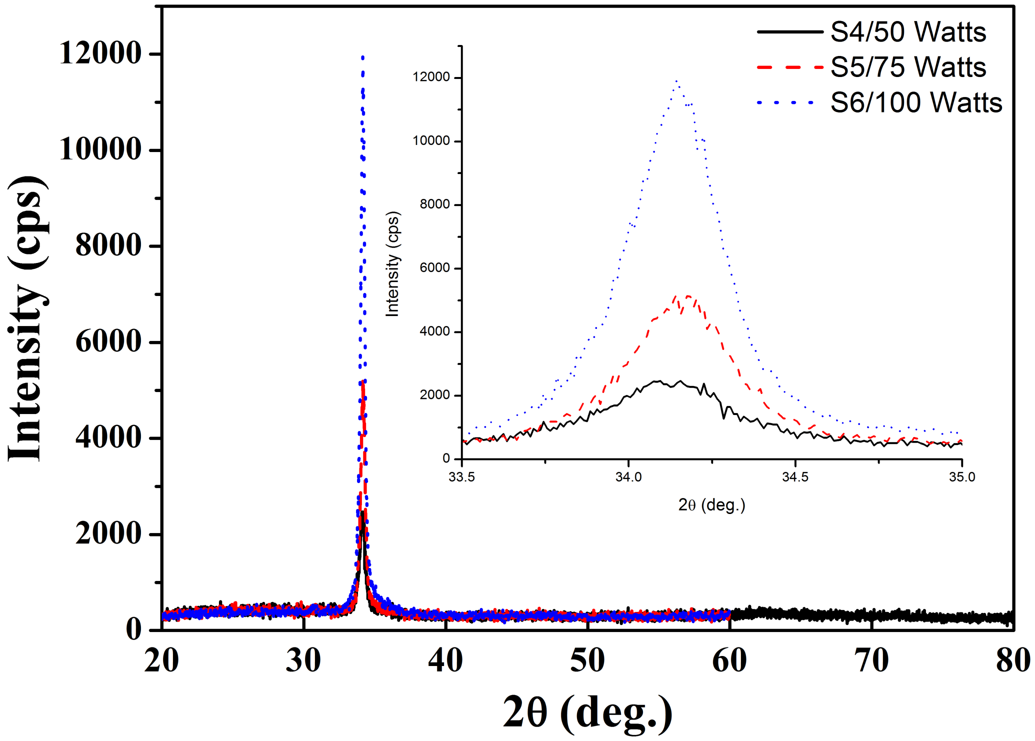

Figure 4.1: X-ray diffraction spectra for the DC reactively sputtered thin films deposited with different sputtering powers and constant working pressure (9×10^{-3} mbar).

working pressure. But, the grain size was found as largest for the films deposited at higher working pressures.

The mean free path of the sputtering gas molecules is given by

$$\lambda = \frac{2.303 \times 10^{-20} T}{P {\delta_m}^2} \tag{4.2}$$

where T is the temperature, P is the pressure and ${\delta_m}^2$ is the molecule diameter. Thus increase in the working pressure will lead to decrease in the mean free path in turn there will be a large number of collisions. Due to this, the sputtered atoms have a high probability to agglomerate before arriving at the substrate surface. So the particle size will increase with the increase in working pressure (Singh et al. 2007). The particle size is also found to increase with the increase in the sputter power. As the sputter power increases the number of ions will also increase which in turn increase the probability to

Table 4.3: Summary of the deposition parameters and structural properties for the films grown using reactive DC sputtering

Sample No.	**Sputter power** (W)	**Working pressure** $(mbar)$	**Peak position** $(deg.)$	**d** $(\AA)$	**Film stress** (MPa)	**FWHM** $(deg.)$	**Grain size** (nm)	**Thickness** (nm)
$S1$		$8X10^{-3}$	34.160	2.621	-1935	0.365	23	410
$S2$	50	$9X10^{-3}$	34.120	2.624	-2204	0.400	21	600
$S3$		$1X10^{-2}$	34.185	2.619	-1765	0.228	36	1293
$S4$	50		34.120	2.624	-2204	0.400	21	600
$S5$	75	$9X10^{-3}$	34.140	2.623	-2069	0.341	24	776
$S6$	100		34.160	2.621	-1935	0.306	27	1230

agglomerate leading to grain growth.

In all the thin films deposited films the 2θ positions were less than that of bulk ZnO powder which is 34.45°. There is a discrepancy in d-value, which is due to the crystal lattice distortion by residual stresses developed in thin films. The calculation of the film stress is based on the biaxial strain model. The strain in the films along the c-axis can be expressed by the formula (Zhang et al. 2009)

$$\epsilon = \frac{(d - d_o)}{d_o} \tag{4.3}$$

where d and d_o are strained and unstrained lattice coefficient, respectively. The lattice coefficient of the deposited films can be calculated according the Bragg formula and the peak positions in the XRD pattern. The residual stress in the films which is valid for hexagonal lattice is given by

$$\sigma_{film} = \frac{2{c_{13}}^2 - c_{33}(c_{11} + c_{12})}{2c_{13}}.\epsilon \tag{4.4}$$

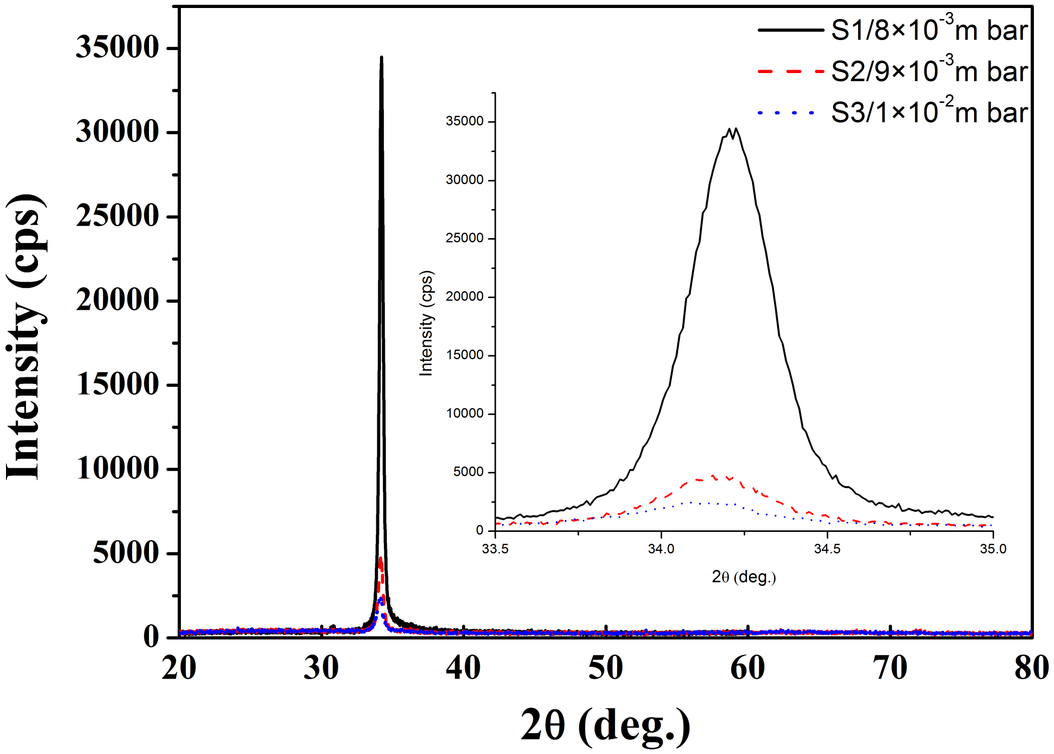

Figure 4.2: X-ray diffraction spectra for the DC reactively sputtered films deposited at different working pressures and with a constant power (50 W).

For the elastic constants c_{ij}, the following values corresponding to the stress free ZnO were used: c_{11}= 208, c_{33} =213.8, c_{12}=119.7 and c_{13}=104.2 GPa (Cebulla et al. 1998). The residual stress found to have a negative value which indicates a compressive stresses developed in the films.

Table 4.3 gives stress values calculated for films deposited at constant pressure (9×10^{-3} mbar) and different sputter power. The compressive stress was highest for the films deposited at 50 W and it drops significantly with increasing power. Stresses found in the films deposited with different working pressure and constant sputter power (50 W) was tabulated in Table 4.3. The stress was compressive in nature and found to increase as the working pressure increased. But for the higher working pressure it is found to decrease from 2204 MPa to 1935 MPa.

Figure 4.18 shows electron microscope images taken for the as deposited films.

Low magnification images show the films are uniform and pin hole free. High magnification image of the same film is shown in Figure 3.8 (b), and it shows nano grains.

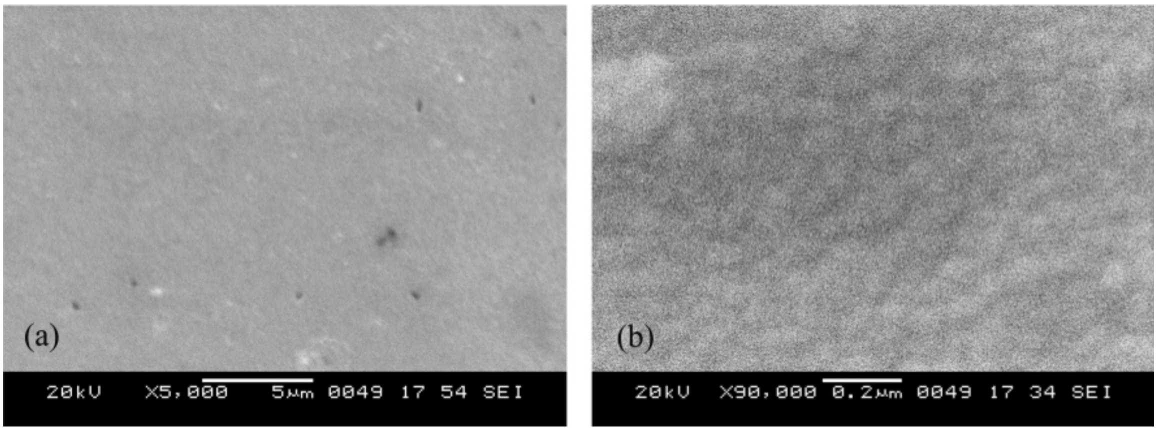

Figure 4.3: SEM images of the deposited ZnO thin films

4.3.2 Thickness measurement of ZnO thin films

If the thickness of the film is uniform, interference effects give rise to a fringes shown in the Figure 4.4. These fringes can be used to calculate the optical constants of the film. By using these optical constants we can also calculate the thickness of the film. We adopted the method proposed by Swanepoel which is known as Swanepoel's envelop method (Swanepoel 1983). The envelop curves were formed by fitting curves obtained for T$_{max}$ and T$_{min}$ of the interference pattern in the weak absorption and transparent region of the transmission spectra (Figure 4.4). The Matlab program was used to get the fitting curves for T$_{max}$ and T$_{min}$. The thickness of the films was calculated from the equation (Swanepoel 1983),

$$d = \frac{M\lambda_1\lambda_2}{2[n(\lambda_1)\lambda_2 - n(\lambda_2\lambda_1)]} \tag{4.5}$$

where, M is the number of oscillations between the two maxima or minima λ_1, λ_2 and $n(\lambda_1)$, $n(\lambda_2)$ are the corresponding indices of refraction. Refractive index n is calculated by equations

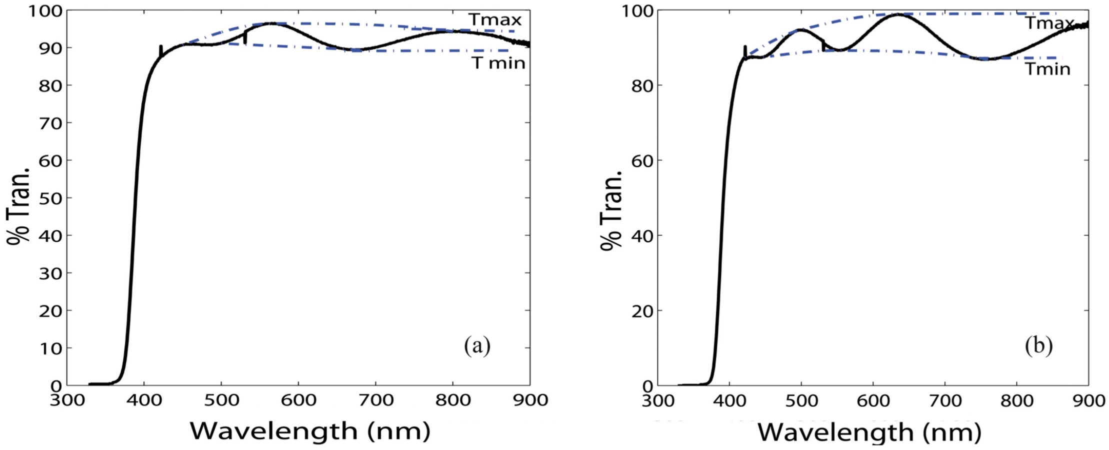

Figure 4.4: Fitted envelop curves for the samples (a) S3 and (b) S5.

$$n = [N + (N^2 - {n_s}^2)^{\frac{1}{2}}]^{\frac{1}{2}} \tag{4.6}$$

and

$$N = \frac{(n_s + 1)}{2} + 2n_s \frac{(T_{max} - T_{min})}{(T_{max} T_{min})} \tag{4.7}$$

where, n_s is the refractive index of the substrate and T_{max} and T_{min} are the maximum and the minimum transmittances at a same wavelength in the fitted envelop curves on the transmittance spectrum which is shown in Figure 4.4. The thicknesses of the deposited films are tabulated in Table 4.4. The thickness of the films found to increase with the sputter power. The thickness found by gravimetric method is in good agreement with one found by Swanpoel's method. Therefore, it can be used for finding out the thickness of the films as it is reproducible and accurate.

4.3.3 Optical studies

Figure 4.5 shows the optical transmittance spectra of the ZnO thin films deposited with the different sputter powers and different working pressure by keeping one of them fixed. The spectra were recorded in the wavelength range 300-900 nm. All the films show an average transmittance above 85% in the wavelength region from 380 to 900 nm. The absorption edge was found to shift towards the higher wavelength side with

Table 4.4: Calculated film thickness and optical bandgap for the ZnO thin films

Sample No.	**Sputter power** (W)	**Working pressure** $(mbar)$	**Grain size** (nm)	**Thickness** (nm)	**Energy bandgap** (eV)
$S1$	50	$8X10^{-3}$	23	410	3.33
$S2$		$9X10^{-3}$	21	600	3.36
$S3$		$1X10^{-2}$	36	1293	3.28
$S4$	50	$9X10^{-3}$	21	600	3.36
$S5$	75		24	776	3.32
$S6$	100		27	1230	3.26

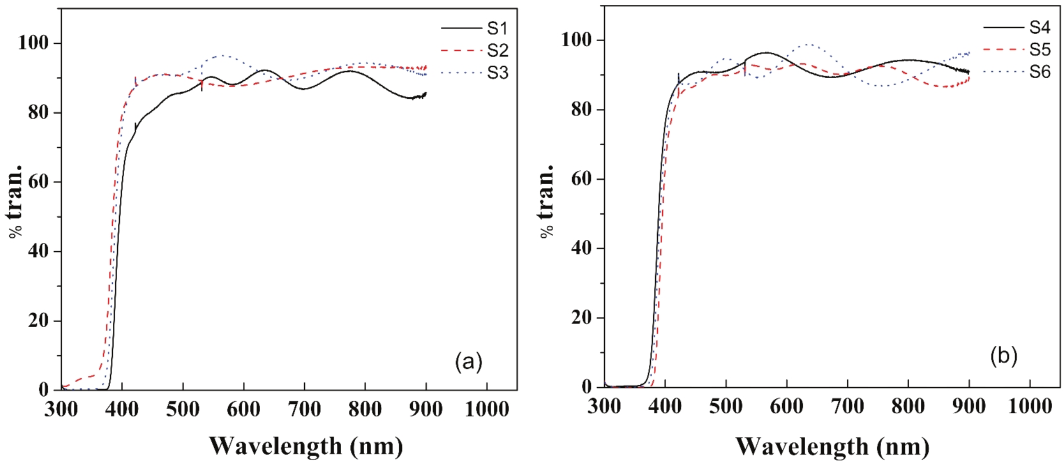

Figure 4.5: Optical transmission spectra for the thin films grown at (a) constant sputter power of 50 W and different working pressures (b) different sputtering powers and constant working pressure of 9x10^{-3} mbar.

the sputter power. But the films deposited at constant sputter power and different working pressure show no particular trend. The interference patterns were observed in the weak absorption and transmittance region of the transmission spectrum (Figure 4.5) indicating the good thickness uniformity of the deposited films.

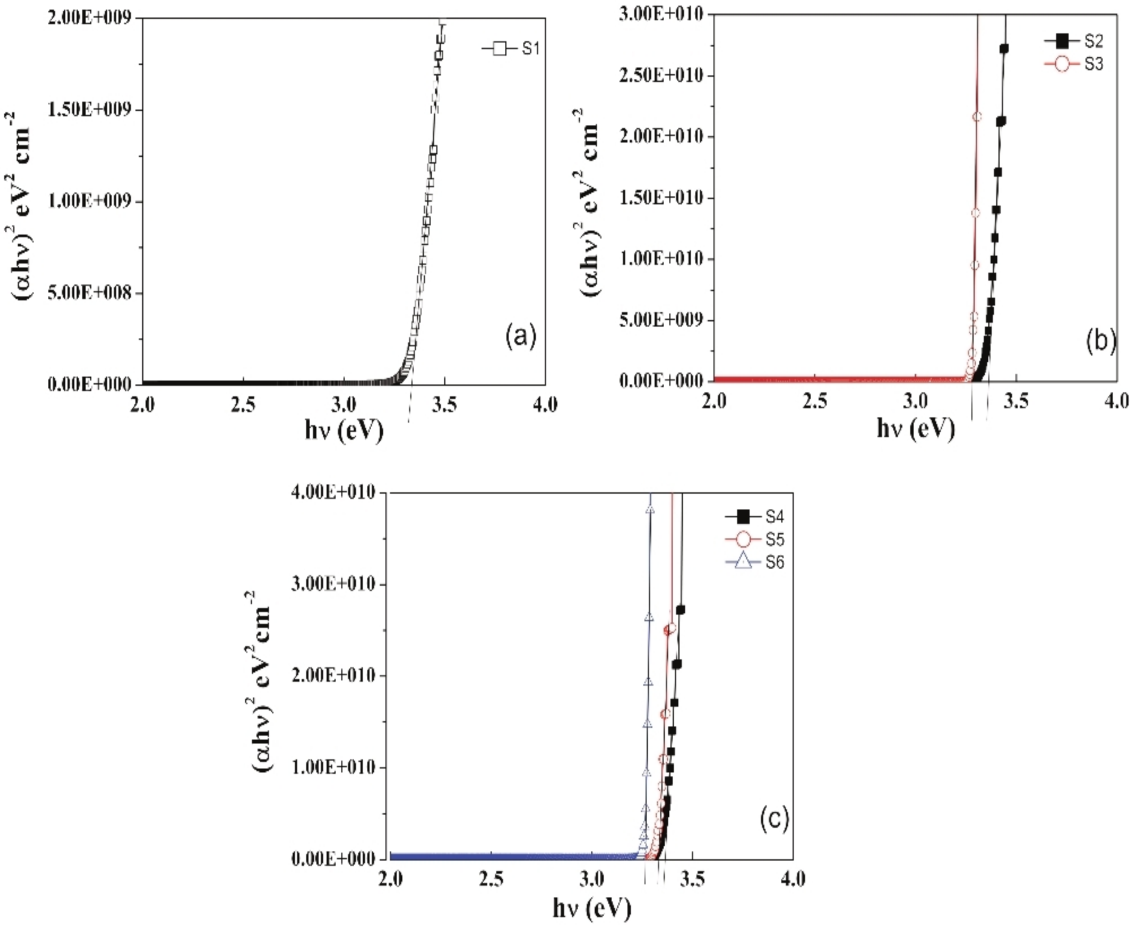

Figure 4.6: $(\alpha h\nu)^2$ v/s $h\nu$ plots for DC reactively sputtered thin films (a) S1 (b)S2 and S3 (c)S4, S5 and S6.

4.3.3.1 Optical energy bandgap

The linear absorption coefficient can be calculated from the expression $\frac{ln(1/T)}{d}$. For a direct band gap semiconductor of allowed band-to-band transition, the optical energy bandgap E_g can be estimated using the relation (Tauc 1974)

$$\alpha = \frac{(h\nu - E_g)^{1/2}}{h\nu} \tag{4.8}$$

E_g is determined by plotting $(\alpha h\nu)^2$ as a function of $h\nu$, and extrapolating the linear region of $(\alpha h\nu)^2$ to zero. Figure 4.6 shows the plot of $(\alpha h\nu)^2$ as a function of $h\nu$. The band gaps of the films are tabulated in the Table 4.4. For the films sputtered with constant working pressure (9×10^{-3} mbar) and different sputter power, optical energy bandgap show decreasing trend indicating the red shift of E_g with the increasing sputter power. This may be because of the variation in the grain size of the films.

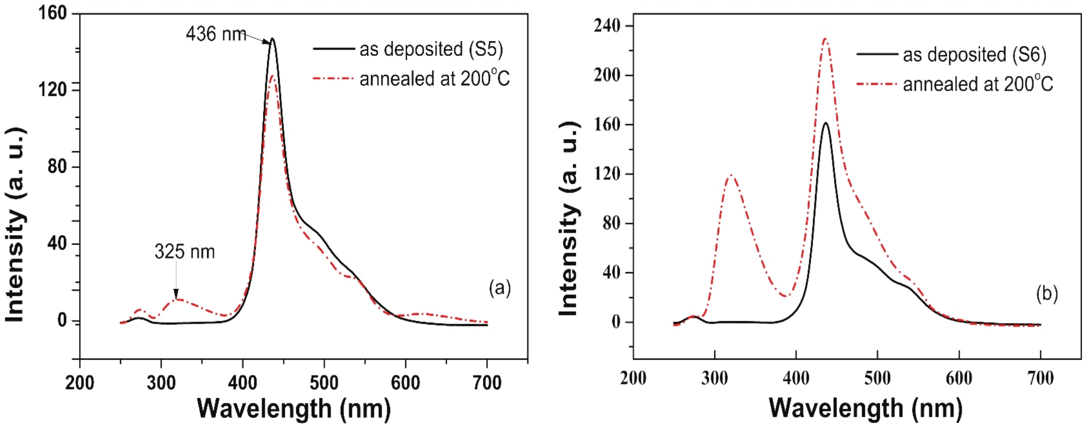

Figure 4.7: PL spectra of sample (a) S5 and (b) S6

4.3.3.2 Photoluminescence Spectra

The photoluminescence spectra of the deposited films were recorded in the wavelength range 250-700 nm. As-deposited films show a weak emission peak around 350 nm, it is near to the excitonic peak of ZnO. In addition to this the films show a strong peak around 436 nm. The films annealed at 200 °C have shown more prominent excitonic emission than the pristine ones. This may be attributed to the improvement in the crystallinity and reduction of defects.

4.4 Properties of RF sputtered ZnO thin films on glass substrates using sintered target

4.4.1 Structural properties

Figure 4.8 shows XRD patterns of the deposited ZnO thin films. The peak at $2\theta = 34.23°$ is almost equal to the standard pattern available (JCPDS no-01-079-0207) for ZnO. All the films show preferred orientation along (0 0 2) planes which is indicated by a intense single peak. In other words, the films are said to have a texture along (0 0 2) direction. The intensity of the (0 0 2) peak increases with the sputter power suggesting the increase in the crystallinity of the deposited films. XRD pattern obtained for the films deposited at 150 W shows some irregular peaks which doesn't belong to ZnO. It may be due to experimental errors. FWHM of the films show considerable decrease with the increase in the sputter power which in turn increases the grain size. Decrease in the FWHM is attributed to the improvement in crystallanity of the films. The lowest grain size obtained for the films deposited with 150 W resulted in getting grain size around 7 nm.

Table 4.5: Summary of the deposition parameters and structural parameters obtained using XRD for the films grown using RF sputtering.

Sample No.	**Sputter power** (W)	**Peak position** $(deg.)$	**FWHM** $(deg.)$	**Grain size** (nm)	**d (Å)**	**Film stress** MPa	**a (Å)**	**c (Å)**
1	300	34.23	0.2880	29	2.616	-1433	3.1106	5.232
2	250	34.23	0.2880	29	2.616	-1433	3.1106	5.232
3	200	34.33	0.3840	21	2.608	-716	3.1018	5.216
5	100	34.37	1.1520	7	2.605	-448	3.0983	5.210

The interplanar spacing d calculated using Scherrer formula (Eqn. 4.1) is in good agreement with the standard value which is 1.60×10^{-10} m for bulk ZnO. The calculated

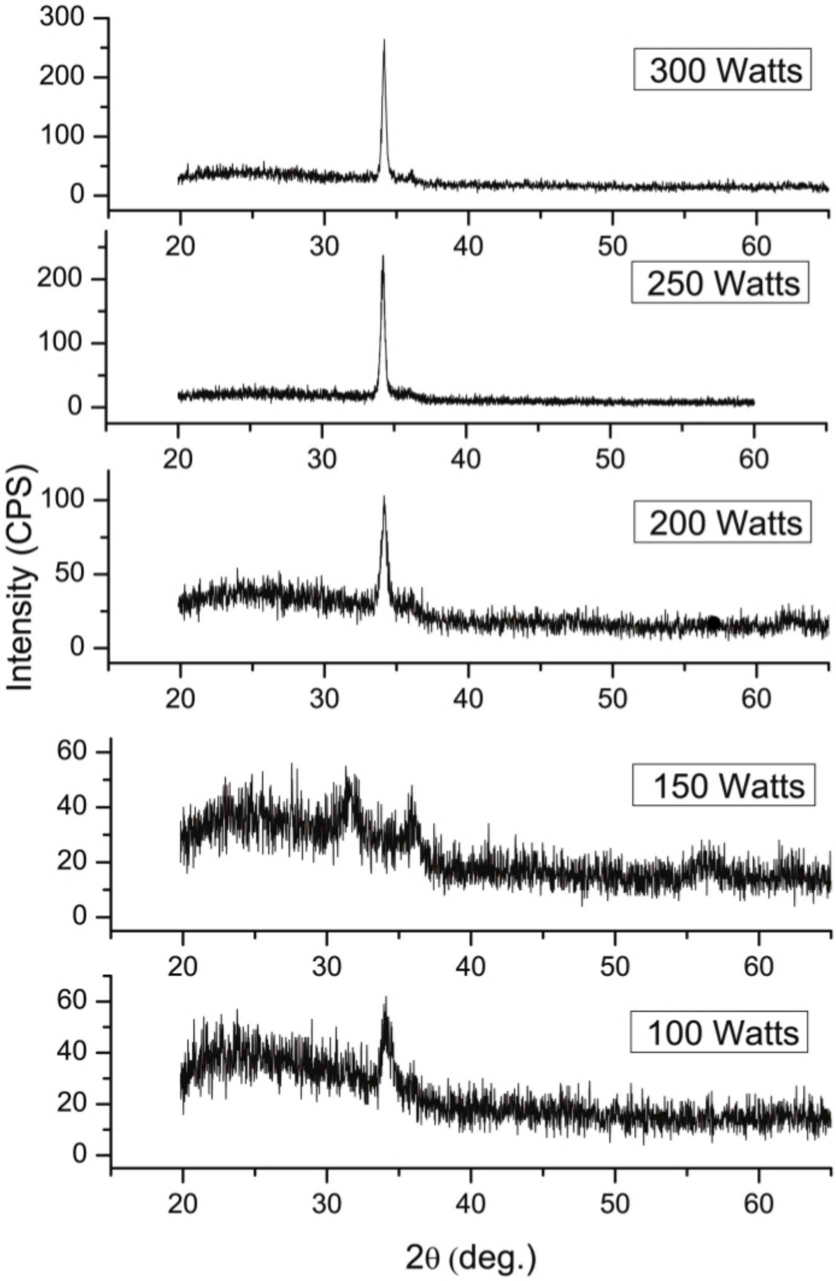

Figure 4.8: XRD patterns obtained for the RF sputtered ZnO thin films deposited at different sputter powers.

values are too close to the standard one indicating less stressed films. The d values shown a small increase with increase in the sputter power due to the presence of residual stresses during the growth process. But the films deposited using reactive sputtering shown more compressive stress than RF sputtered films. The calculated stress values are increasing with the increase in the sputter power. This is in contrast with the one deposited using reactive sputtering.

4.5 Properties of RF sputtered ZnO thin films on quartz substrates using sintered target

4.5.1 Structural and surface morphology

X-ray diffraction patterns of the as-deposited film using RF sputtering and the films annealed in the range 600-1000 °C are shown in Figure 4.9. The peaks corresponding to (1 0 0), (0 0 2), (1 0 1), (1 1 0) and (1 1 2) planes of Wurtzite ZnO were found in as-deposited films. The intensity of the (0 0 2) peak increases with the annealing temperature and found to be maximum for the films annealed at 800 °C, this indicates the increase of preferred orientation in the films. The degree of preferred orientation in the films is roughly estimated from the orientation factor α by the relation $\alpha_{(002)} = \frac{I_{(002)}}{[Sum\ of\ the\ intensities\ of\ other\ prominent\ peaks]}$ (Wang et al. 2010) and found to be 0.079 for the as-deposited films and increases with increase in the annealing temperature. In the present work, the maximum orientation of 0.69 was observed for the films annealed at 800 °C. The increase in the (0 0 2) orientation in the films may be due to the fact that the atoms have enough diffusion activation energy to occupy the correct sites in the crystal lattice at higher temperatures. This leads to the growth of grains with the lower surface energy at high growth⁄annealing temperature (Fujimura et al. 1993; Ye et al. 2002). The FWHM of the films for (0 0 2) planes were found to decrease with the increase in annealing temperature indicating an enhancement of crystallanity due to recrystallization of ZnO films by the supply of sufficient thermal energy. But, as the temperature increases beyond 800 °C, in addition to ZnO phase a secondary phase starts to appear. This is evident from the reflections from (1 1 3), (3 1 3) and (4 2 3) planes corresponding to crystalline SiO_2. At temperatures above 870 °C, ZnO films may turned to be thinner at some areas and SiO_2 turned from normal amorphous phase to tridymite above the annealing temperature 870 °C (Han et al. 2005). At higher temperatures, Zn might have diffused into quartz substrate and Si into ZnO films which is

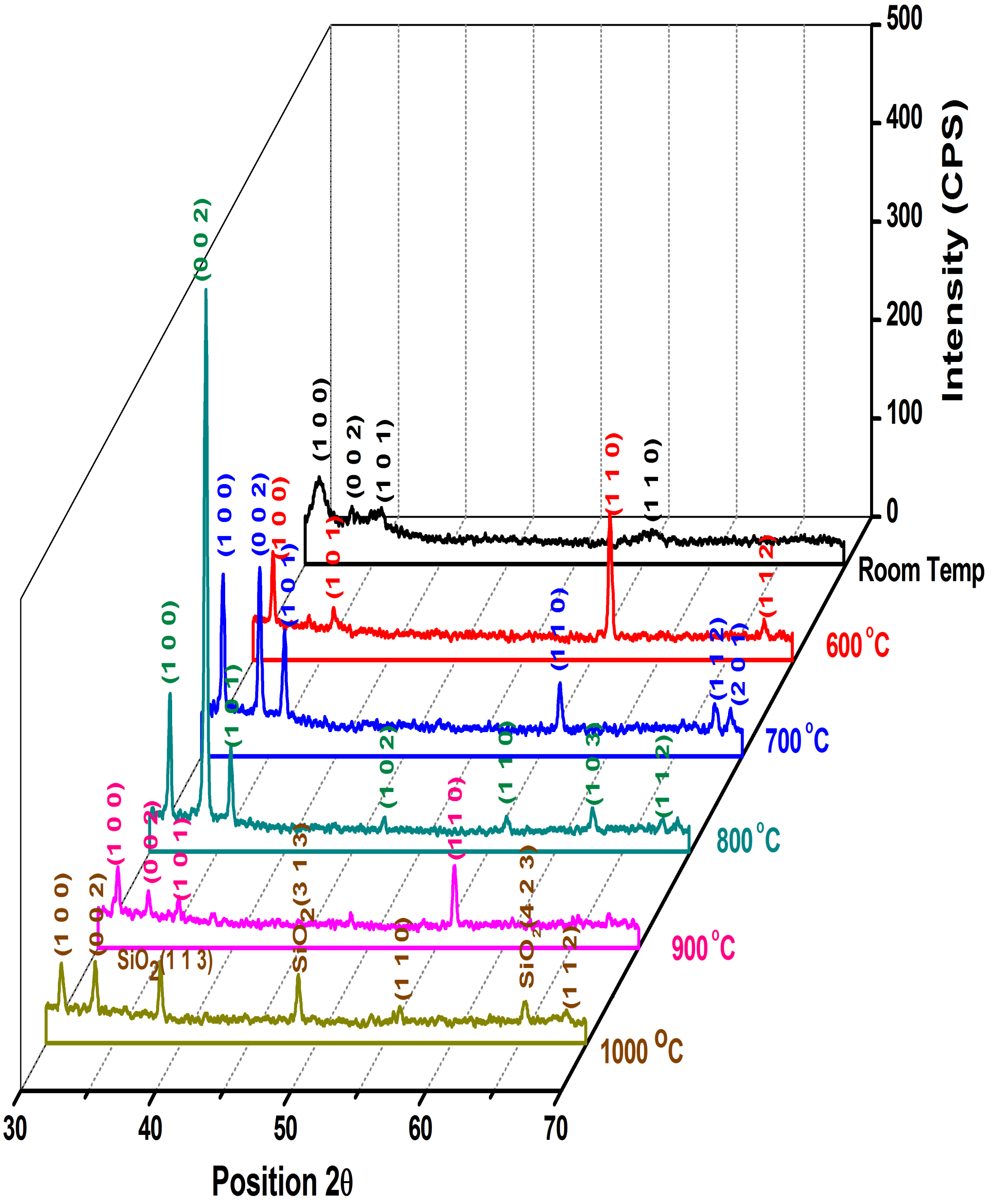

Figure 4.9: X-ray diffraction patterns of as-deposited and annealed thin films on quartz substrates. Reflections from SiO_2 are clearly seen for the thin films annealed at 1000 °C

evident by the increase in the intensity of the peaks corresponding to tridymite phase of SiO_2. The grain size t ((0 0 2) orientation) of the films can be estimated by Scherrer formula (Eqn. 4.1) (Cullity 1978). The grain size of the films is found to increase with the increase in temperature and it is highest for the film annealed at 800 °C. The observed 2θ positions (Table 4.6) for as-deposited and annealed films were less than that of stress free ZnO which is 34.44°. In turn they exhibit the discrepancy in d-value, which is due to the crystal lattice distortion by residual stresses developed in thin films. The calculation of the film stress is based on the biaxial strain model. The strain in the films along the c-axis is calculated using the relation 4.3 and the residual stress in the films which is valid for hexagonal lattice is calculated using the relation 4.4 (Zhang et al. 2009). The residual stress found to have a negative value which indicates a compressive stresses developed in the films. The observed residual stress is maximum for as-deposited film and it decreases as the annealing temperature increases. The minimum stress is obtained for the films annealed at 700 °C. As the annealing temperature increases the atoms of ZnO films have sufficient thermal energy to arrange again and will reduce the stress in the films. Due to the appearance of additional phases at higher annealing temperatures (above 870 °C) the stress values tend to increase. Figure 4.10 shows atomic microscope images of as-deposited and annealed films. The surface morphology of the as-deposited films consists of dense and well packed grains with all possible orientations. At higher annealing temperatures the grains corresponding to (0 0 2) planes starts to appear and the growth of the same increases with further increase in annealing temperature. The films annealed at 800 °C shows highly oriented grains along with the (0 0 2) planes which is confirmed by the presence of grains perpendicular to the plane of the substrate. This was confirmed by XRD pattern for the same film in which it showed a high intense peak corresponding to the (0 0 2) planes. These grains grow perpendicular to the plane of the substrate with the increase in annealing temperature. But, this structure disappears for the films annealed at 1000 °C may be due to the formation of SiO_2 phase in the films annealed at higher temperatures (see magnified images in figure 4.11). The same observation has been made by the XRD analysis. The surface roughness of the films was deduced by AFM images using Nanoscope image analysis software. The average roughness of the as-deposited films was found to be 30 nm and found to decrease with annealing temperature due to recrystallization of ZnO. The minimum roughness was obtained for the films annealed at 800 °C, it may be due to the growth of grains corresponding for (0 0 2) planes only as confirmed by the

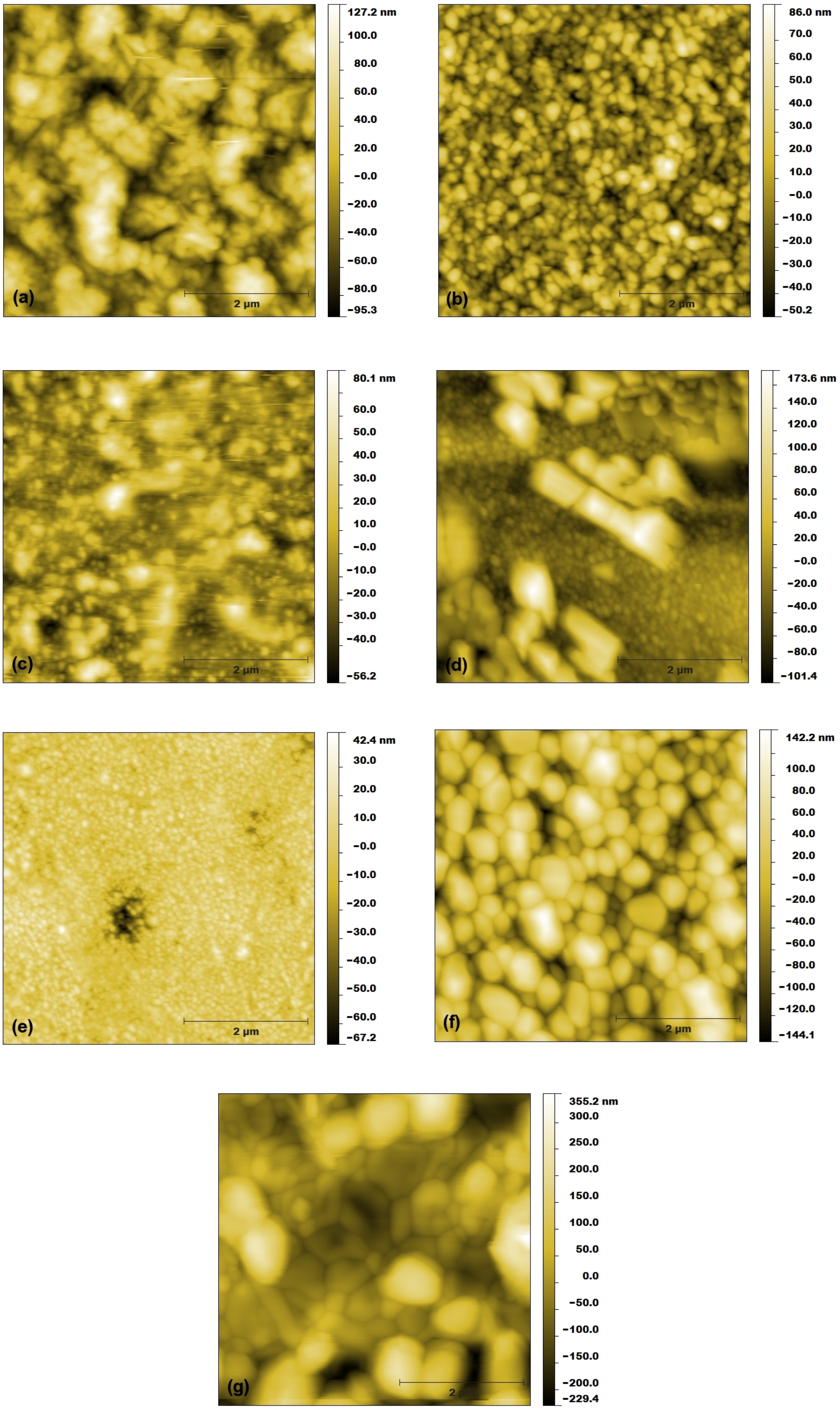

Figure 4.10: Atomic microscope images of (a) as-deposited thin films and those annealed at (b) 400 °C (c)600 °C (d) 700 °C (e) 800 °C (f) 900 °C (g) 1000 °C

AFM images. For higher annealing temperatures the grains grow larger leading to the increase in the roughness (Zhang et al. 2010). The particle diameters were measured using the image analysis software from AFM images. The measured mean diameters were found to increase with the increase in annealing temperature. But, for the films annealed at 800 °C, particle size was minimum because of the presence of (0 0 2) orientation only. Further increase in annealing temperature leads to grain growth. The grain size obtained from XRD spectra corresponds only for the (0 0 2) orientation whereas mean diameter of the particles was calculated from AFM analysis. The structural, morphological and linear optical properties of ZnO films studied in the present work are tabulated in Table 4.6.

4.5.2 Optical properties

4.5.2.1 Linear Optical Properties

Optical transmittance spectra of the as-deposited and annealed thin films are shown in Figure 4.12. As-deposited films and films annealed below 900 °C show transmittance above 75% in the range 400-900 nm. The sharp fall in the transmittance near the absorption edge around 370 nm indicates high crystalline and direct band gap nature. These films also characterized by interference fringes which reveal that the deposited films are uniform with very less surface roughness (Swanepoel 1984). For the annealing temperature above 900 °C the % transmittance decreases drastically to an average transmittance around 40% and the films turn milky for samples annealed above 900 °C. The transmittance of the films is affected by two factors namely, surface scattering and grain boundary scattering. As the annealing temperature increases above 800 °C the grains grow larger thereby increasing the roughness of the films. Also, the grain boundaries become irregular because of the formation of SiO_2 phase in some regions of the films as confirmed by XRD and AFM results. So transmittance of the films annealed at 900°C and 1000 °C show very drastic decrease in their values. For a direct band gap semiconductor, the allowed band-to-band transition, the optical energy band gap E_g is estimated using the relation 4.8 (Tauc 1974; Mott and Davis 1979). The optical band gap for the deposited films can be estimated by plotting $(\alpha(h\nu))^2$ as a function of $(h\nu)$,

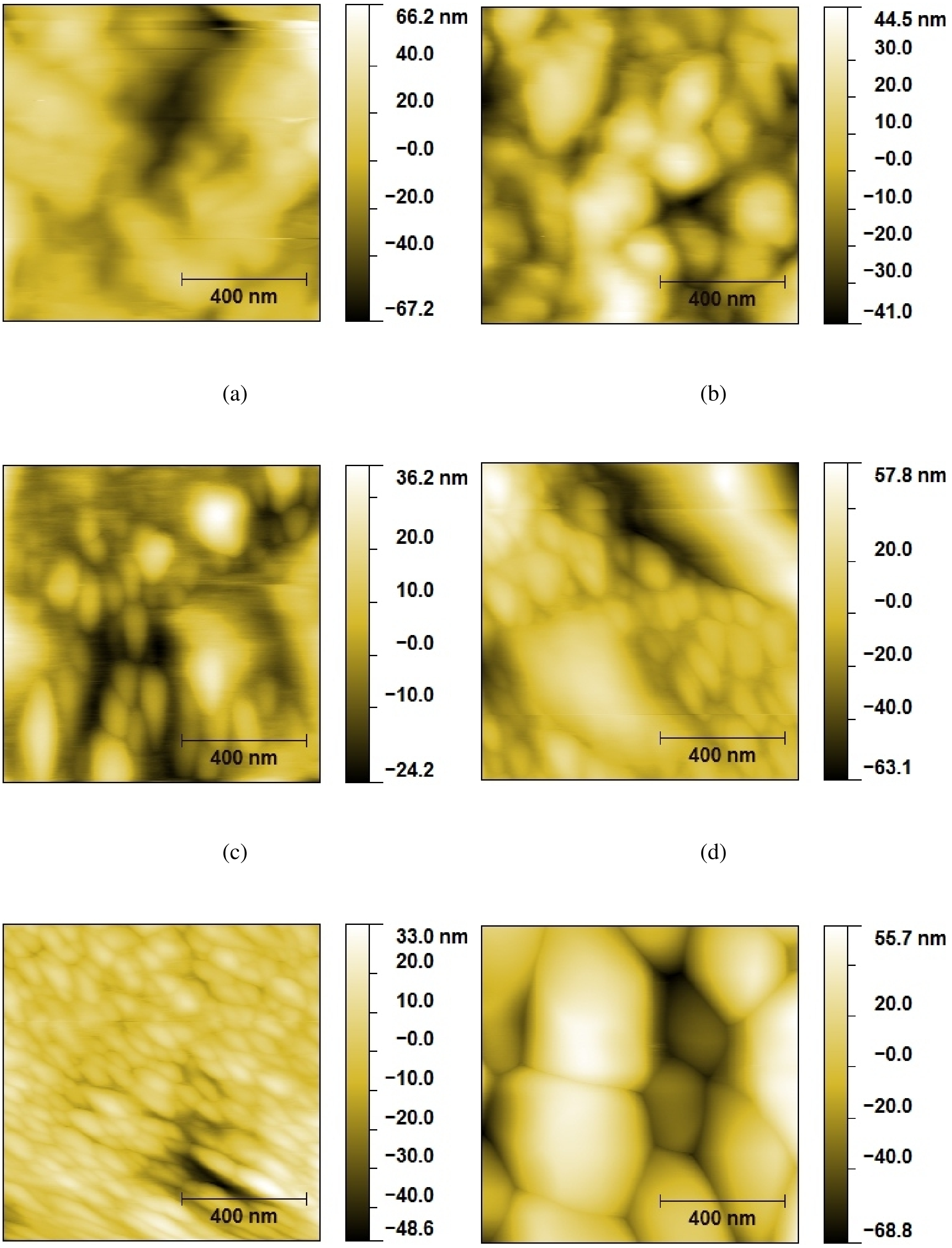

(a) (b)

(c) (d)

(e) (f)

Figure 4.11: Atomic microscope images of (a) as-deposited thin films and those annealed at (b) 400 °C (c) 600 °C (d) 700 °C (e) 800 °C (f) 900 °C (g) 1000 °C

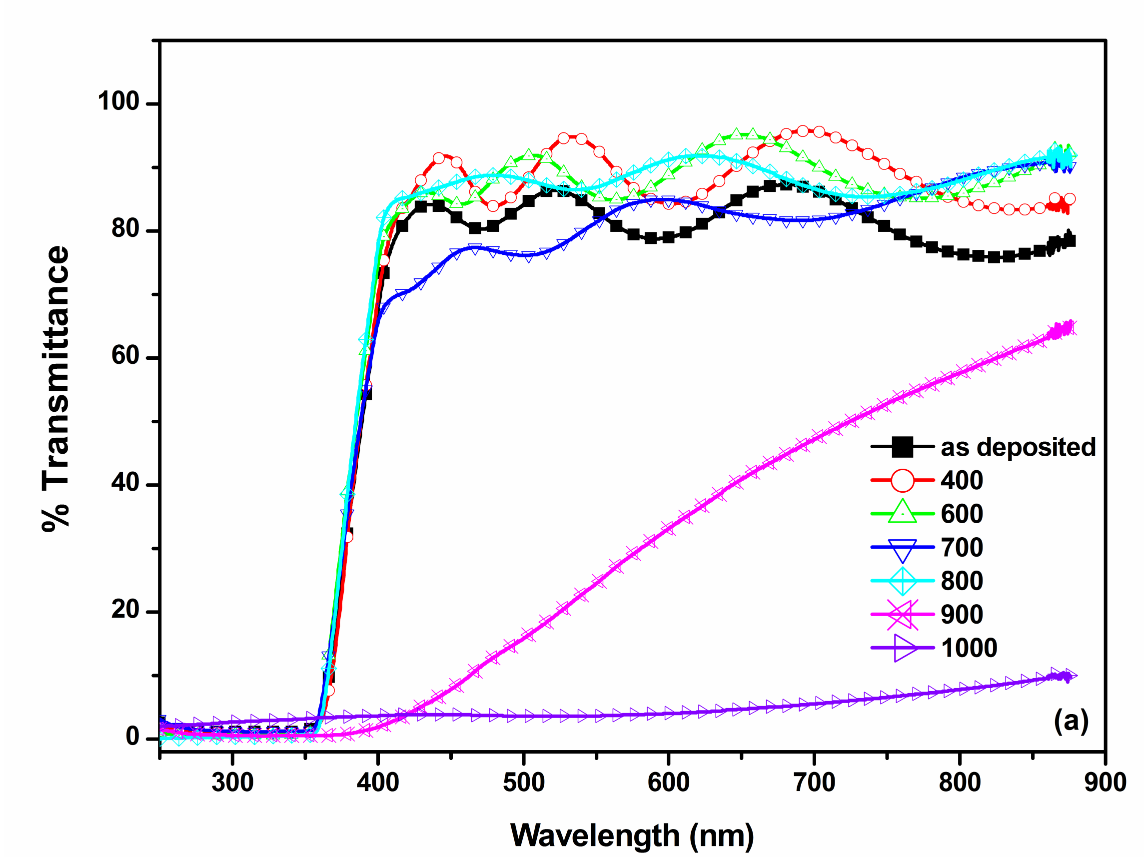

Figure 4.12: Optical transmittance spectra of as-deposited and annealed ZnO thin films on quartz substrates.

and extrapolating the linear region of $(\alpha(h\nu))^2$ to the energy $(h\nu)$ where $(\alpha(h\nu))^2$ corresponds to zero (Tauc 1974; David and Mott 1970; Tan et al. 2005). The band gap of the deposited films was found to be 3.37 eV for as-deposited film and decreases with annealing temperature except for the film annealed at 800 °C. The decrease in the band gap may be due to the increase in the grain growth in the annealed films. The exponential law which empirically describes the behavior of linear absorption coefficient α_o near the band edge in the energy region of $(h\nu) < E_g$ is given by (Srikant and Clarke 1997)

$$\alpha_o(h\nu) = AE_o^{3/2}exp(h\nu/E_o) \tag{4.9}$$

The width of the localized states in the band gap is described by empirical value E_o

which can be calculated by (Srikant and Clarke 1997; Aghamalyan et al. 2003)

$$E_o = [\Delta ln(\alpha)/\Delta ln(h\nu)]^{-1} \tag{4.10}$$

The values of the E_o found to decrease with increase in annealing temperature and

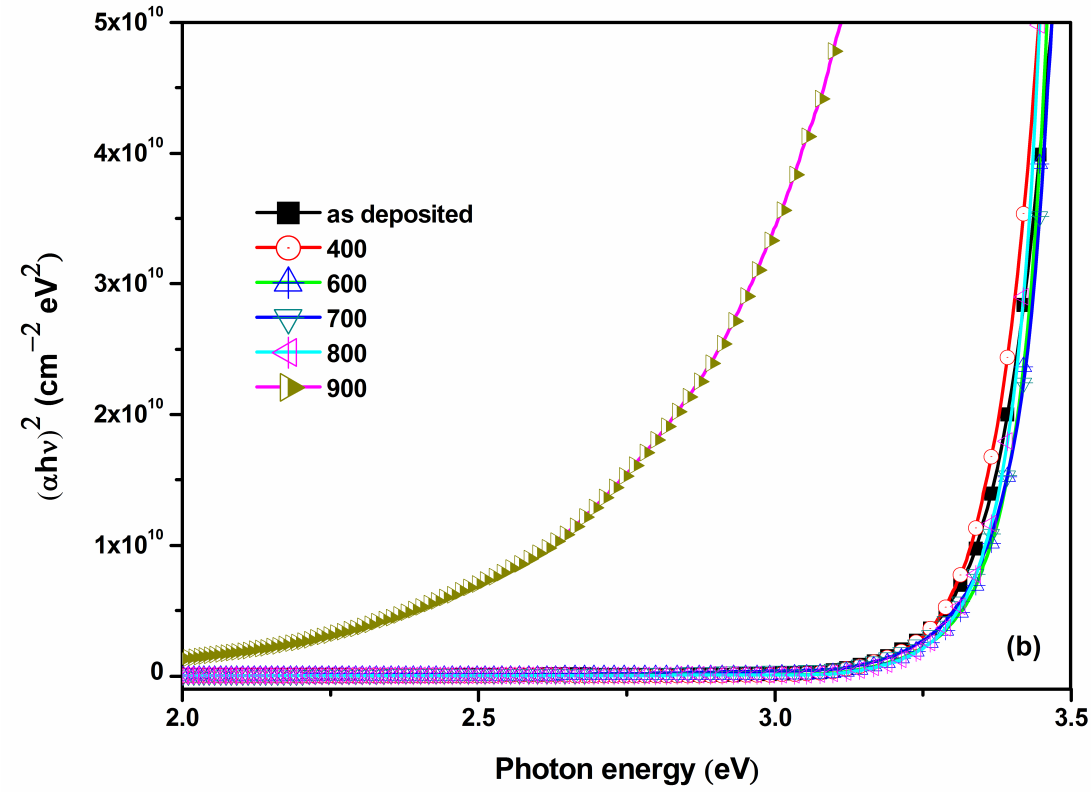

Figure 4.13: Tauc plots to calculate energy gap of as-deposited and annealed ZnO thin films on quartz substrates

found minimum for the films annealed at 800 °C. E_o increases for further increase in the annealing temperature indicating the presence of other phases in the films.

4.5.2.2 Nonlinear Optical Properties

In order to examine the intensity dependence of nonlinear absorption and refraction process for a series of ZnO films deposited on quartz substrates, open aperture and closed aperture z-scan experiments were carried out at an input intensity of 8.9×10^2 W/cm^2. The thickness of deposited film is found to be 553±20 nm which is less than

Table 4.6: Structural, morphological and linear optical properties of ZnO films on quartz substrates

Sl. No.	Annealing Temperature (°C)	$2\theta_{(002)}$ (deg.)	$d_{(002)}$ $\AA$	σ (GPa)	Orientaion factor α_{002}	Grain size by XRD (nm)	Avg. surface roughness R_a (nm)	Mean particle size by AFM (nm)	E_g (eV)	E_o (meV)
1	28	33.43	2.680	−7.00	0.08	29	30	87	3.37	50
2	400	−−	−−	−−	−−	−−	14	116	3.36	47
3	600	34.13	2.626	−2.22	0.04	32	13	137	3.36	46
4	700	34.31	2.613	−1.01	0.34	35	34	132	3.27	40
5	800	34.15	2.625	−2.08	0.68	49	6	46	3.40	35
6	900	33.71	2.658	−5.04	0.15	35	36	237	2.83	281
7	1000	34.59	2.667	−5.86	0.16	43	71	469	−−	−−

the Rayleigh length Z_R for all samples and thus approximation of thin sample is valid (Sheik-Bahae et al. 1989). The open aperture z-scan traces obtained for as-deposited and annealed (in the range 400-1000 °C) ZnO thin films are shown in figure 4.14. These scans revealed a perfectly symmetric open aperture z-scan profiles. When the films were at far field (away from the focus), the laser intensity is low. As the sample translates towards focus, transmittance decreases. The transmission dip decreases further at the focus (z=0) due to the increase in input intensity I_0. Nonlinear absorption can be classified in to two basic processes: saturable absorption also known as negative type of absorption and reverse saturable absorption also known as positive type of absorption. In saturable absorption (SA) with increase in intensity, the transmittance increases and the excited states attains saturation due to their long life time. In reverse saturable absorption (RSA) on the other hand, the molecules in ground state and excited states can absorb the incident photons of same wavelengths and the absorption of excited states will be larger than that of the ground state. In other words, the trans-

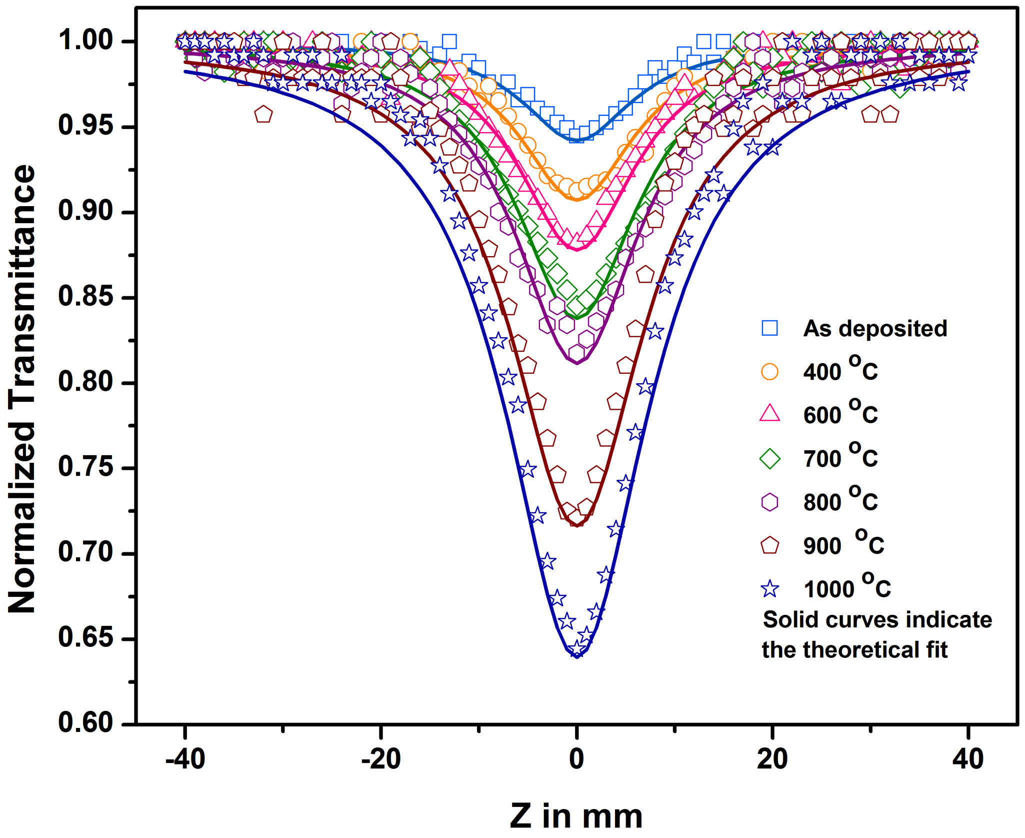

Figure 4.14: Open aperture z-scan traces of as-deposited and annealed ZnO thin films on quartz substrates. Solid line depicts theoretical fit.

mission decreases with increase in intensity. In the present case, with the increase in annealing temperature, well defined normalized dip (valley) at focus (z=0) is observed and indicates that the films exhibits RSA. In semiconductors RSA results mainly due to the nonlinear mechanisms such as two-photon absorption (TPA), free carrier absorption (FCA), nonlinear scattering or with the combination of these processes.

In semiconductors TPA is allowed, when the incident light source energy $h\nu$ is less than the direct band gap energy E_g but, greater than $E_g/2$. The TPA vanishes when $h\nu < E_g/2$ for reasons of energetics (Boyd 2008). For $h\nu < E_g$ the nonlinear response involves virtual processes and the two-photon process is much stronger than one-photon process (Boyd 2008). In the present case, as the incident laser source energy is equal to 1.96 eV which is less less than the $E_g \approx 3.3$ ev for ZnO films, the above required condition is fulfilled. Further if the nonlinearity is due to TPA alone, the nonlinear absorption coefficient calculated from open aperture z-scan trace should be independent of on-axis input intensity I_0 (He et al. 1998). But from figure 4.15, the nonlinear absorption coefficient β_{eff} decreases with increase in on-axis input intensity I_0 for the films. The fall of β_{eff} with I_0 is the consequence of sequential two-photon absorption (Poornesh et al. 2009). Zhang et al. (1999) reported that the nonlinear absorption in ZnSe, ZnO and ZnS is due to two-photon induced FCA along with TPA. Compared to TPA, FCA is a weak process and hence its contribution to the nonlinear absorption is relatively less (Irimpan et al. 2008a). Thus, we can infer that the nonlinear absorption in as-deposited and annealed ZnO thin films is due to the consequence of TPA and weak FCA assisted RSA process. Closed aperture z-scan measurements were

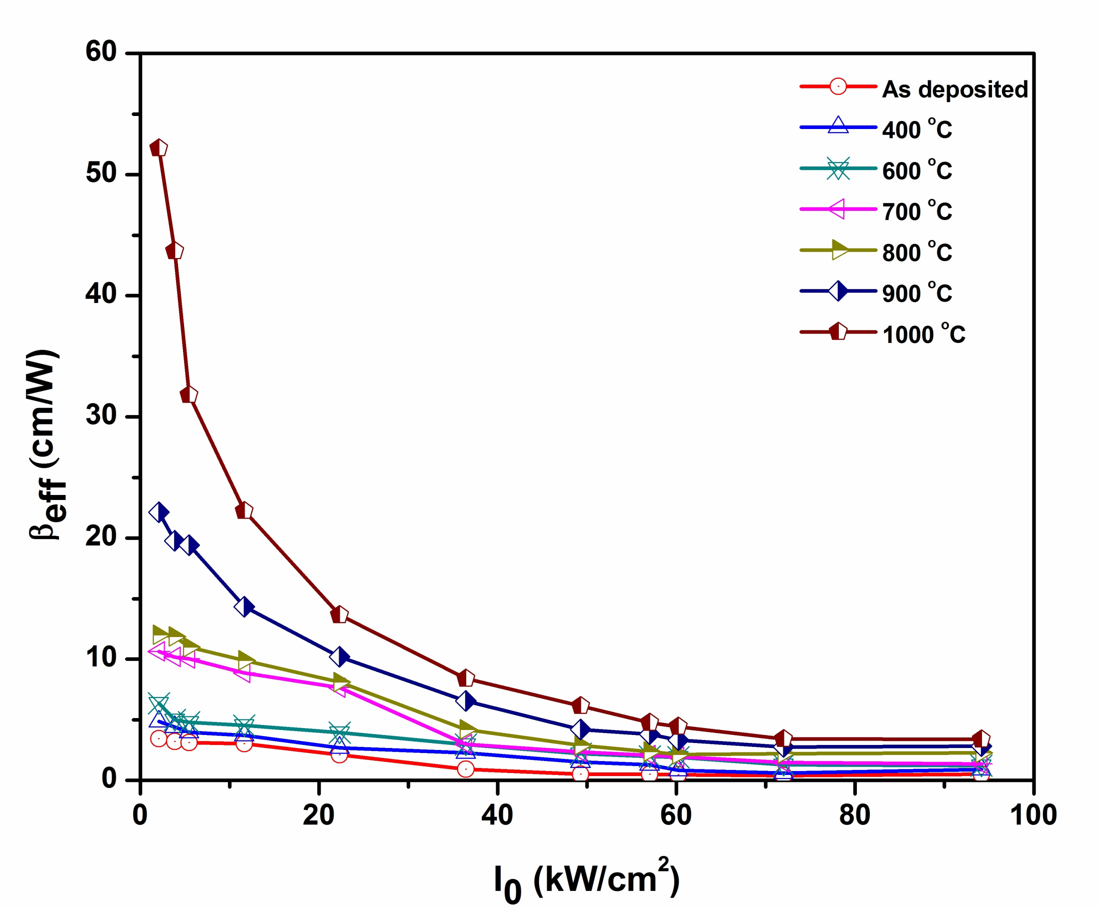

Figure 4.15: Nonlinear absorption coefficient β_{eff} v/s on-axis input intensity I_0 of ZnO thin films.

carried out in order to determine the sign and magnitude of nonlinear refractive index n_2 of as-deposited and annealed ZnO thin films. Figure 4.16 illustrates the closed aperture z-scan traces for the films. The normalized closed aperture z-scan curve exhibits a pre-focal transmittance maximum (peak) followed by a post-focal transmittance minimum (valley). This peak-valley signature indicates the self-defocusing property and it is represented by negative nonlinear refractive index n_2. The sign of the nonlinear index of refraction n_2 of a sample is thus immediately clear from the shape of graph. The sensitivity to nonlinear refraction is entirely due to aperture, and absence of aperture completely eliminates the effect (Sheik-Bahae et al. 1989). Since closed aperture data obtained from z-scan is affected by both nonlinear refraction and nonlinear absorption components, the determination of nonlinear refractive index n_2 is not straight forward

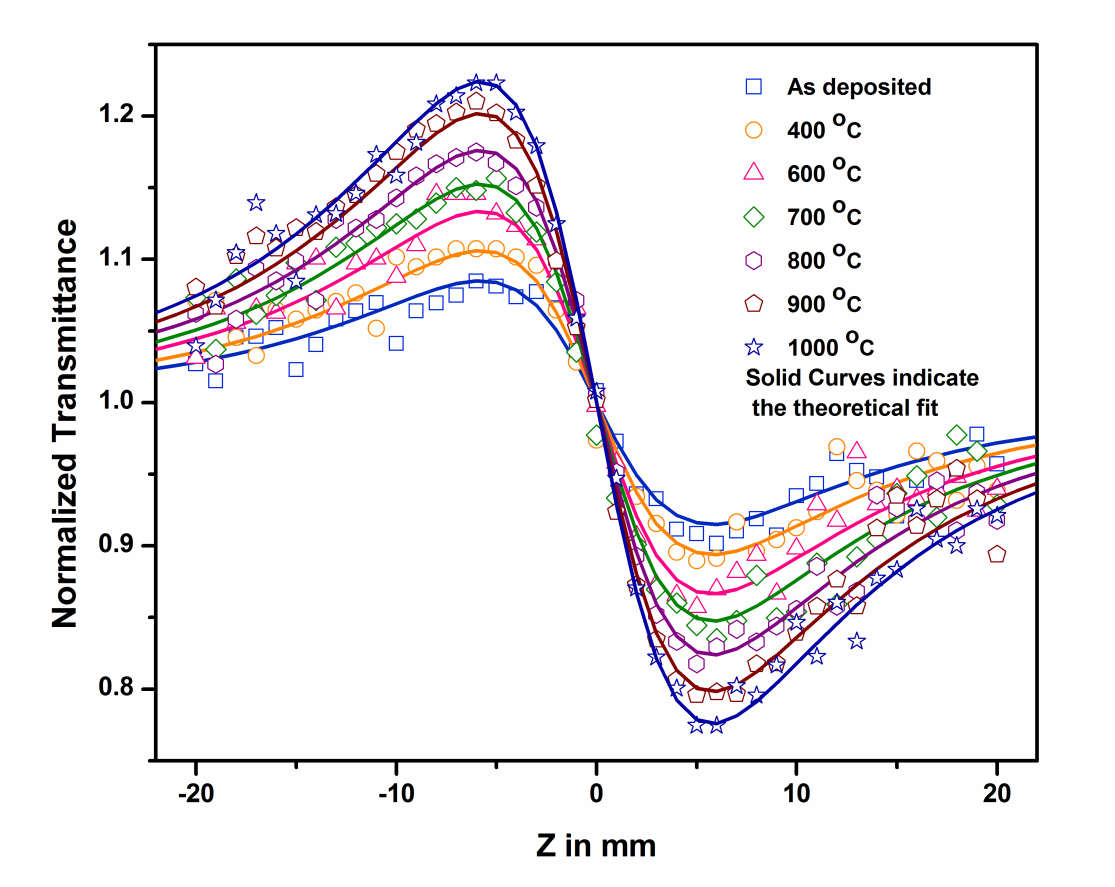

Figure 4.16: Closed aperture z-scan traces of as-deposited and annealed ZnO thin films on quartz substrates. Solid line depicts theoretical fit.

from the closed aperture z-scan data. Hence, it is necessary to separate the nonlinear absorption components from the nonlinear refraction so as to extract pure nonlinear refraction. Figure 4.16 is the closed aperture z-scan trace of films. The physical origin of nonlinear refraction can be electronic, molecular, electrostrictive or thermal in nature. The closed aperture z-scan curves for film samples show a peak-valley separation of 1.9 Z_R. A peak-valley separation of more than 1.7 times the Rayleigh range (Z_R) is the clear indication of thermal nonlinearity and indicates the observed nonlinear effect is the third-order process. The difference in peak-valley normalized transmittance ΔT_{p-v} can be defined as the difference between the normalized peak and valley transmittances $T_p - T_v$. The variation of ΔT_{p-v} quantity as a function of is given by (Sheik-Bahae et al. 1989, 1990)

$$\Delta T_{p-v} = 0.406(1-S)^{0.25}|\Delta\Phi_0| \tag{4.11}$$

where $\Delta\Phi_0$ is the on-axis phase shift, S= 1- exp(-2r_a^2/ω_a^2) is the aperture linear transmittance, r_a is the radius of the aperture and $\omega_a^2 = \omega_0^2(1+(z_a/z_R)^2)$ is the beam waist on the aperture, ω_0 is the beam waist at the focus and z_a is the distance between the aperture and the focal point, $z_R = \pi\omega^2/\lambda$ is the Rayleigh length of the beam with wave vector k. The nonlinear refractive index $\gamma(m^2$/W) is given by the formula (Sheik-Bahae et al. 1989, 1990)

$$\gamma = \frac{\Delta\ \Phi_0\lambda}{2\pi L_{eff} I_0}(m^2/W) \tag{4.12}$$

The third-order nonlinear susceptibility $\chi^{(3)}$ is a complex quantity given by,

$$\chi^{(3)} = \chi_R^{(3)} + \chi_I^{(3)} \tag{4.13}$$

where $\chi_R^{(3)}$ and$\chi_I^{(3)}$ are the real and imaginary parts respectively and given by,

$$\chi_R^{(3)}(esu) = 10^{-4}\frac{\varepsilon_0 c^2 n_0^2}{\pi} n_2(cm^2/W) \tag{4.14}$$

and

$$\chi_I^{(3)}(esu) = 10^{-2}\frac{\varepsilon_0 c^2 n_0^2 \lambda}{4\pi^2}\beta_{eff}(cm/W) \tag{4.15}$$

where ε_0 is the vacuum permittivity and c is the light velocity in vacuum. We conducted z-scan experiment on the bare quartz substrates and found negligible contribution both for nonlinear refraction and nonlinear absorption at the input intensity used. Therefore any contribution from the plane quartz slide to the observed nonlinearity is negligible at the input intensity used. The obtained values of nonlinear refractive index n_2, nonlinear absorption coefficient β_{eff} and the real and imaginary parts of the third-order nonlinear susceptibility $\chi_R^{(3)}$ and$\chi_I^{(3)}$ of as-deposited and annealed ZnO thin film samples are given in Table 4.7. Some of the recently reported nonlinear materials under cw laser excitation are given in Table 4.8. To the best of our knowledge, the estimated values of β_{eff}, n_2 and $\chi^{(3)}$ of as-deposited and annealed ZnO thin films are the highest among the reported values till date.

The dependence of nonlinear absorption coefficient β_{eff} and nonlinear refractive index n_2 annealing temperature was also studied. Figure 4.17 shows the variation of β_{eff} and n_2 as a function of annealing temperature. The β_{eff} and n_2 increases with the annealing temperature. This may be attributed to the fact that with the increase in annealing temperature, the grain size increases due to thermal expansion and hence results in increase in third-order optical nonlinearity. From the open aperture and closed aperture z-scan traces (Figure 4.14 and 4.16), it is clearly seen that the enhancement in the nonlinearity is observed for the films annealed at higher temperatures. The grain size determined by XRD for the as deposited and annealed (400-1000 °C) films increases from 29 nm to 49 nm and hence it comes under weak quantum confinement regime (Irimpan et al. 2008a). Thus with the increase in temperature and grain size the nonlinearity enhances which is due to the size dependence enhancement of exciton oscillator strength (Irimpan et al. 2008a). At the annealing temperature above 900 °C, the value of E_0 increases rapidly and the nonlinearity increases abruptly due to the inter-

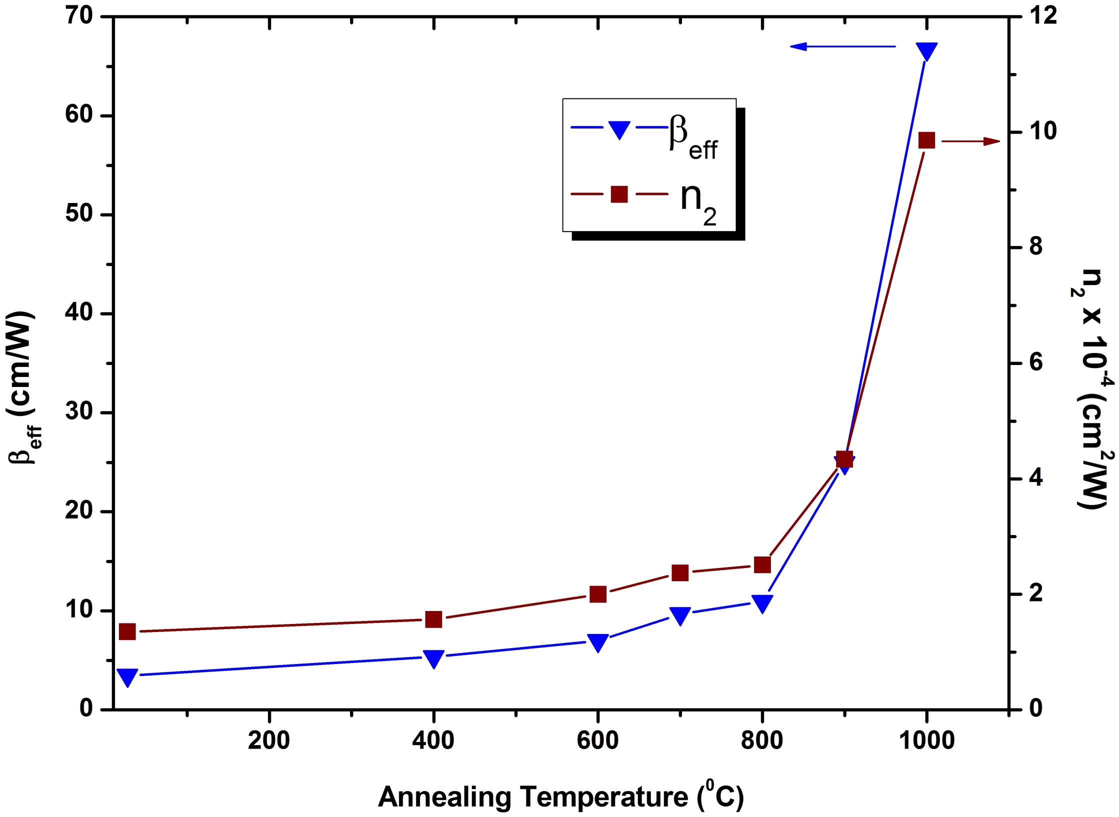

Figure 4.17: Temperature dependence of nonlinear absorption coefficient β_{eff} and n_2 of ZnO thin films.

diffusion of SiO_2 substrates and ZnO films and thus broadens the localized states (Han et al. 2005). For the films annealed at 900 °C and 1000 °C, the $\chi^{(3)}$ value increases rapidly due to the interfacial state enhancement which is clear from XRD and AFM analysis of the samples. Further, with the interdiffusion of Zn nano crystallites into SiO_2 substrate, the local field effects and the interband electrons transitions from the interfacial states to the unoccupied states near the Fermi level will abruptly increases the nonlinear absorption (Feil et al. 1999; Xie et al. 2003). The interference fringes were not observed for the samples annealed at 900 °C and 1000 °C and the transmittance decreases in comparison with the samples annealed at lower temperatures, which infers that the diffusion of Zn in to SiO_2 is high at 1000 °C and this increases the interface area (Han et al. 2005). Han et al. (2005) studied the optical nonlinearity of ZnO micro crystallite films of thickness 20-50 nm developed by sputtering technique under

Table 4.7: Third-order nonlinear optical and optical limiting parameters of ZnO thin films on quartz substrates.

Sl. No.	Annealing Temperature (°C)	β_{eff} (cm/W)	n_3 (cm^2/W)	$\chi_R^{(3)}$ (esu) $\times 10^{-3}$	$\chi_I^{(3)}$ (esu) $\times 10^{-3}$	$\chi^{(3)}$ (esu) $\times 10^{-3}$	Opt. lim. Thres. (mW) (approx.)	Opt. Cl. amp. (mW) (approx.)
1	28	3.48	−1.35	−0.98	0.13	0.99	13.5	14.5
2	400	5.35	−1.56	−1.28	0.22	1.30	13.0	14.0
3	600	6.97	−2.00	−1.85	0.32	1.88	12.0	13.0
4	700	9.69	−2.37	−2.22	0.46	2.27	10.5	12.0
5	800	10.93	−2.51	−2.40	0.52	2.46	8.5	10.0
6	900	24.94	−4.34	−4.14	1.20	4.31	5.0	4.5
7	1000	66.7	−9.86	−9.42	3.21	9.95	2.2	2.0

a femto-second Ti:Sapphire laser irradiation in the temperature range 600 °C to 1050 °C . They have reported that when the annealing temperature rises from 950 °C to 1050 °C , β_{eff} and n_2 value increases from 1.2×10^2 cm/GW to 1.1×10^3 cm/GW and 3×10^{-3} cm^2/GW to 1.9×10^{-2} cm^2/GW respectively and increase in nonlinearity is attributed to the interfacial state enhancement. Irimpan et al. (2008a) investigated the nonlinearity of ZnO nano crystallite films of thickness 60-100 nm developed by sol-gel method under a nano second Nd:YAG irradiation for annealed films at temperature range 300 °C to 1050 °C and reported the increase in $\chi^{(3)}$ value from 2.3×10^{-6} esu to 1.3×10^{-5} esu and increase in nonlinearity is attributed to the nano sized structure of the films. For our samples, the β_{eff} and n_2 values increases for as-deposited and annealed (400 to 1000 °C) films. Above 800 °C, $\chi^{(3)}$ value increases rapidly with increase in annealing temperature. At lower temperatures, $\chi^{(3)}$ value is comparatively small, indicating the thermal nonlinearity. With the increase in annealing temperature and grain size, $\chi^{(3)}$ becomes very large due the effects of thermal nonlinearity, enhanced grain size and the interfacial state enhancement. The increase in grain size and formation of interfacial states were confirmed by AFM and XRD analysis. Presence of interfacial states is also confirmed by transmittance spectra in which interference fringes in the 400-900 nm range disappear for the films annealed at higher temperatures. Drastic shrinkage or disappearance of interference fringes is attributed to inhomogeneity in the interface of the film and the substrate (Swanepoel 1984), hence responsible for the interfacial states.

4.5.2.3 Optical power limiting measurements

The development of modern optical technology demands the ability to control the intensity of light and in this aspect optical power limiters have received significant attention. An ideal optical power limiter has a linear transmittance below a threshold and clamps the output to a constant above it, thus providing safety to optical sensors.

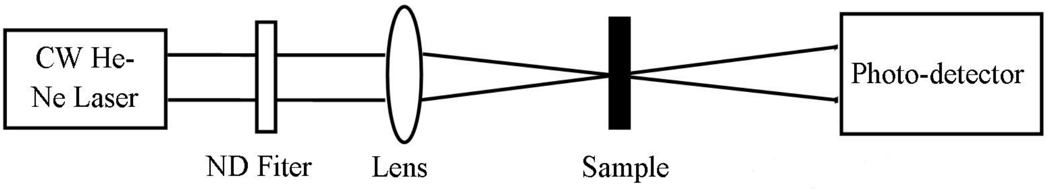

Figure 4.18: A schematic diagram of experimental setup optical limiting measurements.

Optical materials with large nonlinearity, broad band spectral response, fast response time, low limiting threshold, high linear transmittance, stability, etc., are the potential requirements for a good optical limiter. Till date, numerous inorganic and organic materials such as metal nano clusters (Philip et al. 2000) quantum dots (He et al. 2007), self-assembled films, colloids (Irimpan et al. 2008b), ZnS nanoparticles (Deghani et al. 2011), carbon nanotubes (Hyojungyu and Sok 2005) single crystal (Ramamurthy et al. 2011), phthalocyanines (Mathews et al. 2007), porphyrins (Kaladevi et al. 2006), dyes (Zidan et al. 2010), nano composite films (Henari and Cassidy 2011), etc., have been found to possess optical limiting response. In order to measure the critical power of laser beam at which nonlinearity starts to affect the transmission, optical power limiting experiments on as deposited and annealed (in the range 400-1000

Table 4.8: Table depicting the recently reported β_{eff} and n_2 values of different materials with cw laser excitation

Sl. No.	Materials	β_{eff} (cm/W)	n_2 (cm^2/W)
1	Fast green FCF dye (acid blue 3) (Ghaleh et al. 2007)	6.5×10^{-5}	3.2×10^{-8}
2	Phthalocyanines(solutions & films) (Mathews et al. 2007)	-3.25×10^{-3} -1.1	-20×10^{-7} -12×10^{-6}
3	Zinc tetraphenyl porphyrin (Kaladevi et al. 2006)	$--$	-1.4×10^{-7}
4	Basic violet 16 dye (Rashidian et al. 2009)	-1.38×10^{-3}	-2.81×10^{-8}
5	Polymer Nanocomposite films (Frobel et al. 2011)	45.5×10^{-2}	-2.75×10^{-7}
6	Amido black dye (films) (Sreekumar et al. 2007)	$--$	-1.57×10^{-7}
7	Chloroaluminium phthalocyanine (Sathiyamoorthy et al. 2008)	1.3×10^{-3}	-18×10^{-8}
8	2APS single crystal (Ramamurthy et al. 2011)	$--$	-2.42×10^{-8}
9	Acid blue 7 (Geethakrishnan and Palanisamy 2007)	-3.08×10^{-3}	-1.88×10^{-7}
10	Azo dyes (Gayathri and Ramalingam 2008)	-0.23×10^{-4}	-0.54×10^{-8}
11	PDPAlq$_3$ solution (Yassin et al. 2011)	1.12×10^{-4}	-1.76×10^{-8}
12	Au and Ag colloids (Jia et al. 2008)	$--$	-2.23×10^{-8} -1.6×10^{-8}
13	Dye type acid (patent green) (Ara et al. 2010)	8.5×10^{-2}	-4.07×10^{-7}
14	Mn(acac)$_3$ solution (Henari and Mohamed 2008)	1.2×10^{-2}	-1.17×10^{-7}
15	Sudan I dye (He et al. 2007)	$--$	-2.8×10^{-8} -0.3×10^{-6}
16	Nile blue dye (Mohammed and Palanisamy 2006)	1.35×10^{-5}	0.42×10^{-8}
17	Dye doped Liquid crystals (R-Rosales et al. 2008)	$--$	-8.9×10^{-10} 5.9×10^{-10}
18	Polythiophene thin film (Shin and Lee 2000)	-0.139	0.10

°C) ZnO films without aperture (s=1) under cw He-Ne laser illumination was performed. The optical limiting measurements were carried out by placing the sample at the focal plane of the lens and the transmitted power through the film is recorded using power meter for different input powers (shows the schematic of the experimental setup). Figure 4.19 shows the characteristic optical limiting curves as a function of incident power varying from 0.2 up to 20 mW. The optical limiting threshold and optical clamping values of as-deposited and annealed (400-1000 °C) ZnO thin films are given in Table 4.7. The optical limiting can be achieved by means of various nonlinear optical mechanisms, including self-focusing, self-defocusing, induced scattering, induced-refraction, induced aberration, excited state absorption (ESA), two-photon absorption (TPA), photo-refraction and free-carrier absorption (FCA) in nonlinear optical media (Tutt and Boggess 1993). As the films exhibit energy absorbing type of optical

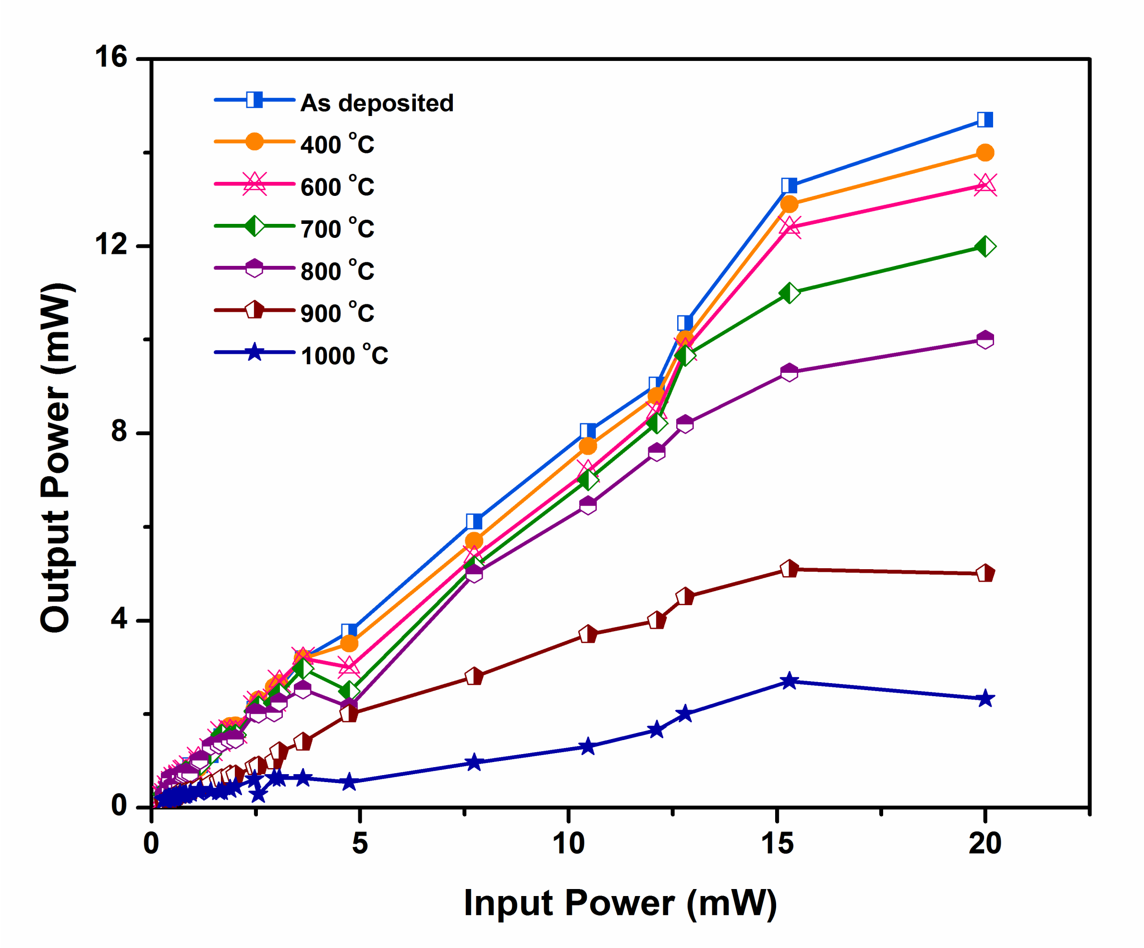

Figure 4.19: Optical power limiting response of ZnO thin films.

limiter, the major nonlinear mechanism employed is RSA and FCA is the process leading to nonlinear absorption in semiconductors. The heating due to laser absorption is the main reason for the changes in the absorption coefficient and optical power limiting effects (Hagen 2001). With increase in annealing temperature and particle size optical limiting is enhanced. The deviations from linearity and the output clamping for the film annealed at 1000 °C occurred at ~1 and ~ 2 mW respectively. Considerable decrease of about 90% was observed in the transmitted power and this reveals that the increase in particle size and annealing temperature has significant effect on optical power limiting and it is in good agreement with the reported values of ZnO nano colloids of different particle size (Irimpan et al. 2008a,b).We could not verify the break down threshold for the film samples above 20 mW due to the limitations with the laser source. The optical power limiting studies reveal that with larger the particle size, better nonlinear absorption occurs and hence it is considered as a good optical limiter.

4.5.2.4 Self diffraction ring patterns

The self-diffraction ring patterns were observed for the as-deposited and annealed ZnO thin films, when the samples were close to the focus. The observed diffraction ring patterns of as-deposited ZnO films recorded using a digital camera is shown in figure 4.20. Continuous wave He-Ne laser at 633 nm wavelength with input intensity 8.9×10^6 W/m^2 was illuminated on the samples by focusing through 5 cm lens. The diffraction rings were observed and photographed at the intensity from 5 mW to 19 mW. As it is seen clearly, with increase in intensity the number of fringes increases. Also, we observed the increase in fringe numbers with the increase in annealing temperature. When the Gaussian laser beam is incident on the sample, the sample absorbs the light and its temperature increases. This increase in temperature results in change of refractive index and induces self-diffraction ring patterns. When the Gaussian laser beam passes through the medium, the maximum induced refractive index change is proportional to the number of fringes (Henari and Cassidy 2011) Thus, the formation of ring pattern is attributed to laser induced refractive index change and thermal lensing. Feeble diffraction pattern was observed for the film annealed at 1000 °C due to the interfacial state

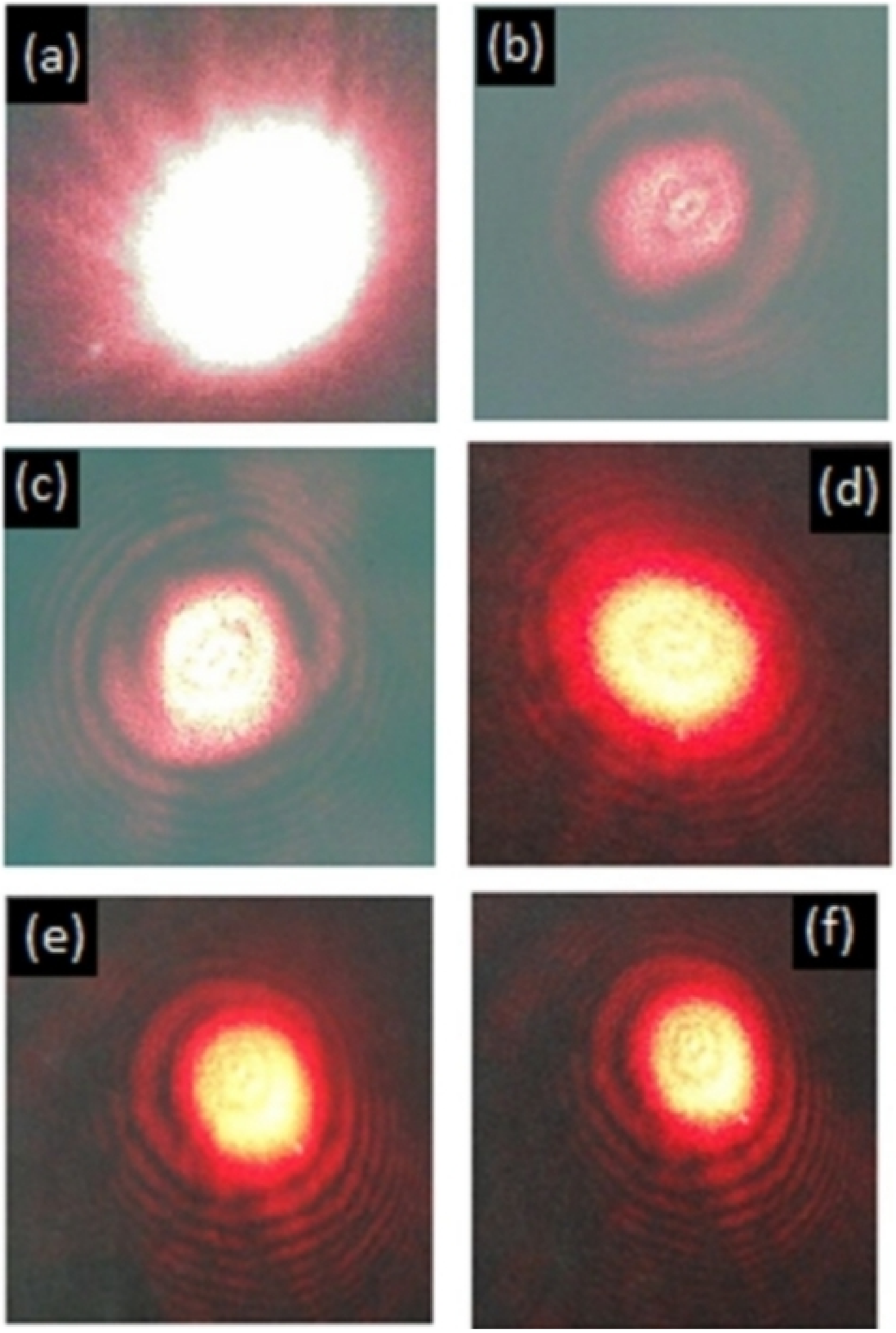

Figure 4.20: Photographs showing (a) absence of diffraction pattern for substrate (b)-(f) self-diffraction ring patterns of as-deposited ZnO thin film with varying intensity.

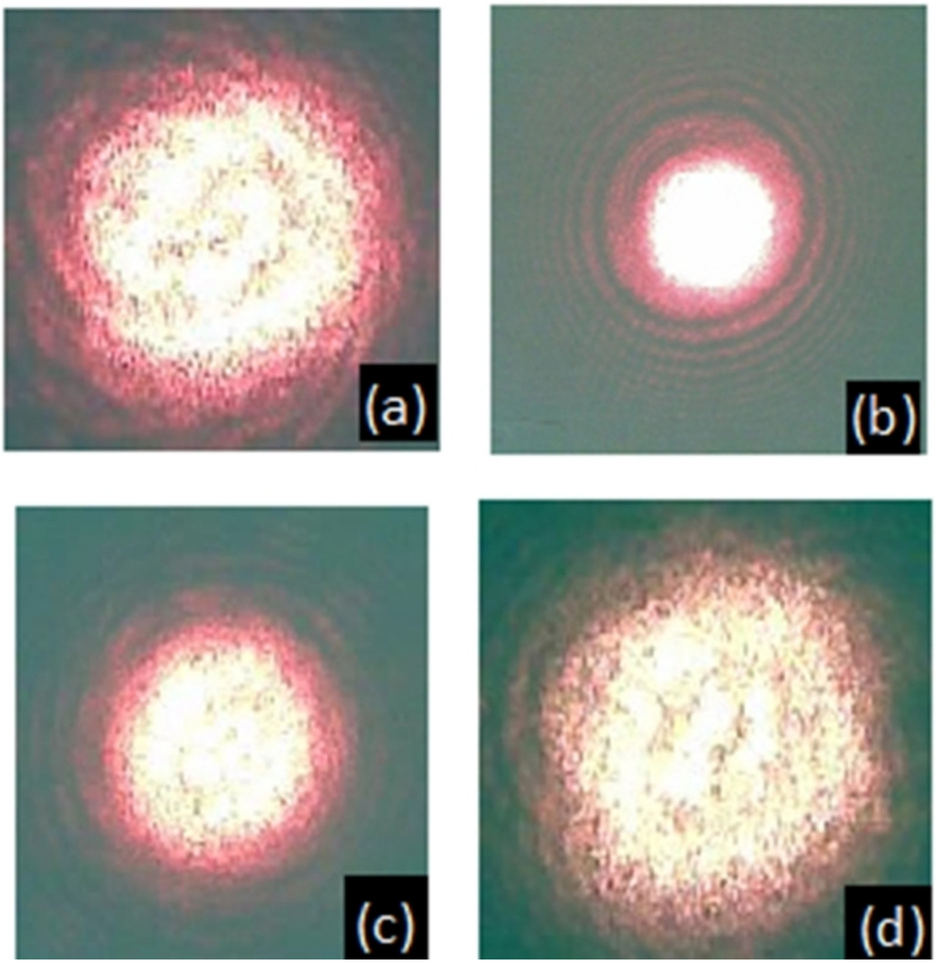

Figure 4.21: Photographs show the laser spot size variation as a function of sample position relative to lens focal point of as-deposited ZnO thin films (a) far from focus, (b) pre-focus transmittance maximum,(c) post-focus transmittance minimum and (d) away from focus.

effect. The variation in the laser beam spot size as a function of sample position relative to focal point of lens was recorded. Figure 4.21 shows the spot size variation of as-deposited film, when the sample was at (a) far from focus, (b) pre-focus transmittance maximum, (c) post-focus transmittance minimum and (d) away from focus. We observed self-focusing and self-defocusing ring patterns with naked eye for all the film samples, which confirms the nonlinear behaviour of the material before conducting the experiment. This can be used as quick check for the nonlinear behaviour of the samples.

4.6 Conclusions

Zinc oxide thin films were deposited (on glass and quartz substrates) using magnetron sputtering technique. The effect of deposition parameters on the structural and optical properties were studied. Undoped ZnO films show good optical transmittance above 85% in 400-900 nm range. The energy band gap of the films decrease with the increase in the sputter power due to increase in the grain size. The characteristic X-ray diffraction peaks for reactively sputtered ZnO were observed and they are well in agreement with the JCPDS. The ZnO films show a strong preferred orientation along c-axis. This was confirmed by a strong peak corresponding to (0 0 2) planes of Wurtzite ZnO. The films show increase in the crystallinty with the sputter power. But, it is found to decrease with the increase in working pressure.

The effects of annealing on structural properties were examined using X-ray diffraction and atomic force microscopy. The grain size increases with the increase in the annealing temperature. The effects of annealing on the structural and nonlinear optical properties of ZnO thin films deposited on quartz substrates were investigated using z-scan technique under continuous wave He-Ne laser at 633 nm. The films were characterized with negative nonlinear refractive index. We observed an increase in induced self-diffraction ring patterns. Also, the films exhibit strong optical power limiting with increase in the intensity of continuous wave laser at the experimental wavelength.

Chapter 5

Growth and properties of Aluminum (Al) doped ZnO thin films

In this Chapter, growth of aluminum doped zinc oxide (AZO) transparent conducting thin films deposited by radio (RF) frequency magnetron sputtering employing zinc oxide and aluminum coaxial targets at room temperature has been discussed. It also presents the preparation and characterization of ZnO/Al/ZnO multilayers by simultaneous RF and DC sputtering.

5.1 Introduction

Transparent conducting oxides are widely used in variety of applications in different kinds of devices. Currently, indium tin oxide (ITO) is the most widely used material for TCO applications like display device electrodes, touch panels and solar cell electrodes for use in liquid crystal display and plasma televisions (Minami 2005). The market for TCOs continues to expand. But, diminishing supply, high cost and toxicity of indium made the supply of requirements difficult and in turn un-stabilizing the supply chain (Jansseune 2005). Researchers are racing against the clock to find alternatives before the supply runs out. The electrical and optical properties of ZnO were studied extensively as it can have low resistivity with excellent optical properties. It can be used as a transparent conducting oxide in many optoelectronic applications. At present, tin doped indium oxide (ITO) is widely used TCO. The expanding use of TCO materials, particularly for the production of transparent electrodes for optoelectronic device applications, is endangered by the scarcity and high price of In. In contrast with ITO, the source materials for a ZnO based TCO are inexpensive, easily available and less toxic. In addition, owing to their better stability in hydrogen plasma than that of ITO, ZnO based TCO thin films can be used for the fabrication of hydrogenated amorphous silicon solar cells (Hupkes et al. 2006; Berginski et al. 2007; Sittinger et al. 2006). ZnO thin films doped with group III elements such as B, Al, Ga, In have been considered as transparent conducting films. Al doped ZnO (AZO) is a most important material due to its low cost, high conductivity and high transmittance. ZnO based TCOs have been investigated extensively by many researchers around the globe (Sim et al. 2010). However, development of large area deposition techniques are still needed to enable the production of TCO films on large area substrates with a high deposition rate. AZO thin films are usually grown by vacuum evaporation, chemical vapor deposition and sputtering. Among all, sputtering is the most widely used technique in obtaining AZO thin films (Chen et al. 2001). Many research groups have used different versions of sputtering methods such as, sputtering with single AZO target in argon atmosphere, co-sputtering of Al and Zn metallic targets in a reactive argon and oxygen atmosphere, co-sputtering of ZnO and Al targets using RF and DC sources. Among these, the last two methods require two magnetron systems. (Minami 2005; Minami et al. 2006; Minami 2012).

Different methods were employed to develop good TCOs by many researchers (Minami 2005; Babar et al. 2008; Ayadi et al. 2007; Sun et al. 2000). The multilayer stacks of TCOs are one such approach employed to improve the properties of TCOs. Kawashima et al. reported improvement of thermal stability in F:SnO_2/ITO stack compared to single layer ITO (2004). Similar stacks of Sn:CdO/$CdIn_2O_4$/Cd_2SnO_4 showed better conductivity than ITO with comparable transparency in the visible region (Martin et al. 2004). Deposition of three layer structure which involves a metallic film embedded between two dielectric layers (D/M/D) has also been investigated. This type of structure allows better TCO with thickness less than a single layer TCO. These D/M/D structures are widely used in energy saving windows as optical filters (Fahland et al.

2001). High refractive index zinc oxide makes it a suitable candidate as a dielectric layer. Few early reports on D/M/D include the development of ZnO/Ag/ZnO & ITO/Ag/ITO (Kusano et al. 1986), ITO/Cu/ITO (Bender et al. 1998), ZnS/Ag/Zns (Ito et al. 2003), TiO_2/Ag/TiO_2 (Leftheriotis et al. 2000) and ZnO/Cu/ZnO (Sahu and Huang 2007). Jyh-Ming et al. reported insertion of thin Al interlayer for the improvement of electrical conductivity of ZnO (2006).

In this chapter we report the deposition of AZO thin films by employing a metallic Al and compacted ZnO targets in a single magnetron. The variation of Al content as a function of sputter power and its effect on optical and electrical properties have been studied.

5.2 Experimental

Radio frequency (RF) (13.56 MHz) is employed to deposit AZO thin films on cleaned glass substrates (Blue Star, Polar Industrial. Corp., India). The two targets, ZnO (50 mm dia., 3 mm thick disc, 99.99%) and metallic Al (50 mm dia., 2 mm thick disc, 99.99%) were fixed coaxially in a single magnetron. The Al target used had a hole with a diameter of 20 mm at the center. The chamber was pumped down to pressure of 5×10^{-6}mbar using a diffusion pump backed with a rotary pump prior to deposition. Pure argon was used as a sputtering gas. The distance between the substrate and the target was adjusted to 50 mm. The deposition was carried out at room temperature with a working pressure of 0.02 mbar and the substrates were not rotated during the deposition. The power applied to the target was varied in steps of 50 W starting from 150 W to 300 W. Multilayers of ZnO/Al/ZnO were deposited on cleaned glass substrates. The ZnO/Al/ZnO multilayer films were successively formed on glass substrates with-

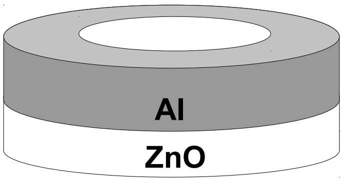

Figure 5.1: Cross section view of the target used to deposit AZO thin films.

out vacuum break using a zinc oxide (99.99% purity, 50 mm dia., 3 mm thick) and metallic Al (99.999% purity, 50 mm dia., 3 mm thick, Alfa Aeser) as targets. High pure argon was used as sputter gas and working pressure was adjusted at 0.001 m bars. Sputtering power was adjusted to 150 Watts for ZnO and 15 Watts for Al. Before each experiment the targets were presputtered for 10 mins to remove contamination on the target surfaces.

The crystal structure of the deposited films was analyzed with JEOL (JDX-8030) X-ray diffractometer using a Cu-K_α radiation. JEOL (JSM-6380 LV) scanning electron microscope was used for surface morphology and EDX analysis of the films. The electrical measurements were carried out using a Keithley Sourcemeter (Model-2400). The optical transmittance measurements were performed using Ocean-Optics UV-Visible spectrometer(USB-2000).

5.3 Properties of Aluminum (Al) doped ZnO thin films

5.3.1 Structural Properties

The X-ray diffraction spectra of the AZO thin films deposited with different sputter powers are shown in Figure 5.2. As we can see the films show a preferred orientation along c-axis indicated by a prominent (0 0 2) peak. As the sputter power increased further, the other reflection which belong to Wurtzite ZnO were observed. Crystallite size t for the films was found using Debye-Scherrer formula Cullity (1978)

$$t = \frac{0.9\lambda}{B\ cos\theta} \tag{5.1}$$

where, λ is the wavelength of the X-ray 0.1540 nm, B is FWHM in radians and θ is Bragg diffraction angle. Crystallite size for the films deposited at 150, 200, 250 and 300 W is found to be 10, 15, 19 and 30 nm respectively. Amount of Al in the films was found using EDX analysis. The Al percentage in the films is found to increase with the sputter power. The lattice parameters a and c were also calculated. Lattice parameter c of the films is found to vary with the sputtering power and it is higher than that of

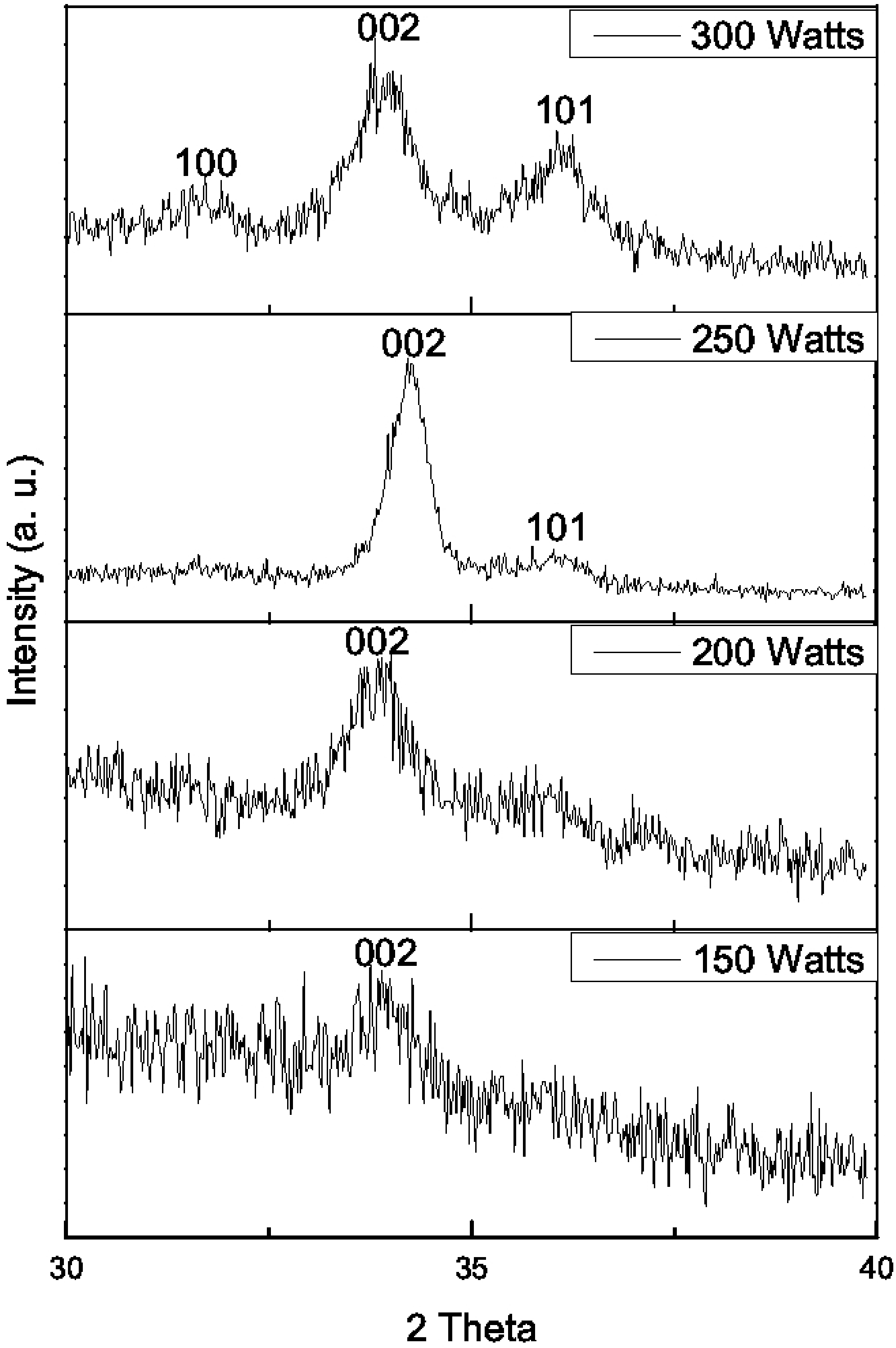

Figure 5.2: XRD patterns of the RF sputtered AZO thin films using a coaxial target.

stress free bulk ZnO and it is varying with Al content. Al doping in ZnO films leads to the decrease in the lattice parameter as the ionic radius of Al^{3+} is lower than that of Zn^{2+}. Thus the addition of Al atoms in the ZnO matrix is expected to shorten the c lattice parameter if Al atoms are substituted to Zn sites (Sharma and Tripathi 2012). Lattice parameter c decreases as the sputter power is increased due to increase in the Al substitution to Zn sites. Above some critical value of Al content, the Al atoms rather than substituting at the Zn sites, may go to the interstitial sites. (Sharma and Tripathi 2012).

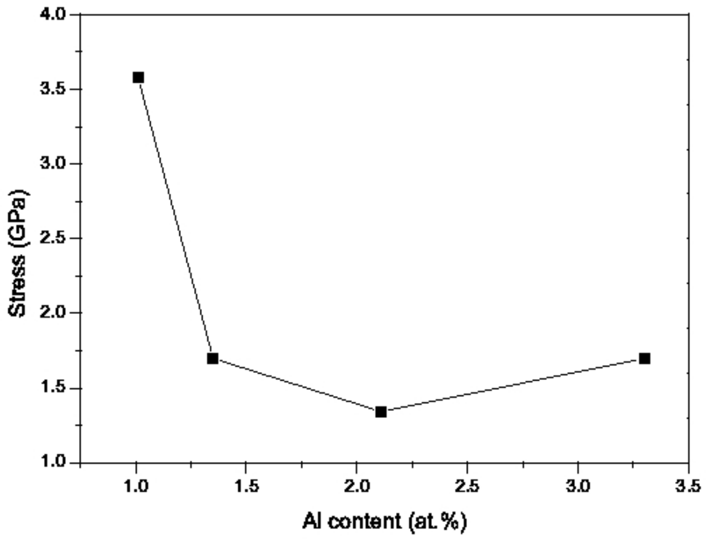

Figure 5.3: Variation of stresses in the AZO thin films with Al content.

Residual stresses generated during the growth process. The strain in the films along the c-axis could be expressed by the formula (Zhang et al. 2009)

$$\epsilon = \frac{(d - d_0)}{d_0} \tag{5.2}$$

where d and d_0 are strained and unstrained lattice co-efficient respectively. The residual stress in the films which is valid for hexagonal lattice is given by (Zhang et al. 2009)

$$\sigma_{film} = \frac{2{c_{13}}^2 - c_{33}(c_{11} + c_{12})}{2c_{13}}.\epsilon \tag{5.3}$$

For the elastic constants c_{ij}, the following values corresponding the stress free ZnO

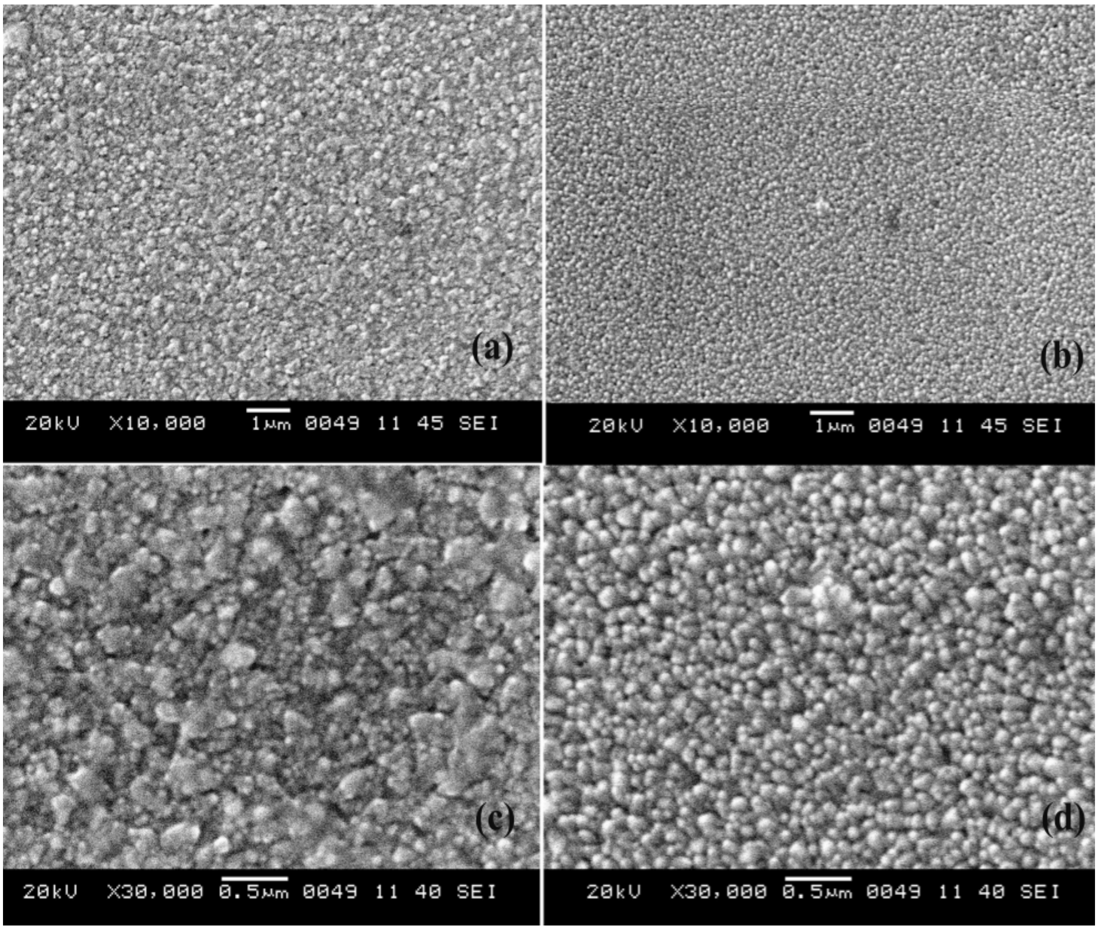

Figure 5.4: SEM images showing surface morphology for the AZO thin films (a) deposited deposited at (a) 300 W (b) 200 W (c) 300 W (higher magnification) (d) 200 W (higher magnification)

were used: c_{11}= 208, c_{33} =213.8, c_{12}=119.7 and c_{13}=104.2 GPa (Cebulla et al. 1998). The residual stress found to have a negative value which indicates a compressive stresses generated in the films during the growth. The variation in film stress with Al content is shown in Figure 5.3. The stress value for 1.01 at.% Al is found to be 3.580 GPa and it decreases as the Al content increases in the films up to 2.11 at.%. For further increase in Al content the stress found to increase. This may be due to the presence of Al interstitials for the films deposited at higher sputter powers. This is also evident from the decreasing c-parameter. Total stresses in the films is composed of intrinsic stress due to

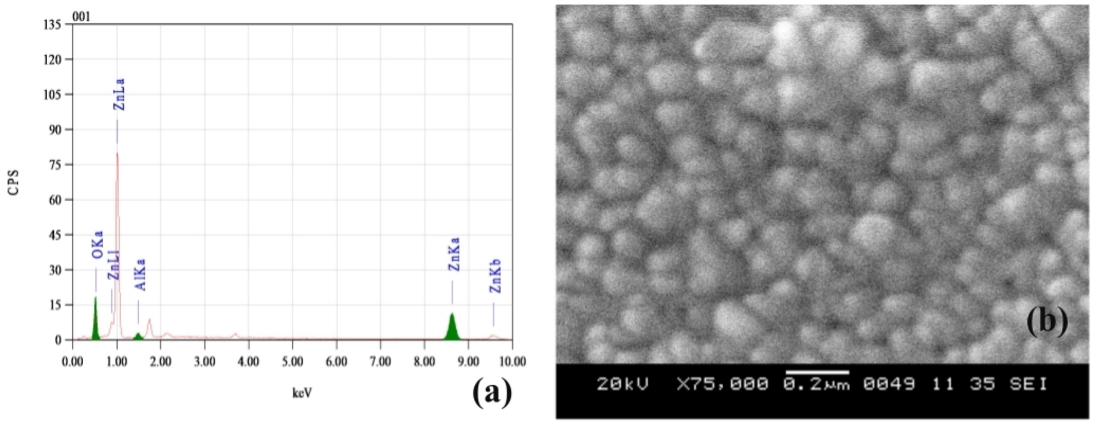

Figure 5.5: (a) EDX spectrum of the AZO thin film (b) high magnification image showing nanograins.

the dopants and defects during the growth and extrinsic stress due to thermal mismatch between substrate and the films. The substrate temperature was maintained constant in all our experiments. Therefore, the change in the stress may be due to Al doping and change in the defects in the films.

Scanning electron microscope images for the films deposited at 200 and 300 W are shown in the Figure 5.4. Films deposited at 200 W show fine grained surface but films grown at 300 W show relatively rough surface. SEM image in Figure 5.5(b) show nanograins on the surface of the films. EDX spectrum clearly indicates the presence of Al in the films.

5.3.2 Optical transmittance and Electrical properties

Figure 5.6 shows the optical transmittance spectrum of the AZO thin films deposited with different sputter powers in the wavelength range 330-850 nm. The optical absorption edge shift was observed. This shift in the absorption may be due to variation of Al content in the films. All the films show an average transmittance above 80% in the wavelength region from 380 to 800 nm. If the thickness of the film is uniform, interference effects give rise to a spectrum as shown in Figure 5.6. These fringes can be used to calculate the optical constants of the film. By using these optical constants we can also calculate the thickness of the film. We adopted method proposed by Swanepoel

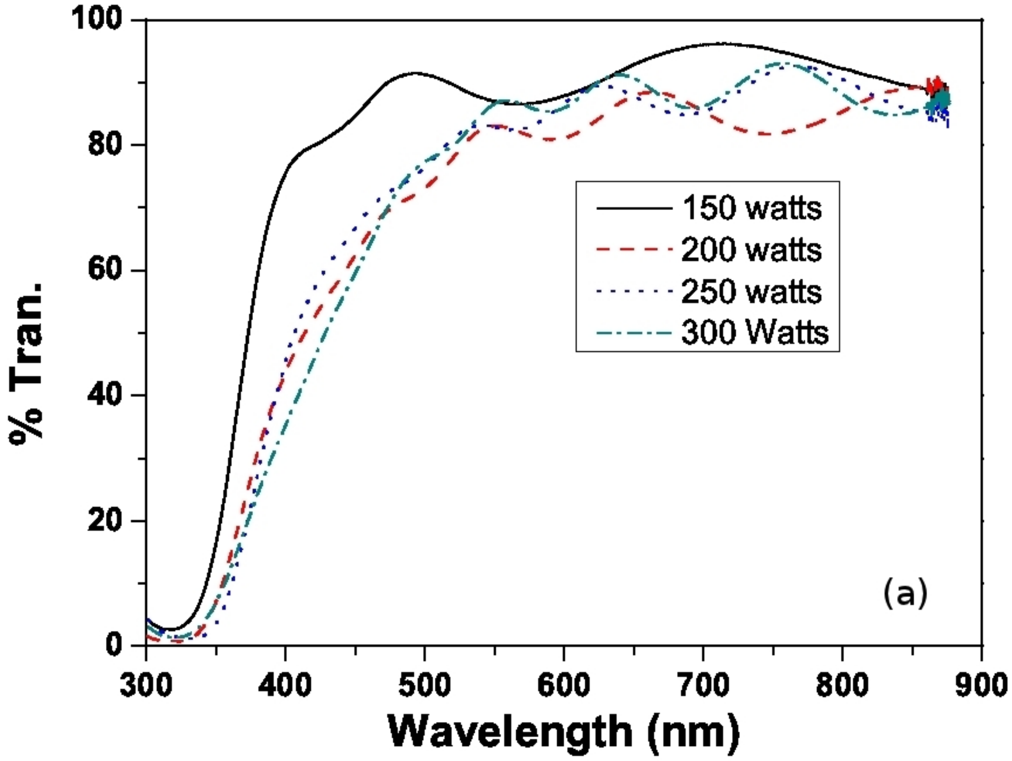

Figure 5.6: Optical transmittance spectra for AZO thin films.

which is known as Swanepoel's envelop method (Swanepoel 1983). Envelop curves were formed by fitting curves obtained for T$_{max}$ and T$_{min}$ of the interference pattern in the weak absorption medium of the transmission spectra (Figure 5.7). Thickness of the films was calculated from the equation (Swanepoel 1983).

$$d = \frac{M\lambda_1\lambda_2}{2[n(\lambda_1)\lambda_2 - n(\lambda_2)\lambda_1]} \tag{5.4}$$

Where, M is the number of oscillations between the two maxima or minima λ_1, λ_2 and n(λ_1), n(λ_2) are the corresponding indices of refraction. Refractive index n is calculated by equations

$$n = [N + (N^2 - {n_s}^2)^{\frac{1}{2}}]^{\frac{1}{2}} \tag{5.5}$$

and

$$N = \frac{(n_s + 1)}{2} + 2n_s\frac{(T_{max} - T_{min})}{(T_{max}T_{min})} \tag{5.6}$$

where, n_s is the refractive index of the substrate and T_{max} and T_{min} are the maximum and the minimum transmittances at a same wavelength in the fitted envelop curves on the transmittance spectrum which is shown in Figure 5.7. Thicknesses of the deposited films are tabulated in Table 5.1. Thickness of the films found to increase with the sputter power. The film thickness can also be varied by adjusting the sputter duration. For specific applications the thickness of the films can be maintained constant without much change in Al content by choosing optimum sputter power and duration of deposition. For a direct band gap semiconductor of allowed band-to-band transition, the value of absorption coefficient α is expressed as (Tauc 1974; Mott and Davis 1979)

$$\alpha = \frac{A(h\nu - E_g)^{1/2}}{h\nu} \tag{5.7}$$

where A is a constant, $h\nu$ is the photon energy and E_g is the band gap of the semiconductor. The absorption coefficient can be calculated from the expression $\frac{ln(1/T)}{d}$ where T and d are the transmittance and the thickness of the film respectively. E_g is determined by plotting $(\alpha h\nu)^2$ as a function of $h\nu$, and extrapolating the linear region of $(\alpha h\nu)^2$ to the energy $h\nu$ where $(\alpha h\nu)^2$ corresponds to zero. Figure 5.8 shows the plot of $(\alpha h\nu)^2$ as a function of $h\nu$. Direct optical band gap of pure polycrystalline ZnO film is 3.30 eV (Look et al. 2004). Slightly higher band gap of our ZnO:Al films is attributed to the Burstein-Moss effect caused by an increased free electron concentration due to Al doping (Burstein 1954; Moss 1954). Inset of Figure 5.8 shows the variation of band gap of AZO thin films as a function of Al content in the films. It decreases initially up to 2 at.% Al and then it increases further with Al content. This is due to B-M effect which occurs for highly doped semiconductor.

The resistivity of the films was found to decrease with the sputtering power. This is because, as the sputter power to target increased, the amount of Al content in the films is found to increase. As the power was further increased above 250 W, Al content in the films found to increase beyond 2 at.% hence, the increase in the resistance (Minami 2005). It is well known that, the conduction characteristics of the ZnO are primarily

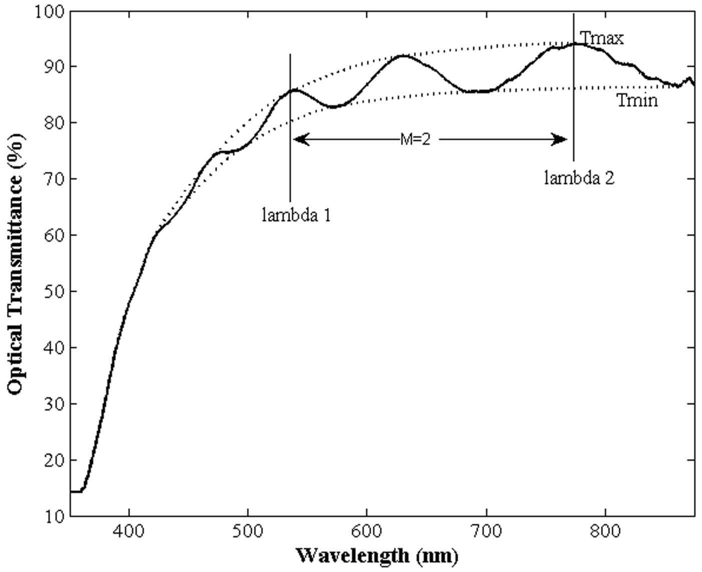

Figure 5.7: Fitted envelope curves drawn for transmission spectra of AZO thin film.

dominated by electrons generated from oxygen vacancies and Zn interstitial atoms. The electrical conductivity in ZnO:Al film is higher than that in pure ZnO films, due to the contribution from Al^{3+} ions on substitutional sites of Zn^{2+} ions (Singh et al. 2004; Kim et al. 2000). As the Al content in the deposited films increases beyond 2 at.%, the doping may lead to the creation of non-conducting Al_2O_3 clusters in the films causing crystal disorder, which act as carrier traps rather than electron donors. The measured resistivity values for AZO films are comparable with the previous reports (Minami 2005, 2012; Sittinger et al. 2006) and it is as low as 0.5×10^{-4} Ω-cm for 2.11 at.% Al doped films which is better compared to the previous report (Santana-Aranda et al. 2007) where the reactive sputtering of Zn and Al coaxial targets was used. The present method offers a technologically simple and economic route to deposit AZO films without the need of two or more magnetrons and targets.

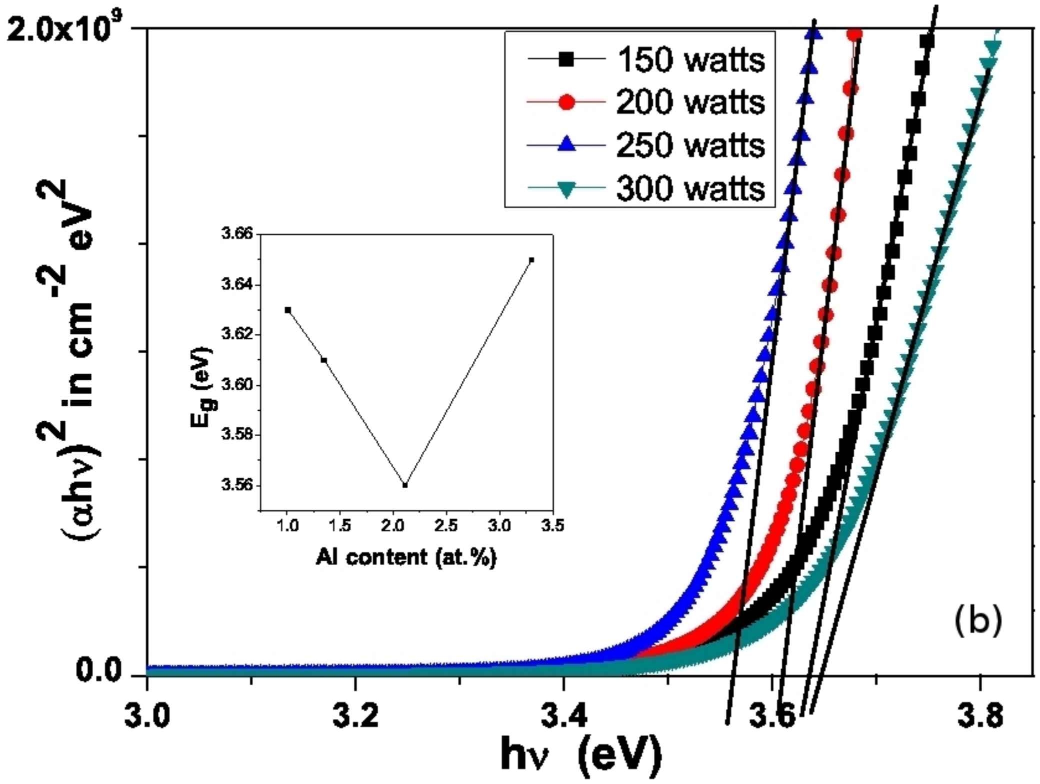

Figure 5.8: $(\alpha h\nu)^2$ vs $h\nu$ plots for AZO thin films, inset shows the variation of band gap with Al content

Table 5.1: Summary of the Al content, energy gap, resistance and the lattice parameter of the studied samples

Sputter power (W)	Film thickness (nm)	Al content $(at.\%.)$	Energy bandgap (eV)	Electrical resistivity $(\times 10^{-4}\Omega - cm)$	c (nm)
150	477	1.01	3.63	10.0	0.5286
200	932	1.35	3.61	8.0	0.5245
250	1160	2.11	3.56	0.5	0.5237
300	1320	3.45	3.65	10.8	0.5254

5.4 Properties of ZnO/Al/ZnO multilayers by simultaneous RF and DC magnetron sputtering

5.4.1 X-ray diffraction studies

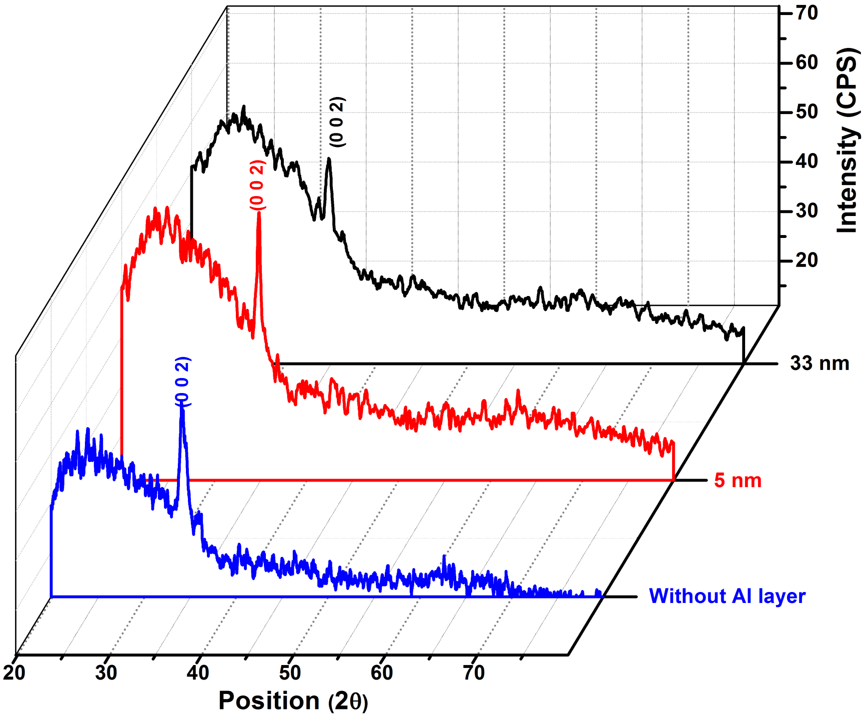

Figure 5.9: XRD of ZnO and multilayers with different Al interlayer thickness.

X-ray diffraction patterns of the deposited multilayers are shown in Figure 5.9. The thickness of the ZnO layer was found around 100 nm and Al layer thickness varies from 5 nm to 30 nm. Thickness of Al layer was calculated by considering the deposition rate of Al. A single peak at $2\theta \approx 34.75°$confirms the existence of ZnO phase. It is also revealed that the deposited films show preferred orientation along (0 0 2) planes. Intensity of (0 0 2) peak found to decrease with the increase in Al layer thickness which indicates the decrease in the crystallanity. No prominent peaks corresponding to Al were observed. This may be because of the fact that the thickness of the ZnO layer is large compared to that of Al. Observed 2θ positions for multilayer film was bit high compared to that of ZnO film studied here. This is because of residual stresses

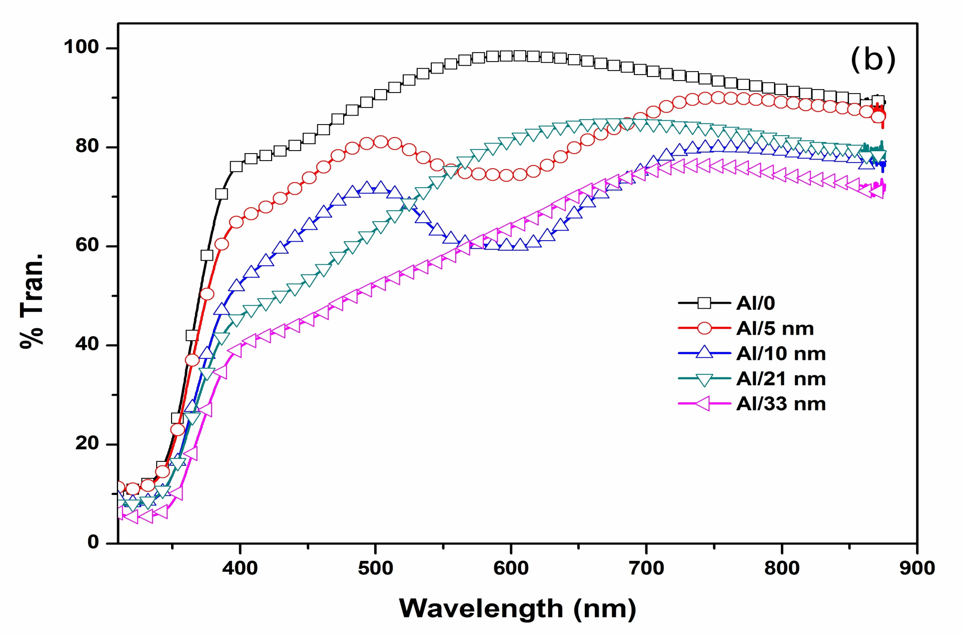

Figure 5.10: Transmittance spectra of ZnO and multilayer thin films.

present in the films during deposition. Undoped film show a compressive stress where as multilayer shows tensile stress. This may because of the presence of Al interlayer.

5.4.2 Optical transmittance and electrical resistance

Optical transmittance spectra of the deposited films are shown in Figure 5.10. For undoped films a good transmittance over 80% was observed in the visible region of the electromagnetic spectra. The average transmittance of the films in the visible region decreases as the Al layer thickness increases. The absorption edge of the multilayer films shifts towards higher wavelength with increase in the thickness of Al interlayer thickness. As the thickness of Al interlayer increases the electrical resistance decreases (Figure 5.11). The multilayered thin films show low resistance because of Al interlayer. The conduction electrons were supplied from donor sites associated with excess Zinc, and Aluminum ions on substitutional sites of Zinc ions in the as deposited samples. The lowest resistance is obtained for the multilayer thin film with Al interlayer thickness 33 nm.

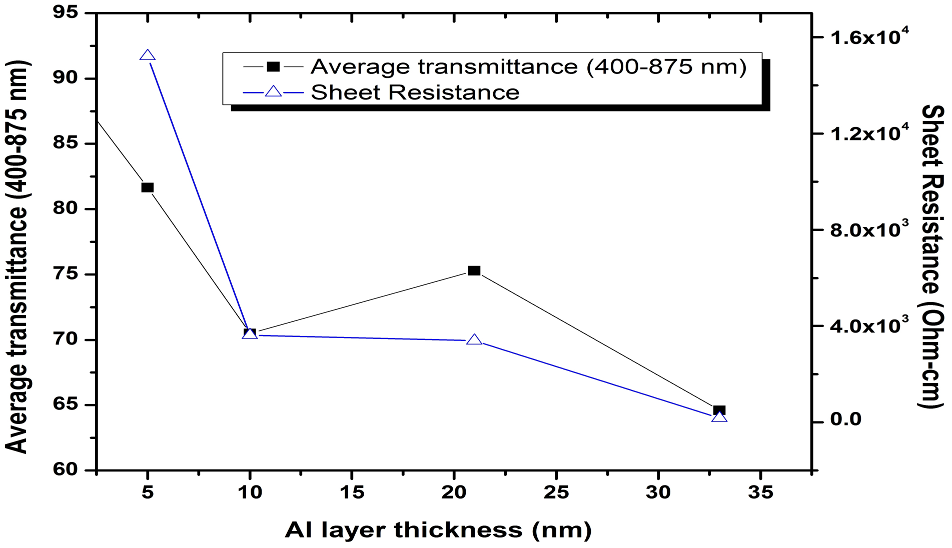

Figure 5.11: The variation of sheet resistance and average transmittance (400-875nm) with Al interlayer thickness.

5.5 Conclusions

In conclusion, we have successfully deposited Al doped ZnO thin films using coaxial targets. Al content in the deposited films found to vary with the sputtering power, which can be used to control the resistivity of the films. The lowest resistivity obtained was $0.5 \times 10^{-4}\Omega$-cm for the film deposited at 250 W. The variation in stress values in the films showed a considerable change with Al content in the films, which is due to the presence of Al^{3+} ions in the ZnO matrix. Optical band gap of the films was estimated using absorption spectra which vary with the Al content in films.

Multilayers of ZnO/Al/ZnO were deposited by simultaneous RF and DC sputtering. Obtained multilayers were characterized using optical transmittance spectra and XRD. Sheet resistance of the multilayers found to decrease with the increase in the Al interlayer thickness. XRD patterns of the multilayers show reflections corresponding to Wurtzite ZnO, no peaks corresponding to Al observed due to thicker ZnO layers. Transmittance spectra shows a considerable decrease in the average transmittance (in the visible region) of the multilayers.

Chapter 6

Growth and properties of Manganese (Mn) doped ZnO thin films

This Chapter presents the preparation of manganese doped zinc oxide thin films and the effect of Mn concentration on the structural and optical properties of ZnO thin films.

6.1 Introduction

Doped ZnO thin films are studied widely for many practical applications like spintronics devices, light emitting diodes, diode lasers etc. (Pearton et al. 2003; Chu et al. 2008; Lupan et al. 2011; Ip et al. 2003). The ZnO based diluted magnetic semiconductors (DMS) have been studied widely in the recent years. The DMS materials, combining charge with spin degrees of freedom, are the potential candidates for many spintronics applications such as spin-valve transistors, spin LEDs, spin polarized lasers, non-volatile memory and magneto optical switches (Pearton et al. 2008). The developments started with the theoretical prediction of room temperature ferromagnetism in Mn doped ZnO by Dietl et al (Dietl et al. 2000). In particular, incorporation of Mn ions in to the large band gap ZnO lattice promises to lead to a new magnetic transport and optical properties. The half filled 3d-shell of Mn^{2+} ions, which have the largest ionic moment ($5\mu_b$), plays a important role in both theoretical and experimental studies of ZnO (Chikoidze et al. 2007). Ferromagnetism near and above the room temperatures has been reported for Mn doped ZnO pellets, powders and thin films (Sharma et al. 2003), whereas some studies reported only paramagnetism (Risbud et al. 2003). Since Mn is paramagnetic, any ferromagnetism detected in Mn doped ZnO cannot be due to the Mn or Mn oxide precipitates those may be formed during the preparation process. Despite to close analogy to Mn doped ZnS, which is an efficient phosphor, it has been shown that the luminescence in Mn doped ZnO suppressed to the large extent even at low doping concentration. Therefore Mn has been considered to be a quencher of luminescence in ZnO and predominantly optical absorption and transmission experiments have been performed on Mn doped ZnO (Chikoidze et al. 2007). However, a little is known about the nonlinear optical properties of ZnO thin films (Abed et al. 2011).

The second and third-order nonlinear optical properties of undoped ZnO thin films (Larciprete et al. 2006) and ZnO thin films doped with Ni, Zr, Ce, F, Er, Al, Sn, F:In (Abed et al. 2011; Bahedi et al. 2009; Sofiani et al. 2006, 2007; Lamrani et al. 2007; M.-Saavedra and Castaneda 2007) deposited using various techniques under pulsed lasers have been reported. The study of photo physical and optical characteristics such as nonlinearity, magnitude, response time, etc., must be carried out to spot the material suitability for nonlinear applications (Gayathri and Ramalingam 2008). The magnetic, optical and electrical properties of Manganese (Mn) doped ZnO thin films (Kim and Park 2003; Chikoidze et al. 2007; Jung et al. 2002) have been studied. These results reveal that Mn doped ZnO films have good optical properties. To the best of our knowledge, the nonlinear optical properties of ZnO thin films doped with manganese (Mn) have not been investigated. Hence, it is necessary to investigate and study the nonlinear optical properties of Mn doped ZnO thin films for its future applications. The nonlinear optical response of thin films is of particular interest because of its application in integrated nonlinear optical devices (Abed et al. 2011).

Continuous wave (cw) lasers ranging from μW to kW are widely used in various applications (Gayathri and Ramalingam 2008) such as, laser printers, optical discs, barcode scanners, thermometers, laser pointers, holograms, CD-ROM/DVD drives and players, CD/DVD burners, micro machining, non-contact measurement, laser cutting, medical surgeries, cosmetic skin treatments forensics, military (weapon) applications, entertainment etc (Thyagarajan and Ghatak 2011). This necessitates the need for protecting the optical sensors from high intense laser beams. In this chapter, we report for first time the third-order optical nonlinearity and optical power limiting properties of Mn doped ZnO sputtered thin films under cw laser using z-scan technique. Under cw laser illuminations, the self focusing and self defocussing effects are usually associated with refractive nonlinearities of thermo-optic origin (Sreekumar et al. 2007).

6.2 Experimental

6.2.1 Deposition of Mn doped ZnO thin films

Mn doped ZnO thin films were deposited on glass substrates by radio frequency (RF) magnetron sputtering. The compound targets with various Mn concentration (0, 5, 10 and 15 wt.%) were prepared using solid state reaction technique in which ZnO (99.99%, from Sigma) and MnO_2 (99.99%, from Sigma) were mixed thoroughly in a planetary ball mill for ten hours. This homogeneous mixture was calcinated at 400 °C for 6 hours. The calcinated powders were cold pressed using hydraulic press at a pressure of 25 MPa to get 50 mm diameter pellets. The pressed pellets were sintered at 950 °C for 6 hours to get dense pellets. These pellets were used as targets and they are mounted on the water magnetron cooled cathode. The targets with different Mn concentration were sputtered to get thin films on precleaned glass substrates. Before each sputter process the chamber was pumped down to a pressure less than 5×10^{-6} mbar. The sputtering was performed in the growth ambient with mixture of high purity Ar (99.999%) and O_2 (99.8%) at a constant working pressure of 0.02 mbar. The Oxygen to argon ratio was adjusted to 3 and kept constant for all our experiments. Before each sputtering process, the targets were pre-sputtered in pure Ar for 30 minutes to remove any contamination on the target surface and to make the system stable. The RF power, sputter duration and the target to substrates distance were kept constant at 200 W, 60 min and 50 mm respectively in all experiments.

The thickness of deposited film is measured by using Filmetrics film thickness measurement system (Model-F 20) and found to be 125±20 nm for Mn doped ZnO films and it is 350±20 nm for undoped ZnO film. Topography of the deposited films was characterized commercially available AFM system (Veeco, Innova) in contact mode. Nanoscope software was used to examine the three dimensional features on AFM image. The linear refractive index was measured using spectroscopic ellipsometry. The optical transmittance measurements were done using Ocean Optics USB4000 UV-VIS spectrophotometer in the spectral range 300-800 nm.

6.2.2 Z-scan and optical limiting

The nonlinear index of refraction n_2, the nonlinear absorption coefficient β_{eff}, the magnitude of the real and imaginary parts of third-order nonlinear susceptibility $\chi^{(3)}$ of Mn doped and undoped ZnO thin films was characterized using z-scan technique developed by Mansoor Sheik Bahae et al. (Sheik-Bahae et al. 1989, 1990). In this technique, a polarized Gaussian laser beam is focused to a narrow waist. The samples were mounted on a translation stage and moved along z-direction through the beam focus (z=0), self-focusing or self-defocussing modifies the wave front phase, there by modifying the detected beam intensity. The schematic experimental setup used for z- scan technique is shown in Figure 1. The optical power limiting responses of the films was studied by placing the samples at the focus. The input power of the laser beam was varied by using neutral density filter and the resultant output power through the samples was recorded using a photo-detector fed to the power meter.

For the present studies a CW He-Ne laser at 633 nm wavelength was used as excitation source. The laser beam with power input 21.8 mW was focused using a 5 cm focal length lens. The measured laser beam waist ω_0 and the Rayleigh length Z_R are 36.78 μm and 6.71 mm respectively.

6.3 Structure and surface morphology

6.3.1 X-ray diffraction studies

During the sintering process of the compound targets, the Mn ions substitute to Zn in ZnO which leads to formation of $Zn_{(1-x)}Mn_xO$. The milling process performed to mix ZnO and MnO_2 creates new surfaces that can favor the initial reduction of manganese sites. Also, it is known that the MnO_2 gets converted into Mn_2O_3 at 536 °C, which then transforms to Mn_3O_4 at 767 °C, and finally gets converted to MnO above 1080 °C (Bhatti et al. 2005). Figure 6.1 shows XRD patterns of undoped and Mn doped ZnO thin films. Undoped thin films show a preferred orientation along c-axis which is confirmed by the presence of a strong peak along (0 0 2) planes at 2θ value 34.337°. The value is slightly less than the actual value 34.44°, which is due to the presence of residual stresses in the films. Preferred orientation disappears for doped films as indicated by XRD patterns of doped films. These films show additional peaks at

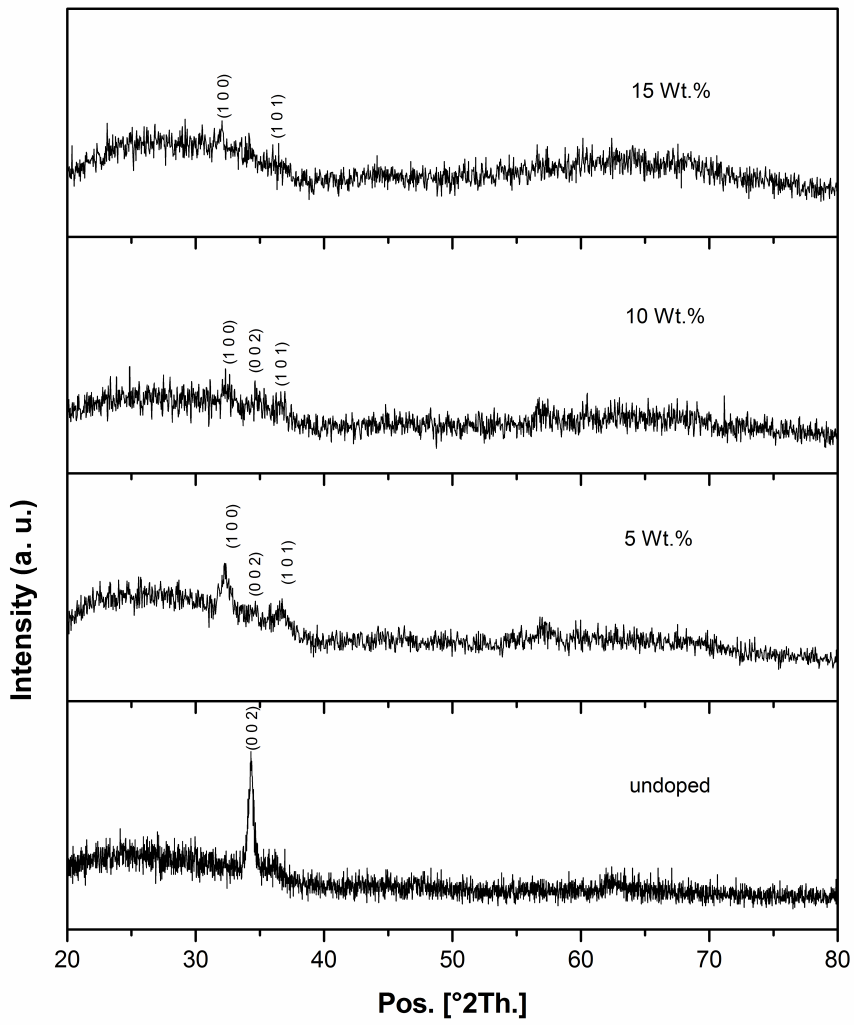

Figure 6.1: XRD patterns of undoped and Mn doped ZnO thin films

32.286° and 36.711° corresponding to (1 0 0) and (1 0 1) planes respectively (JCPDS: 01-089-0511). The peak positions shift to higher angles as the dopant concentration increases because of the decrease in their interplanar spacing d due to substitution of lattice site by an ion of lower radius (Karamat et al. 2008). The lattice parameter c calculated to be 0.5219 nm, 0.5163 nm and 0.5134 nm for undoped, 5 wt.% Mn doped and 10 wt.% Mn doped ZnO films. We could not find lattice parameter c for 15 wt.% Mn doped films as the (0 0 2) peak was out of detection range of X-ray diffractometer. The lattice parameter a for 5, 10 and 15 wt.% Mn doped films was calculated as 0.3201 nm, 0.3180 nm and 0.3085 nm respectively. The ionic radius of Zn^{2+} (~0.60 Å) is large compared to that of Mn^{4+} (~0.53 Å) and Mn^{3+} (~0.58 Å) ion but it is smaller than Mn^{2+} (~0.67 Å) ions (Bhatti et al. 2005). When an ion with smaller ionic radius substitutes the host ion there will be a decrease in the lattice parameters a and c (Bhatti et al. 2005). Thus the observed decrease in the present study is due to substitution of Zn^{2+} ions by Mn^{4+} and Mn^{3+} ions. It is also observed that the intensity of the peaks start to diminish rapidly as the doping concentration increases. According to Han et al. Mn doping in the range 0.1-1.2 mol% promoted the grain growth of ZnO during sintering (2000). But, Excessive doping usually resulted in segregation of second phase in grain boundaries, thereby hindering the grain growth and it deteriorates the crystal structure (Rahaman 1995). Therefore, the deterioration of crystal structure in our samples can be attributed to excess doping of Mn.

6.3.2 Studies on Surface morphology using AFM

AFM images were collected to examine the surface properties of ZnO and Mn doped ZnO thin films. Figure 6.2 shows 2-D topographic images of undoped ZnO and Mn (5, 10 & 15 wt.%) doped ZnO thin films. The morphology of ZnO thin film consisted of big columnar grains with variation in their diameters. As the doping percentage of Mn increases, the films show lack of crystallanity which is clear from 2-D images for 10 wt.% and 15 wt.% Mn doped films. Lack of crystallanity in Mn doped thin films was also observed by Kim et al. (Kim et al. 2004).

Roughness values of the deposited films were calculated using Nanoscope soft-

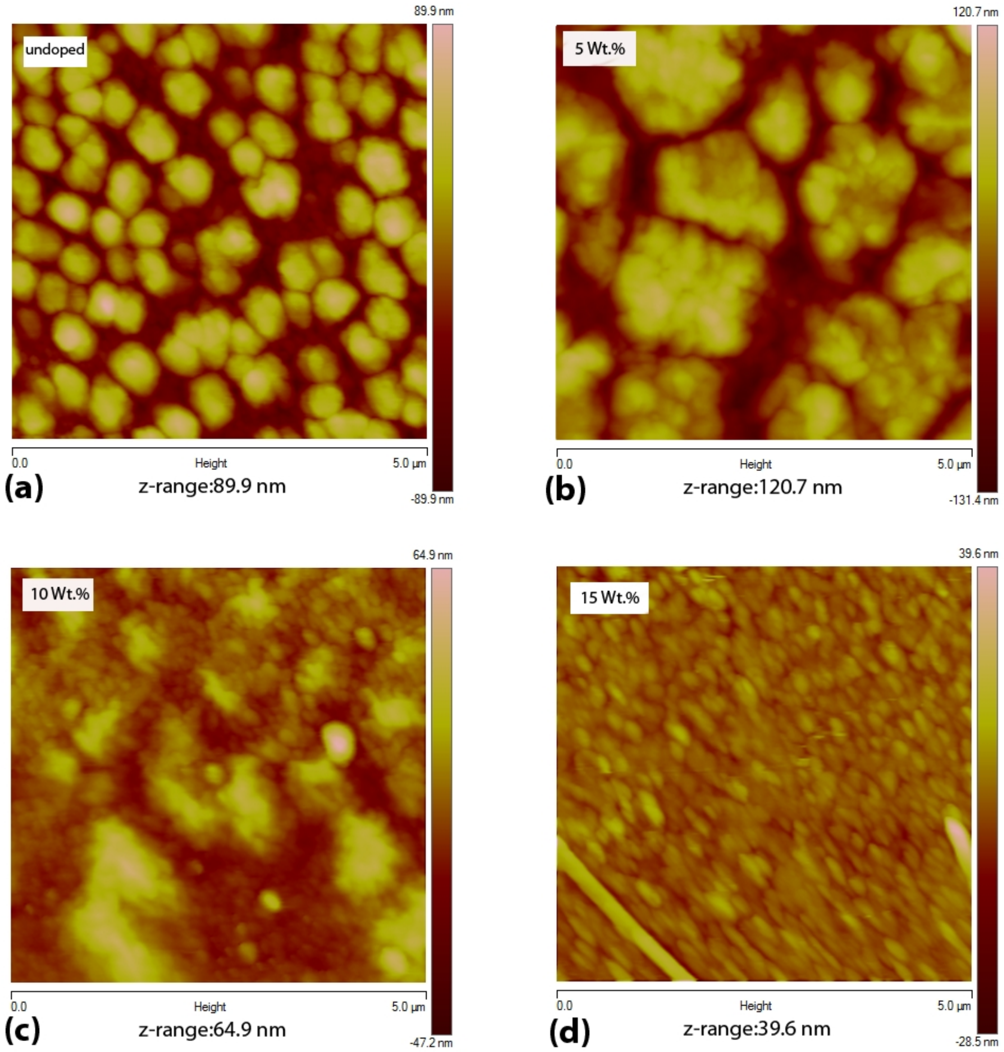

Figure 6.2: 2-D AFM images of (a) Undoped (b) 5 wt.% Mn doped (c) 10 wt.% Mn doped & (d) 15 wt.% Mn doped ZnO thin films.

ware. The roughness value of doped film is greater than that of undoped one and found to decrease as the doping concentration increases even lesser than that of undoped films. Interstitial Zn plays an important role in the grain growth process. Due to substitution of Mn ions, interstitial Zn will be decreased. So the grain growth was inhibited because of the decreased diffusivity which in turn decreases the grain size (Fujihara et al. 2001). As the grain size becomes smaller the roughness decreases further. The average roughness values are tabulated in Table 6.1.

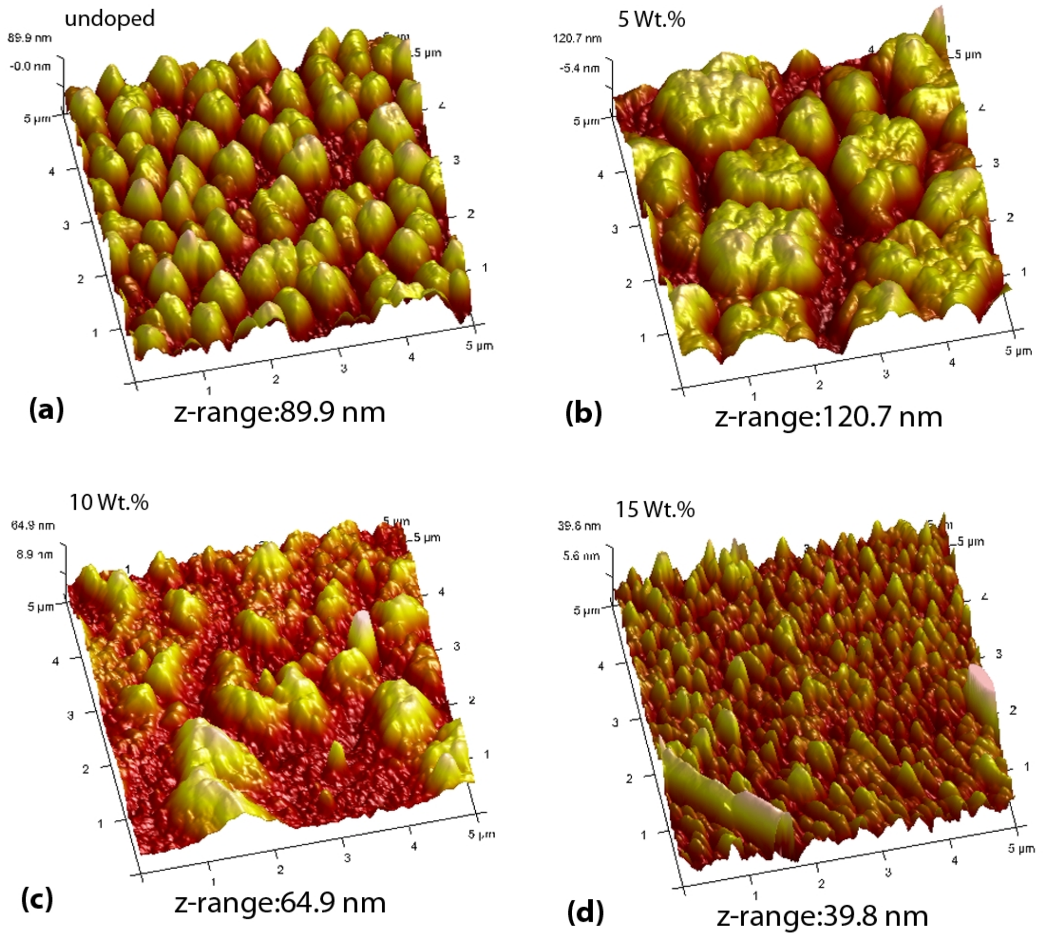

Figure 6.3: 3-D AFM images of (a) Undoped (b) 5 wt.% Mn doped (c) 10 wt.% Mn doped & (d) 15 wt.% Mn doped ZnO thin films.

6.4 Optical properties of Mn doped ZnO thin films

6.4.1 UV-VIS Spectra and Band gap analysis

Figure 6.4 show the UV-VIS transmittance spectra and Tauc plots of undoped and Mn doped ZnO thin films. All the films show very high transmittance (upto 90%) in the UV and visible regions. In case of undoped ZnO, the sharp fall of the transmittance near the absorption edge ~370 nm indicates their high crystalline and direct band gap nature. The same spectra also reveal that with the increase in the Mn doping concentration, the absorption edge shifts to lower wavelengths. The doped films are transparent but have a slight brown color. The color becomes deeper as the Mn concentration in the films increases. The average transmittance of undoped ZnO film is 91% in the 400-800 nm range. On the other hand, the average transmittance of Mn doped ZnO films for 5, 10 and 15 Wt.% are 76%, 75% and 70% respectively.

Table 6.1: Average transmittance, energy band gap and roughness values of Mn doped and undoped ZnO thin films

Sample No.	Mn Concentration (wt.%)	Average Transmittance (400-800 nm)(%)	Energy bandgap (eV)	Average Roughness (nm)
1	undoped	91	3.20	26.7
2	5	76	3.27	35.3
3	10	75	3.29	13.9
4	15	70	3.34	6.4

The optical band gap of the films was found using the relation (Tauc 1974; Mott and Davis 1979).

$$\alpha = \frac{A(h\nu - E_g)^{1/2}}{h\nu} \tag{6.1}$$

The band gap of the undoped films is found to be 3.2 eV. The band gap found to increase with Mn concentration in the films. The increase of band gap from bulk ZnO with Mn concentration in the deposited films can be attributed to the sp-d spin-exchange interaction between the band electrons and localized spin of the transition-metal ions (Mandal and Nath 2006). The main d-d transitions occur at $^6A_1 \rightarrow ^4T_1, ^4T_2, ^4A_1, ^4E$ energy levels of Mn^{+2} ion in presence of tetrahedral crystal field interaction similar to the results observed by other groups (Koidl 1977; Koidl et al. 1973; Kim and Park 2003; Jung et al. 2002). Average transmittance values in the wavelength range 400-800 nm and the estimated band gap values for Mn doped and undoped ZnO films are given in Table 6.1.

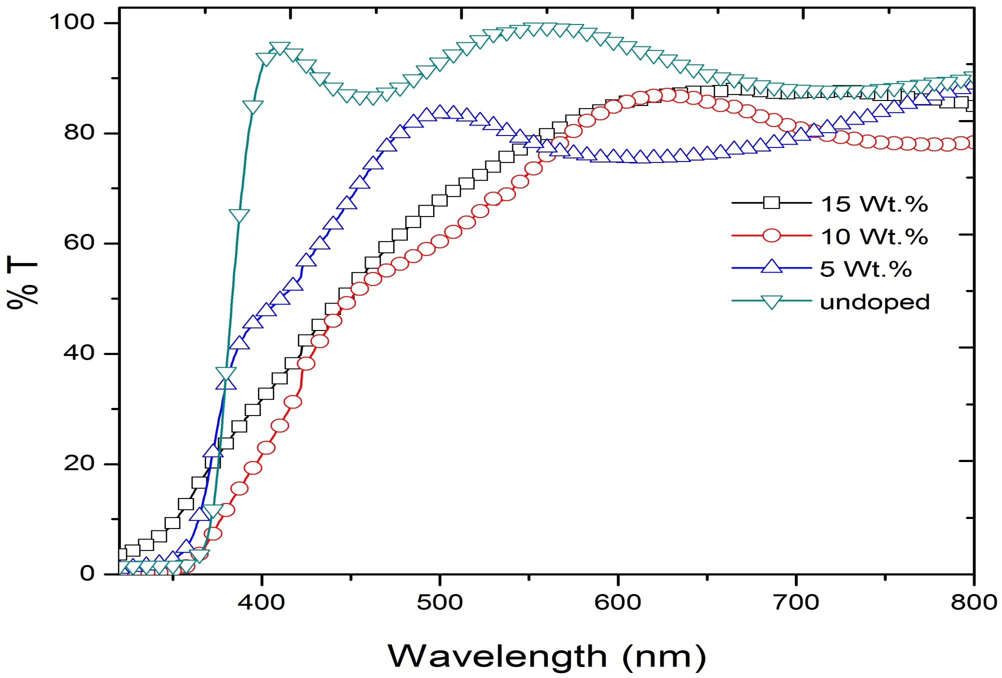

Figure 6.4: Transmittance spectra of Mn doped and undoped ZnO thin films

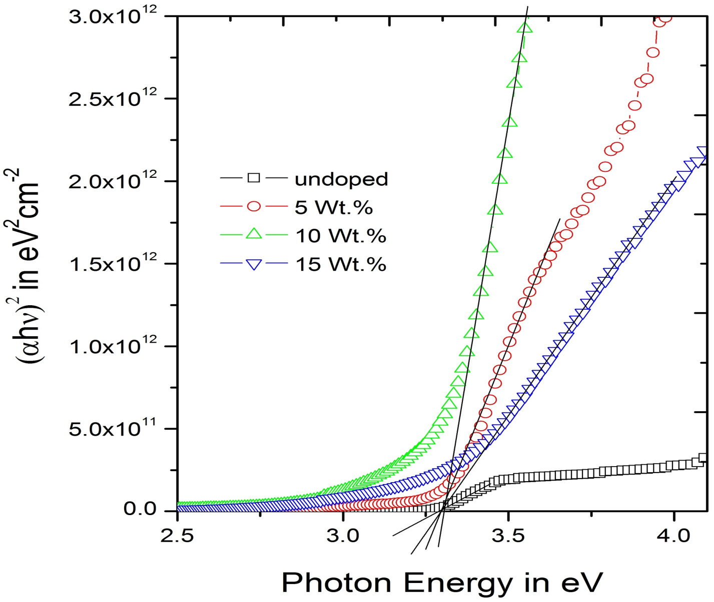

Figure 6.5: Tauc plots of Mn doped and undoped ZnO thin films.

6.4.2 Nonlinear optical properties

6.4.2.1 Nonlinear absorption and refraction

In order to determine the sign and magnitude of real and imaginary parts of third-order nonlinear susceptibility z-scan studies were conducted. The intensity dependent nonlinear absorption and refraction are expressed by the equations (Sheik-Bahae et al. 1989, 1990; Boyd 2008),

$$\alpha(I) = \alpha + \beta_{eff} I \tag{6.2}$$

$$n(I) = n_0 + n_2 I \tag{6.3}$$

where α is the linear absorption coefficient, n_0 is the linear refractive index, β_{eff} the nonlinear absorption coefficient, n_2 is the nonlinear refractive index and I the intensity of the laser beam. The nonlinear absorption coefficient β_{eff} of the Mn doped and undoped ZnO films were determined from the open aperture z-scan measurements. The results obtained for open aperture z-scan measurements of the film that corresponds to the far field normalized transmittance T(z) as a function of the distance from the beam focus are shown in Figure 6.6. The open aperture curve exhibits the presence of induced absorption in the films, as the transmission at the focus decreases with increase in intensity. The nonlinearity obtained is of third-order, as it fits to a two-photon absorption process. Better nonlinear optical properties are observed with increase in concentration. However, the THG comprised with SHG and SFG in polycrystalline films has very low efficiency, which is even lower for thin films and therefore neglected (Morkoc and Ozgur 2009).

There are several mechanisms reported to occur in nanomaterials that give rise to nonlinear absorption including two-photon absorption (TPA), reverse saturable absorption (RSA), transient absorption, free carrier absorption (FCA) and nonlinear scattering (Kumari et al. 2012). In semiconductors, two-photon absorption is allowed, when the incident light source energy is less than the direct band gap energy E_g, but greater than $E_g/2$ (Morkoc and Ozgur 2009). In the present case, as the photon energies are smaller than the band gap, the nonlinear response is due to the third-order nonlinearity

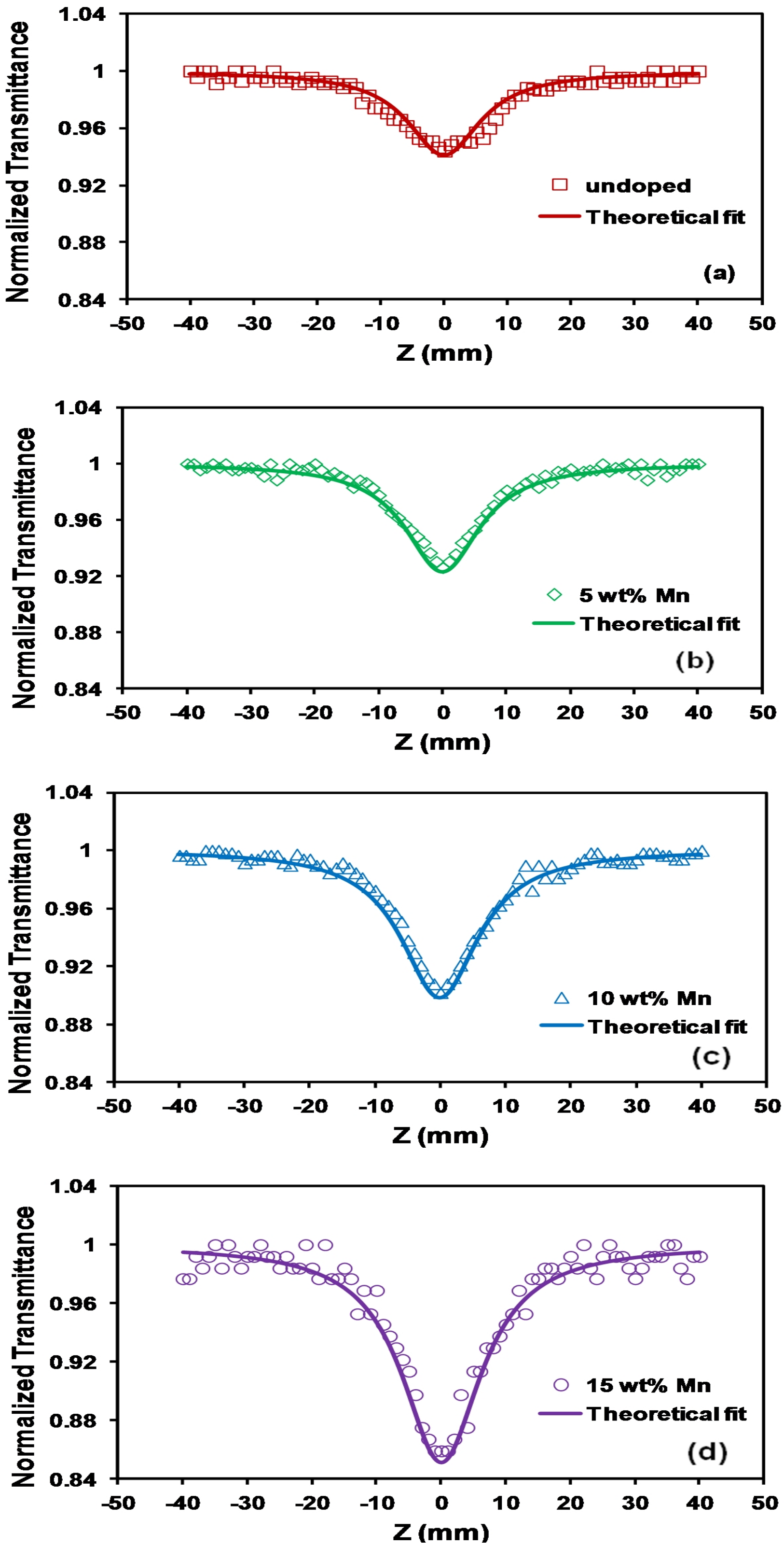

Figure 6.6: Open aperture z-scan traces of (a) Undoped (b) 5 wt.% Mn (c) 10 wt.% Mn & (d) 15 wt.% Mn doped ZnO thin films. Solid line depicts theoretical fit.

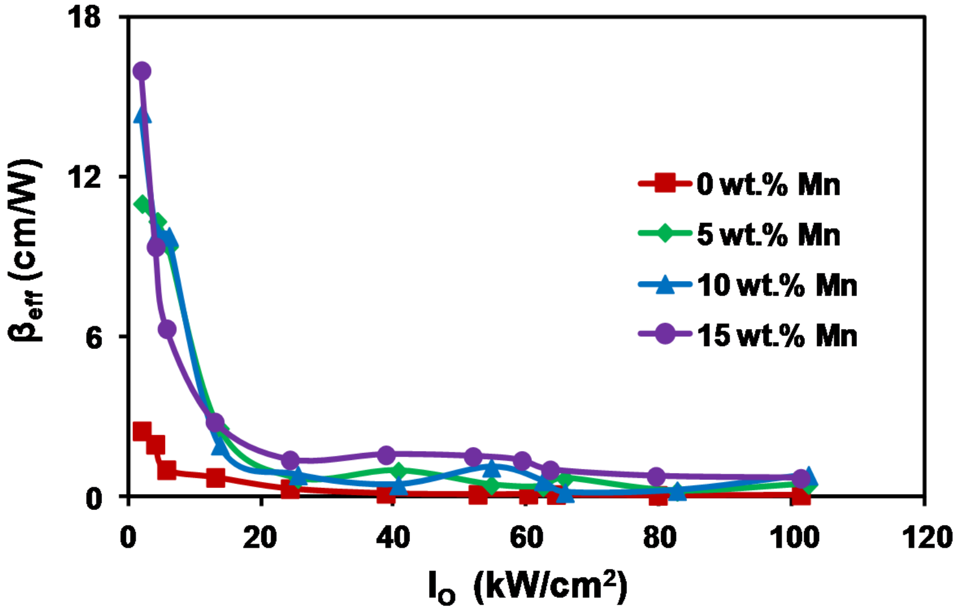

Figure 6.7: The nonlinear absorption coefficient β_{eff} v/s on-axis input intensity I_0 of (a) Undoped (b) 5 wt.% Mn (c) 10 wt.% Mn & (d) 15 wt.% Mn doped ZnO thin films.

arising from the bound electronic effects and the two-photon absorption (Morkoc and Ozgur 2009). Along with TPA free carrier absorption, a higher order nonlinear process may also contribute to induced absorption. Compared to TPA, FCA is a weak process and hence its contribution to the nonlinear absorption is relatively less (Irimpan et al. 2008a). Further, if the nonlinearity is due to two-photon absorption alone, the nonlinear absorption coefficient β_{eff} obtained using eqn.6.2 should be a constant independent of on-axis input intensity I_0. But from the Figure 6.7, the β_{eff} values decreases with increase in on-axis input intensity I_0 for the MZO films, which is the consequence of sequential two-photon absorption. It has been reported that the nonlinear absorption in ZnSe, ZnO and ZnS is due to two-photon induced FCA along with TPA (Zhang et al. 1997). The enhancement of nonlinear absorption of MZO films compared to undoped films may be due to the free carrier absorption originated from the Mn ions of ZnO matrices. Thus, we can infer that the nonlinearity observed in thin films is due to TPA followed by weak FCA. Under open aperture z-scan condition, normalized transmission is given by (Sheik-Bahae et al. 1989, 1990),

$$T(z, S=1) = \sum_{m=0}^{\infty} \frac{[-q_0(z,0)]^m}{(m+1)^{\frac{3}{2}}} \tag{6.4}$$

where q_0 is a free factor defined as, $q_0(z) = \frac{\beta_{eff} I_0 L_{eff}}{(1+z^2/z_R^2)}$
L_{eff} is the effective thickness of the sample, which is defined as, $L_{eff} = \frac{(1-e^{\alpha L})}{\alpha}$,
I_0 is the intensity of the laser beam at the focus and,
L is the thickness.

A fit to the equation 6.2 to the open aperture data yielded a large value of nonlinear absorption coefficient β_{eff} for the films. Closed aperture z-scan experiments with aperture were performed to study the nonlinear refraction behavior of the Mn doped and undoped ZnO films. Figure 6.8 illustrates the closed aperture z-scan profiles of all Mn-ZnO films. The closed aperture z-scan curves exhibit a pre-focal transmittance maximum (peak) followed by a post-focal transmittance minimum (valley) signature for all the films. This peak-valley signature indicates the self defocussing property, which corresponds to negative nonlinear refractive index n_2 (Sheik-Bahae et al. 1989, 1990). The sign of the nonlinear index of refraction n_2 of a sample is thus immediately clear from the shape of graph. The sensitivity to nonlinear refraction is entirely due to aperture, and absence of aperture completely eliminates the effect (Sheik-Bahae et al. 1989, 1990). It is important to note that in most of the cases nonlinear refraction does not occur on its own, but usually in conjunction with nonlinear absorption. This implies that the closed aperture data obtained from z-scan will contain both nonlinear refraction and nonlinear absorption components. By dividing the closed aperture z-scan trace by the open aperture z-scan trace, one can extract pure nonlinear refraction. The physical origin of nonlinear refraction can be electronic, molecular, electrostrictive or thermal in nature. In the present case, the nonlinearity is thermal in nature as CW laser is used (Christodoulides et al. 2010). The closed aperture z-scan curves for all films show a peak-valley separation of $2Z_R$. A peak-valley separation of more than 1.7 times the Rayleigh range (Z_R) is the clear indication of thermal nonlinearity. The nonlinear refractive index γ(m^2/W) is given by the formula (Sheik-Bahae et al. 1989, 1990),

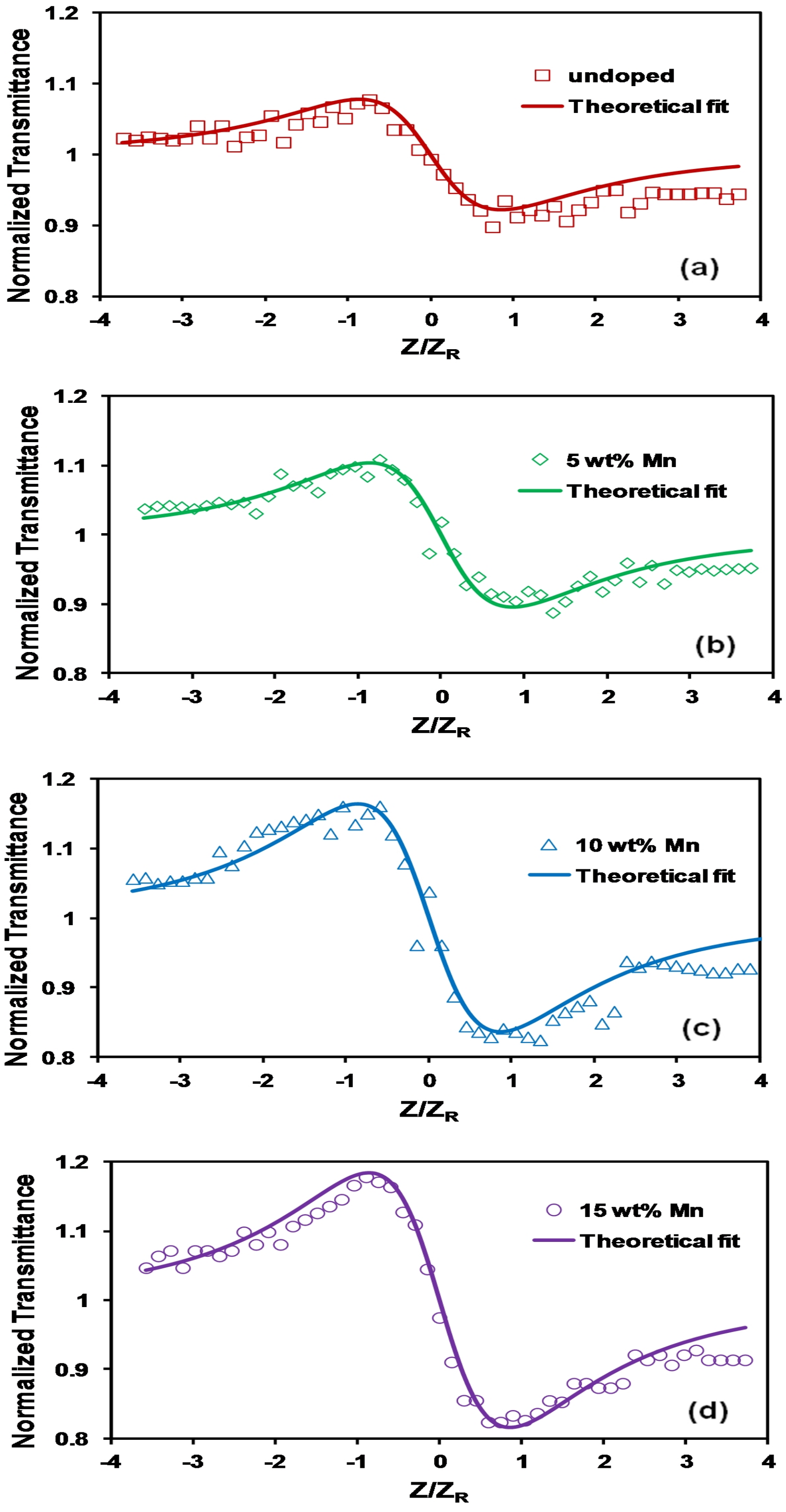

Figure 6.8: Closed aperture z-scan traces of (a) Undoped ZnO (b) 5 wt.% Mn (c) 10 wt.% Mn & (d) 15 wt.% Mn doped ZnO thin films. Solid line depicts theoretical fit.

$$\gamma = \frac{\Delta\ \Phi_0 \lambda}{2\pi L_{eff} I_0}(m^2/W) \tag{6.5}$$

where $\Delta\Phi_0$ is the on-axis phase shift given by the equation (Sheik-Bahae et al. 1989, 1990),

$$\Delta\ \Phi_0 = \frac{\Delta\ T_{p-\nu}}{0.406(1-S)^{0.25}} for|\Delta\ \Phi_0| \leq \pi \tag{6.6}$$

where $\Delta T_{p-\nu}$ is the difference in peak-valley normalized transmittance and S is the linear aperture transmittance, which is equal to 0.7 in our experiments. The normalized transmittance for pure nonlinear refraction is given by (Sheik-Bahae et al. 1989, 1990),

$$T(z) = 1 + \frac{4x\Delta\Phi_0}{(x^2+9)(x^2+1)} \tag{6.7}$$

where $x = z/z_R, z_R = \pi\omega^2/\lambda$, is the Rayleigh length of the laser beam and ω_0 is the laser beam waist at the focal point. The nonlinear refractive index n_2 and nonlinear absorption coefficient β_{eff}, are related to the real and imaginary part of third-order nonlinear optical susceptibility $\chi^{(3)}$ through the equation,

$$\chi_R^{(3)}(esu) = 10^{-4}\frac{\varepsilon_0 c^2 n_0^2}{\pi} n_2(cm^2/W) \tag{6.8}$$

and

$$\chi_I^{(3)}(esu) = 10^{-2}\frac{\varepsilon_0 c^2 n_0^2 \lambda}{4\pi^2} \beta_{eff}(cm/W) \tag{6.9}$$

where ε_0 is the vacuum permittivity and c is the light velocity in vacuum. We conducted z-scan experiment on the plane glass slides used and found negligible contribution both for nonlinear refraction and nonlinear absorption at the input intensity used. Therefore at the input intensity used, any contribution from the plane glass slide to the observed nonlinearity is negligible. Using the obtained values of n_2 and β_{eff}, the real and imaginary parts of the third-order nonlinear susceptibility was determined. The obtained

Table 6.2: β_{eff}, n_2, $\chi_R^{(3)}$,$\chi_I^{(3)}$ and $\chi^{(3)}$ of Mn doped and undoped ZnO thin films.

Dopant concentration (wt.%)	Nonlinear absorption coefficient β_{eff} (cm/W)	Nonlinear refraction coefficient n_2 (cm^2/W) $\times 10^{-4}$	Real $\chi_R^{(3)}$ (esu) $\times 10^{-3}$	Imaginary $\chi_I^{(3)}$ (esu) $\times 10^{-4}$	$\lvert\chi^{(3)}\rvert$ (esu) $\times 10^{-3}$
undoped	0.371	-0.139	-0.10	0.14	0.10
5	3.23	-0.319	-0.32	1.63	0.36
10	3.73	-1.51	-1.62	2.02	1.63
15	5.26	-1.56	-1.95	3.33	1.98

values of nonlinear refractive index n$_2$, nonlinear absorption coefficient β_{eff} and the real and imaginary parts of the third-order nonlinear susceptibility are given in Table 6.2.

There are several research papers reporting on the nonlinear optical properties of different materials using CW He-Ne laser. To the best of our knowledge, the reported values here are larger under cw excitation till date. This suggests that the films are characterized by high nonlinearity with thermal contributions in the CW laser regime. Shin et al.(2000) and Mathews et al.(2007) reported the highest value of $\chi^{(3)}$ to be of the order 10^{-4} esu under cw He-Ne laser illumination. It is evident that our estimated values for MZO samples are one order of magnitude higher than there. Concentration dependence of the nonlinear refractive index n$_2$ and nonlinear absorption coefficient β_{eff} was also studied.

Figure 6.9(a) shows the nonlinear refractive index n$_2$ and nonlinear absorption coefficient β_{eff} as a function of sample doping concentrations for Mn doped and undoped ZnO thin films. It has been found that the n$_2$ and β_{eff} are linearly dependent at lower concentrations of the films within the range studied. The β_{eff} and n$_2$ increases with the concentration. This may be attributed to the fact that the number of particles participating, increases with increase in concentration and more number of particles are thermally agitated resulting in increase in third-order optical nonlinearity.

Table 6.3: Table depicting the recently reported β_{eff} and n_2 values of different semiconductors with cw laser excitation

Sl. No.	Materials	β_{eff} (cm/W)	n_2 (cm^2/W)	Laser wavelength (nm)
1	ZnS nanoparticles (Dehghani et al. 2011)	-3.2×10^{-3}	-1.38×10^{-8}	632.8
2	Polymer Nanocomposite films (Frobel et al. 2011)	45.5×10^{-2}	-2.75×10^{-7}	442
3	ZnSe/PVA nanocomposite film (Sharma and Tripathi 2012)	4.52×10^{-5}	$--$	633
4	Colloidal ZnO nanoparticles (Koushki et al. 2011)	-1.23×10^{-7}	-0.95×10^{-3}	632.8
5	Mn doped ZnS nanoparticles (Somayeh et al. 2011)	1.52×10^{-8}	-4.7×10^{-3}	632.8
6	CdTe quantum dots (Dancus et al. 2008)	-5.5×10^{-8}	$-$	550
7	In_2O_3 nanoparticles (Yu et al. 1997)	$-$	-3.89×10^{-7}	632.8
		$-$	-4.04×10^{-7}	514.5
		$-$	-4.05×10^{-7}	488
		$-$	-4.43×10^{-7}	457.9
8	PbS nanocomposite film (Kurian and Vijayan 2009)	$-$	-3.5×10^{-7}	632.8

6.4.2.2 Optical power limiting

With the extensive use of CW lasers, there arises the need for optical power limiters working in that power regime. An ideal optical power limiter has a linear transmission below a threshold and clamps the output to a constant above it, thus providing safety to sensors or eye. The minimum criteria identified for a material to act as an effective optical limiter are low limiting threshold, high linear transmittance throughout the sensor band width, stability, etc. (Srinivas et al. 2001). The optical limiting behavior of all the films was studied under CW laser illumination. The optical limiting experimental setup is very similar to the z-scan geometry. Figure 6.9(b) show the characteristic optical limiting curves of the Mn doped and undoped ZnO films. It is shown clearly in the Figure 6.9(b) that at low incident energy, the output varies linearly with input energy. The deviations from linearity began at $\sim$5 mW for the doped films and the maximum output clamping occurred at $\sim$12 mW. In the optical power limiting, concentration dependence plays an important role. The transmittance decreases and the optical limiting increases with the increase in Mn concentration. This is because a sample with high concentration has more particles per unit volume participating in the interaction during nonlinear absorption process.

Optical limiting can be achieved by means of various nonlinear optical mechanisms, including self-focusing, self-defocussing, induced scattering, induced-refraction, induced aberration, excited state absorption, two-photon absorption, photo-refraction and free-carrier absorption in nonlinear optical media. In our case the optical limiter is energy absorbing type, the major nonlinear mechanism is due to RSA and FCA is the process leading to nonlinear absorption in semiconductors. Therefore we attribute the optical power limiting behavior in Mn doped and undoped ZnO films to FCA.

The samples were examined using optical microscopy before and after the laser irradiation to check any damage in the films. We found no damage of the films at the region where z-scan data was obtained at the input intensity used, indicating the photo-stability of the thin films.

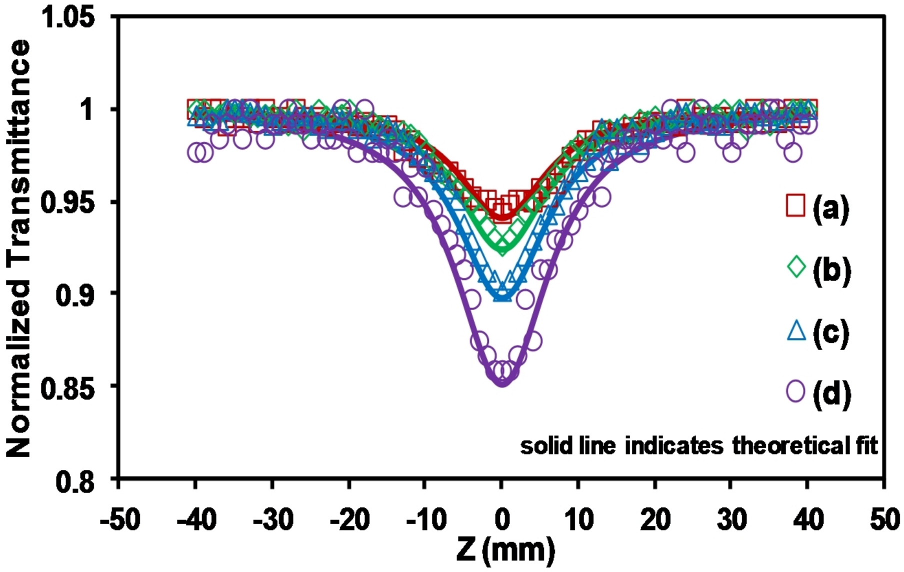

(a)

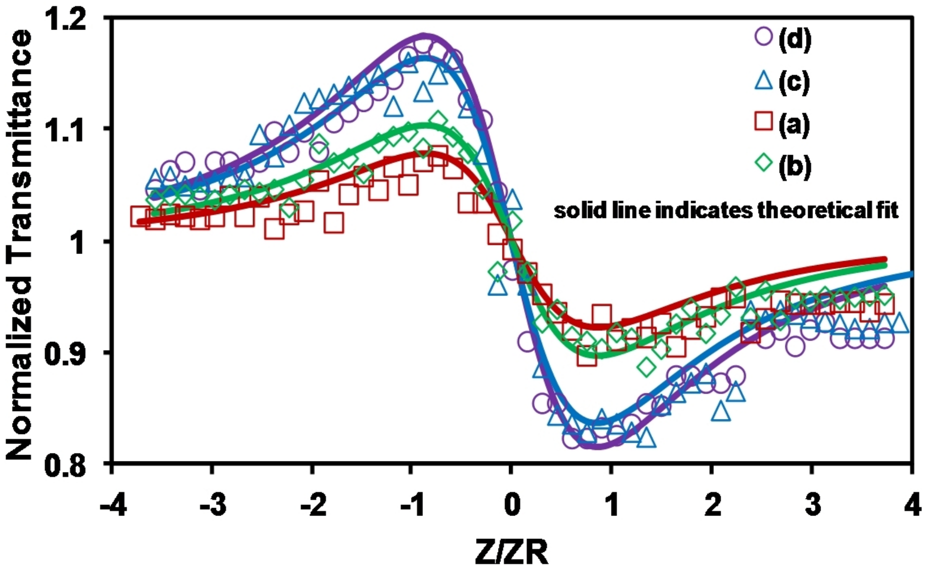

(b)

Figure 6.9: The comparative studies using z-scan (a) open aperture (b) closed aperture traces of (a) Undoped (b) 5 wt.% Mn (c) 10 wt.% Mn & (d) 15 wt.% Mn doped ZnO thin films. Solid line depicts theoretical fit.

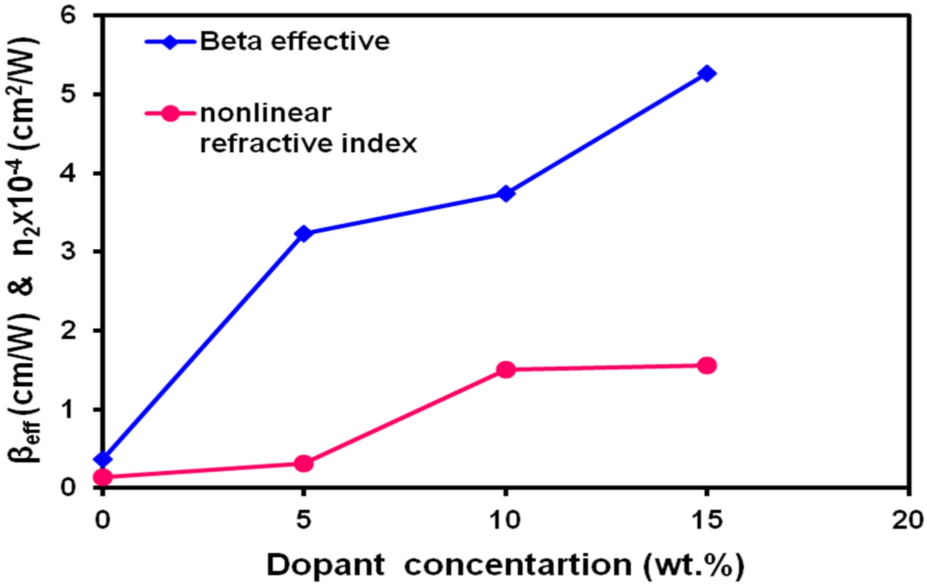

(a)

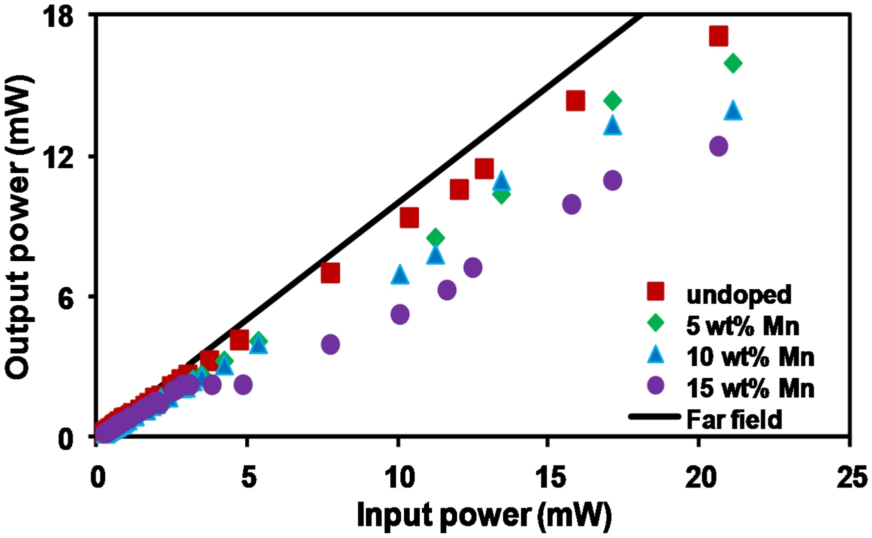

(b)

Figure 6.10: (a) The concentration dependence of nonlinear absorption coefficient β_{eff} and nonlinear refraction coefficient n_2 of Mn doped ZnO thin films. (b)The optical power limiting response of undoped, 5 wt.% Mn, 10 wt.% Mn and 15 wt.% Mn doped ZnO thin films.

6.5 Conclusions

The third-order nonlinear optical properties of Mn doped ZnO thin films deposited by RF magnetron sputtering technique was investigated with cw He-Ne laser at 633 nm wavelength using z- scan technique. The XRD results show the decrease of lattice parameters a and c after doping of Mn into ZnO, due to the substitution of Mn^{4+} and Mn^{3+} ions to Zn^{2+} ions. The AFM results reveal a decrease in the grain size and surface roughness with the increase in Mn content. The optical energy band gap of Mn doped ZnO films is tunable between 3.20 eV and 3.34 eV with increase in Mn concentration. The third-order nonlinear susceptibility obtained for Mn doped ZnO films is as large as 10^{-3} esu. The optical power limiting measurements indicated that the Mn doped ZnO films exhibits good optical limiting at 633 nm wavelength. The nonlinearity leading to optical power limiting behaviour of Mn doped and undoped ZnO films is attributed to RSA. Hence, the Mn doped ZnO films may be a possible candidate for the protection of sensors.

Chapter 7

Conclusions and Future Directions

The conclusions of the thesis and scope for future directions are presented in this chapter.

7.1 Conclusions

- The undoped zinc oxide thin films using sputtering were deposited on glass and quartz substrates. The effect deposition parameters on the structural and optical properties were studied.

- The films show good optical transmittance above 85% in 400-900 nm range. The energy band gap of the films decrease with the increase in the sputter power due to increase in the grain size.

- The characteristic X-ray diffraction peaks for reactively sputtered ZnO were observed and they are well in agreement with the JCPDS. The ZnO films shown a strong preferred orientation along c-axis. This was confirmed by a strong peak corresponding to (0 0 2) planes of Wurtzite ZnO. The films show increase in the crystallinty with the sputter power. But, it is found to decrease with the increase in working pressure

- The stresses in the films were compressive in nature and found to decrease with the increase in the sputter power. Stresses in the films deposited by RF sputtering were smaller than those of the reactively sputtered films.

- Annealing at higher temperatures lead to the formation of Tridymite phase of SiO_2 in the ZnO films deposited on quartz. The appearance of extraneous phase was confirmed by atomic force microscope (AFM) images and optical transmittance spectra. From the z-scan measurements, the films were characterized with negative nonlinear refraction.

- The enhanced nonlinear response of the films was observed with the increase in the annealing temperature for ZnO films deposited on quartz. Multiple diffraction rings due to the refractive index change and thermal lensing were observed when the samples exposed to laser beam. The films also exhibited strong optical limiting properties.

- The electrical resistance of the AZO films found to decrease with the increase in the Al content in the films up to 2 wt.%. The bandgap considerably decreases with the Al content in the films up to 2 wt.%, attributed to B-M effect.

- XRD patterns of the ZnO/Al/ZnO multilayers show reflections corresponding to Wurtzite ZnO, no peaks corresponding to Al observed due to thicker ZnO layers. The sheet resistance of the multilayers found to decrease with the increase in the Al interlayer thickness. But, the average transmittance in the visible region decreases.

- The XRD results for Mn doped ZnO films show decrease of lattice parameters a and c after doping of Mn into ZnO, due to the substitution of Mn^{4+} and Mn^{3+} ions to Zn^{2+} ions. The AFM results reveal a decrease in the grain size and surface roughness with the increase in Mn content. The energy band gap of Mn doped ZnO films is tunable between 3.20 eV and 3.34 eV with increase in Mn concentration. The third-order nonlinear susceptibility obtained for MZO films is as large as 10^{-3} esu. MZO films exhibits good optical limiting at a wavelength of 633 nm.

7.2 Future Directions

- We have fabricated the multilayered structure for possible TCO applications. The nonlinear optical properties of these multilayers will be of specific interest as these contains interfaces.

- The electrical properties of AZO films were studied in this thesis. The effect of co-doping of fluorine, nitrogen may be studied to achieve improved properties.

- The comparative study of nonlinear properties of doped ZnO films under CW and pulsed regime may give more information on the origin of nonlinear response in ZnO. The magnetic properties of transition metal doped ZnO can be studied and a clear understanding about the origin of magnetic properties may be investigated.

Bibliography

Abed, S., Aida, M. S., Bouchouit, K., Arbaoui, A., Iliopoulos, K., and Sahraoui, B. (2011). Non-linear optical and electrical properties of ZnO doped Ni thin films obtained using spray ultrasonic technique. *Opt. Mater.*, 33:968–972.

Aghamalyan, N. R., Gambaryan, I. A., Goulanian, E. K., Hovsepyan, R. K., Kostanyan, R. B., Vardanyan, S. I. P. E. S., and Zerrouk, A. F. (2003). Influence of thermal annealing on optical and electrical properties of ZnO films prepared by electron beam evaporation. *Semicond. Sci. Technol.*, 18:525–529.

Ahn, C. H., Kim, Y. Y., Kang, S. W., Kong, B. H., Mohanta, S. K., Cho, H. K., Kim, J. H., and Lee, H. S. (2008). Dependency of oxygen partial pressure on the characteristics of ZnO films grown by radio frequency magnetron sputtering. *J. Mater. Sci.:Mater Electron.*, 19:744–748.

Ara, M. H. M., Salmani, S., Mousavi, S. H., and Koushki, E. (2010). Investigation of nonlinear optical responses and observing diffraction rings in acid dye (patent green). *Curr. Appl. Phys.*, 10:997–1001.

Ayadi, Z. B., Mir, L. E., Djessas, K., and Alaya, S. (2007). Electrical and optical properties of aluminum-doped zinc oxide sputtered from an aerogel nanopowder target. *Nanotechnology*, 18:445702.

Babar, A. R., Deshamukh, P. R., Rajpure, K. Y., Deokate, R. J., Haranath, D., and Bhosale, C. H. (2008). Gallium doping in transparent conductive ZnO thin films prepared by chemical spray pyrolysis. *J. Phys. D: Appl. Phys.*, 41:135404.

Bagnall, D. M., Chen, Y. F., Zhu, Z., Yao, T., Koyama, S., Shen, M. Y., and Goto, T.

(1997). Optically pumped lasing of ZnO at room temperature. *Appl. Phys. Lett.*, 70:2230.

Bahedi, K., Addou, M., Jouad, M. E., Sofiani, Z., Lamrani, M. A., Habbani, T. E., Fellahi, N., Bayoud, S., Dghoughi, L., Sahraoui, B., and Essaidi, Z. (2009). Diagnostic study of the roughness surface effect of zirconium on the third-order nonlinear-optical properties of thin films based on zinc oxide nanomaterials. *Appl. Surf. Sci.*, 255:4693–4695.

Bai, S.-N. and Tseng, T.-Y. (2009). Electrical and optical properties of ZnO:Al thin films grown by magnetron sputtering. *J. Mater. Sci.:Mater. Electron.*, 20:253–256.

Bender, M., Seelig, W., Daube, C., Frankenberger, H., Ocker, B., and Stollenwerk, J. (1998). Dependence of film composition and thicknesses on optical and electrical properties of ITOmetalITO multilayers. *Thin Solid Films*, 326:67–71.

Berginski, M., Hpkes, J., Schulte, M., Schpe, G., Stiebig, H., Rech, B., and Wuttig, M. (2007). The effect of front ZnO:Al surface texture and optical transparency on efficient light trapping in silicon thin-film solar cells. *J. Appl. Phys.*, 101:074903.

Bhatti, K. P., Chaudhary, S., Pandya, D. K., and Kashyap, S. C. (2005). On the room-temperature ferromagnetism in $(\mathrm{ZnO})_{0.98}(\mathrm{MnO}_2)_{0.02}$. *Solid State Commun*, 136:384–388.

Bolger, J. A., Kar, A. K., Wherret, B. S., Salvo, R. D., D. C, H., and Hagan, D. J. (1993). Nondegenerate two-photon absorption spectra of ZnSe, ZnS and ZnO. *Optics Comm.*, 97:203–209.

Boyd, R. W. (2008). *Nonlinear Optics*. Elsevier Inc., 3rd edition.

Burstein, E. (1954). Anomalous optical absorption limit in InSb. *Phys. Rev.*, 93:632–633.

Caglar, M., SalihaIlican, Caglar, Y., and Yakuphanoglu, F. (2008). The effects of Al doping on the optical constants of ZnO thin films prepared by spray pyrolysis method. *J. Mater. Sci.:Mater. Electron.*, 19:704–704.

Cao, H., Wu, J. Y., Ong, H. C., Dai, J. Y., and Chang, R. P. H. (1998). Second harmonic generation in laser ablated zinc oxide thin films. *Appl. Phys. Lett.*, 73:572.

Cebulla, R., Wendt, R., and Ellmer, K. (1998). Al-doped zinc oxide films deposited by simultaneous rf and dc excitation of a magnetron plasma: Relationships between plasma parameters and structural and electrical film properties. *J. Appl. Phys.*, 83:1087.

Chen, M., Pei, Z. L., Wang, X., Sun, C., and Wen, L. S. (2001). ZAO: An attractive potential substitute for ITO in flat display panels. *Mater. Sci. Eng. B*, 85:212–217.

Chikoidze, E., Dumont, Y., Jomard, F., and Gorochov, O. (2007). Electrical and optical properties of ZnO:Mn thin films grown by MOCVD. *Thin Solid Films*, 515:8519–8523.

Christodoulides, D. N., Khoo, I. C., Salamo, G. J., Stegeman, G. I., and Stryland, E. W. V. (2010). Nonlinear refraction and absorption: mechanisms and magnitudes. *Advanc. Opt. Photonics*, 2:60–200.

Chu, S., Olmedo, M., Yang, Z., Kong, J., and Liu, J. (2008). Electrically pumped ultraviolet ZnO diode lasers on Si. *Appl. Phys. Lett.*, 93:181106.

Cullity, B. D. (1978). *Elements of X-ray diffraction*. Prentice Hall.

Dancus, I., Vlad, V. I., Petris, A., Gaponika, N., Shavela, A., and Eychmullera, A. (2008). Nonlinear optical properties of CdTe qds near the resonance regime. *J. Optoelectron. Adv. Mater.*, 10:149–151.

David, E. A. and Mott, N. F. (1970). Conduction in non-crystalline systems V. conductivity, optical absorption and photoconductivity in amorphous semiconductors. *Philos. Mag.*, 22:903.

Dehghani, Z., Nazerdeylami, S., Saievar-Iranizad, E., and Ara, M. H. M. (2011). Synthesis and investigation of nonlinear optical properties of semiconductor ZnS nanoparticles. *J. Phys. Chem. Solids*, 72:1008–1010.

Deng, Z., Huang, C., Huang, J., Wang, M., He, H., Wang, H., and Cao, Y. (2010). Effects of Al content on the properties of ZnO:Al films prepared by Al_2O_3 and ZnO co-sputtering. *J.Mater. Sci.:Mater. Electron.*

Dietl, T., Ohno, H., Matsukura, F., Cibert, J., and Ferrand, D. (2000). Zener model description of ferromagnetism in zinc-blende magnetic semiconductors. *Science*, 287:1019–1022.

Dong, W. W., Zhu, X., RuhuaTao, and Fang, X. (2008). Effect of homo-buffer layers on the optical properties of ZnO thin films grown by pulsed laser deposition on Si (100). *J. Mater. Sci. :Mater. Electron.*, 19:538–542.

Egerton, R. F. (2005). *Physical Principles of Electron Microscopy:An Introduction to TEM, SEM, and AEM*. Springer Science+Business Media, Inc, New York.

Elanchezhiyan, J., Bhuvana, K. P., Gopalakrishnan, N., and Balasubramanian, T. (2008). Investigation on Mn doped ZnO thin films grown by rf magnetron sputtering. *Mater. Lett.*, 62:3379–3381.

Fahland, M., Karlsson, P., and Charton, C. (2001). Low resisitivity transparent electrodes for displays on polymer substrates. *Thin Solid Films*, 392:334.

Feil, G. T., Ma, Ying, Z. F., and Zhang, L. D. (1999). Third-order nonlinear optical properties and the influence of surface state of nanoscale Ag particles dispersed in silicon oil. *Mater. Res. Bull.*, 34:217–224.

Franken, P. A., Hill, A. E., Peters, C. W., and Weinreich, G. (1961). Generation of optical harmonics. *Phys. Rev. Lett.*, 7:118.

Frobel, P. G. L., Suresh, S. R., Mayadevi, S., Sreeja, S., Mukherjee, C., and Muneera, C. I. (2011). Intense low threshold nonlinear absorption and nonlinear refraction in a new organic-polymer nanocomposite. *Mater. Chem. Phys.*, 129:981–989.

Fujihara, S., Sasaki, C., and Kimura, T. (2001). Effects of Li and Mg doping on microstructure and properties of sol-gel ZnO thin films. *J. Eur. Ceram. Soc.*, 21:2109–2112.

Fujimura, N., Nishihara, T., Goto, S., Xu, J., and Ito, T. (1993). Control of preferred orientation for ZnO$_x$ films: control of self-texture. *J. Cryst. Growth*, 130:269–279.

Gayathri, C. and Ramalingam, A. (2008). Studies of third-order optical limiting properties of azo dyes. *Spectrochem. Acta A*, 69:980–984.

Geethakrishnan, T. and Palanisamy, P. K. (2007). Z-scan determination of the third-order optical nonlinearity of a triphenylmethane dye using 633 nm He-Ne laser. *Opt. Commun.*, 270:424–428.

Gerward, L. and Olsen, J. S. (1995). The high-pressure phase of zincite. *J. Synchrotron Rad.*, 2:233–235.

Ghaleh, K. J., Salmani, S., and Ara, M. H. M. (2007). Nonlinear responses and optical limiting behaviour of fast green FCF dye under a low power CW He-Ne laser irradiation. *Opt. Commun.*, 271:551–554.

Hagen, D. J. (2001). *Hand Book of Optics Volume 4*. McGraw Hill USA.

Han, J., Mantas, P., and Senos, A. (2000). Grain growth in Mn-doped ZnO. *J. Eur. Ceram. Soc.*, 20:2573.

Han, Y. B., Han, J. B., Ding, S., Chen, D. J., and Wang, Q. Q. (2005). Optical nonlinearity of ZnO microcrystallite enhanced by interfacial state. *Opt. Express*, 13:9212–9216.

He, G., Weder, C., Smith, P., and Prasad, P. (1998). Optical power limiting and stabilization based on a novel polymer compound. *IEEE J. Quantum Electron.*, 34:2279.

He, G. S., Ken-Tye, Y., Qingdong, Z., Yudhisthira, S., Alexander, B., Aleksandr, I. R., and Prasad, P. N. (2007). Multi-photon excitation properties of CdSe quantum dots solutions and optical limiting behavior in infrared range. *Opt. Exp.*, 15:12818–12833.

Henari, F. Z. and Cassidy, S. (2011). Nonlinear optical properties and all optical switching of congo red in solution. *Optik*, 123:711–714.

Henari, F. Z. and Mohamed, A. Y. A. (2008). Nonlinear refractive index measurements of tris(acetylacetonato) manganese (iii) solution. *Opt. Laser Technol.*, 40:602–606.

Hong, R., Huang, J., He, H., Fan, Z., and Shao, J. (2005). Influence of different post treatments on the structure and optical properties of zinc oxide thin films. *Appl. Surf. Sci., 242,*, 242:346–352.

Hupkes, J., Rech, B., Calnan, S., Kluth, O., Zastrow, U., Siekmann, H., and Wuttig, M. (2006). Material study on reactively sputtered zinc oxide for thin film silicon solar cells. *Thin Solid Films*, 502:286–291.

Hyojungyu and Sok, W. K. (2005). Temperature effects in an optical limiter using carbon nanotube suspensions. *J Korean. Phys. Soc.*, 47:610–614.

Im, S., Jin, B. J., and Yi, S. (2000). Ultraviolet emission and microstructural evolution in pulsed-laser-deposited ZnO films. *J. Appl. Phys.*, 87:4558.

Ip, K., Frazier, R. M., Heo, Y. W., Norton, D. P., Abernathy, C. R., Pearton, S. J., J. Kelly, R., Rairigh, Hebard, A. F., Zavada, J. M., and Wilson, R. G. (2003). Ferromagnetism in Mn- and Co-implanted ZnO nanorods. *J. Vac. Sci. Technol. B*, 21:1476–1481.

Irimpan, L., Ambika, D., Kumar, V., Nampoori, V. P. N., and Radhakrishnan, P. (2008a). Effect of annealing on spectral and NLO properties of ZnO thin films. *J. Appl. Phys.*, 104:033118–033126.

Irimpan, L., Krishnan, B., Deepthy, A., Nampoori, V. P. N., and 103, P. R. (2008b). Size dependent enhancement of nonlinear optical properties in nano colloids of ZnO. *J. Appl. Phys*, 103:033105.

Ito, S., Takeuchi, T., Katayama, T., and M. Sugiyama, . (2003). Conductive and transparent multilayer films for low-temperature-sintered mesoporous TiO_2 electrodes of dye-sensitized solar cells. *Chem. Mater.*, 15:2824–2828.

Jagadish, C. and Pearton, S. J., editors (2006). *Zinc Oxide Bulk, Thin Films and Nanostructures: Processing, Properties, and Applications*. Elsevier.

Jansseune, T. (2005). Indium price soars as demand for displays continues to grow. *Compound Semicond.*, 11:34.

Jayaraj, M. K., Anthony, A., and Ramachandran, M. (2002). Transparent conducting zinc oxide thin film prepared by off-axis rf magnetron sputtering. *Bull. Mater. Sci.*, 25:227–230.

Jeon, K. A., Kim, J. H., Shim, W. Y., Lee, W. Y., Jung, M. H., and Lee, S. Y. (2006). Magnetic and optical properties of Zn_{1-x} Mn_xO thin films prepared by pulsed laser deposition. *J. Cryst. Growth*, 28:66–69.

Jia, T., He, T., Li, P., Mo, Y., and Cui, Y. (2008). A study of the thermal-induced nonlinearity of Au and Ag colloids prepared by the chemical reaction method. *Opt. Laser Technol.*, 40:936–940.

Jiang, M. and Liu, X. (2009). Preparation and optical properties of Bi doped ZnO thin films with (100) orientation by rf magnetron sputtering. *J. Mater. Sci.:Mater. Electron.*, 20:972–976.

Jiang, M., Liu, X., Chen, G., Cheng, J., and Zhou, X. (2009). Preparation and photoelectric properties of Ti doped ZnO thin films annealed in vacuum. *J. Mater. Sci.:Mater. Electron.*, 20:1225–1228.

Jin, J., Chang, G. S., Boukhvalov, D. W., Zhang, X. Y., Finkelstein, L. D., Xu, W., Kurmaev, Y. X. Z. E. Z., and Moewes, A. (2010). Element-specific electronic structure of Mn dopants and ferromagnetism of (Zn,Mn)O thin films. *Thin Solid Films*, 518:2825–2829.

Jung, S. W., An, S. J., Chul, G., Jung, C. U., Lee, S., and Cho, S. (2002). Ferromagnetic properties of $Zn_{1-x}Mn_xO$ epitaxial thin films. *Appl. Phys. Lett.*, 80:4561–4563.

Kaiser, W. and Garrett, C. (1961). Two-photon excitation in CaF_2: Eu^{2+}. *Phys. Rev. Lett.*, 7:229–231.

Kaladevi, S., Vijayan, C., and Kothiyal, M. P. (2006). Low threshold optical power limiting of cw laser illumination based on nonlinear refraction in zinc tetraphenyl porphyrin. *Opt. Laser Technol.*, 38:512–515.

Kang, H. S., Kang, J. S., Kim, J. W., and Lee, S. Y. (2004). Annealing effect on the property of ultraviolet and green emissions of ZnO thin films. *J. Appl. Phys.*, 95:1246.

Karamat, S., S.Mahmood, Lin, J. J., Pan, Z. Y., Lee, P., Tan, T. L., Springhama, S. V., Ramanujan, R. V., and Rawat, R. S. (2008). Structural, optical and magnetic properties of $(ZnO)_{1-x}(MnO_2)_x$ thin films deposited at room temperature. *Appl. Surf. Sci.*, 254:7285–7289.

Kawashima, T., Ezure, T., Okada, K., Mastui, H., Goto, K., and Tanabe, N. (2004). FTO/ITO double-layered transparent conductive oxide for dye-sensitized solar cells. *J. Photochem. Photobiol.-A*, 164:199–202.

Kim, H., Pique, A., Horwitz, J. S., Murata, H., Kafafi, Z. H., Gilmore, C. M., and Chrisey, D. B. (2000). Effect of aluminum doping on zinc oxide thin films grown by pulsed laser deposition for organic light-emitting devices. *Thin Solid Films*, 377-378:798–802.

Kim, K. J. and Park, Y. R. (2003). Optical absorption and electronic structure of $Zn_{1-x}Mn_xO$ alloys studied by spectroscopic ellipsometry. *J. Appl. Phys.*, 94:867–869.

Kim, S. S., Moon, J. H., Lee, B.-T., Song, O. S., and Je, J. H. (2004). Heteroepitaxial growth behavior of Mn-doped ZnOthin films on Al_2O_3 (0001) by pulsed laser deposition. *J. Appl. Phys.*, 95:454–459.

Kisi, E. H. and Elcombe, M. M. (1989). u parameters for the wurtzite structure of ZnS and ZnO using powder neutron diffraction. *Acta Cryst.*, C45:1867–1870.

Kittilstved, K. R., Zhao, J., Liu, W. K., Bryan, J. D., Schwartz, D. A., and Daniel R. Gamelina (2006). ., 89, . (2006). Magnetic circular dichroism of ferromagnetic Co^{2+}-doped ZnO. *Appl. Phys. Lett.*, 89:062510.

Koidl, P. (1977). Optical absorption of Co^{2+} in ZnO. *Phys. Rev. B*, 15:2493–2499.

Koidl, P., Schirmer, O., and Kaufmann, U. (1973). Near-infrared absorption of Co^{2+} in ZnS: Weak jahn-teller coupling in the $^4T_1$ and$^4T_2$ states. *Phys. Rev. B*, 8:4926–4934.

Koushki, E., Ara, M. H. M., Mousavi, S. H., and Haratizadeh, H. (2011). Temperature effect on optical properties of colloidal ZnO nanoparticles. *Curr. Appl. Phys.*, 11:1164–1167.

Kryshtab, T., Khomchenko, V. S., Khachatryan, V. B., Roshchina, N. N., Andraca-Adame, J. A., Lytvyn, O. S., and Kushnirenko, V. I. (2007). Effect of doping on properties of ZnO:Cu and ZnO:Ag thin films. *J. Mater. Sci: Mater. Electron.*, 18:1115–1118.

Kumari, V., Kumar, V., Malik, B. P., Mehra, R. M., and Mohan, D. (2012). Nonlinear optical properties of erbium doped zinc oxide (EZO) thin films. *Opt. Commun.*, 285:2182–2188.

Kurian, P. A. and Vijayan, C. (2009). Spatial phase filtering based on the intensity-dependent refractive index of PbS nanocomposite film. *Appl. Opt.*, 48:5259–5265.

Kusano, E., Kawaguchi, J., and Enjoiji, K. (1986). Thermal stability of heat-reflective films consisting of oxide-Ag-oxide deposited by dc magnetron sputtering. *J. Vac. Sci. Technol. A*, 4(6):2907–2910.

Lai, L.-W. and Lee, C.-T. (2009). Investigation of optical and electrical properties of ZnO thin films. *Mater. Chem. Phys.*, 110:393–396.

Lamrani, M. A., Addou, M., Sofiani, Z., Sahraoui, B., Sahraoui, B., Ebothe, J., Hichou, A. E., Fellahi, N., Bernede, J. C., and Dounia, R. (2007). Cathodoluminescent and nonlinear optical properties of undoped and erbium doped nanostructured ZnO films deposited by spray pyrolysis. *Opt. Commun.*, 277:196–201.

Larciprete, M. C., Haertle, D., Belardini, A., Bertolotti, M., Sarto, F., and Gunter, P. (2006). Characterization of second and third order optical nonlinearities of ZnO sputtered films. *Appl. Phys. B*, 82:431–437.

Laud, B. B. (1991). *Lasers & Nonlinear optics, second edition*. Wiley Eastern Limited.

Lee, C., Dwivedi, R. P., Lee, W., hong, C., Lee, W. I., and Kim, H. W. (2008). IZO/Al/GZO multilayer films to replace ITO films. *J. Mater. Sci.:Mater. Electron.*, 19:981–985.

Lee, Y. E., Lee, J. B., Kim, Y. J., Yang, H. K., Park, J. C., and Kim, H. J. (1996). Microstructural evolution and preferred orientation change of radio-frequency-magnetron sputtered ZnO thin films. *J. Vac. Sci. Technol. A*, 14:1943–1948.

Leftheriotis, G., Papaefthimiou, S., and Yianoulis, P. (2000). Development of multilayer transparent conductive coatings. *Solid State Ionics*, 136-137:655–661.

Lide, D. R., editor (1992). *CRC Handbook of Chemistry and Physics*. CRC Press, New York, 73 edition.

Liu, H., Qiu, H., Chen, X., Yu, M., and Wang, M. (2009a). Structural and physical properties of ZnO:Al films grown on glass by direct current magnetron sputtering with the oblique target. *Curr. Appl. Phys*, 9:1217–1222.

Liu, Y., hong Yang, S., li Zhang, Y., and hua Bao, D. (2009b). Influence of annealing temperature on structural, optical and magnetic properties of Mn-doped ZnO thin films prepared by sol-gel method. *J. Magn. Magn. Mater.*, 321:3406–3410.

Look, D. C., B. Claflin, Y., Alivov, T., and Park, S. J. (2004). The future of ZnO light emitters. *Phys. Stat. Sol. (a)*, 201:2203–2212.

Look, D. C., Reynolds, D. C., Hemsky, J. W., Jones, R. L., and Sizelove, J. R. (1999). Production and annealing of electron irradiation damage in zno. *Appl. Phys. Lett.*, 75:811–813.

Lupan, O., Pauporte, T., Bahers, T. L., Viana, B., and Ni, I. C. (2011). Wavelength-emission tuning of ZnO nanowire-based light-emitting diodes by Cu doping: Experimental and computational insights. *Adv. Funct. Mater.*, 21:3564–3572.

M.-Saavedra, O. G. and Castaneda, L. (2007). Second harmonic generation of fluorine-doped zinc oxide thin films grown on soda-lime glass substrates by a chemical spray technique. *Optics Communications*, 269:370–377.

Ma, Q.-B., Ye, Z.-Z., He, H.-P., Zhu, L.-P., Wang, J.-R., and Zhao, B.-H. (2007). Influence of Ar/O_2 ratio on the properties of transparent conductive ZnO:Ga films prepared by DC reactive magnetron sputtering. *Mater. Lett.*, 61:2460–2463.

Maissel, L. and Glang, R. (1970). *Handbook of Thin Film Technology*. McGraw-Hill, New York.

Major, K. L., Chopra, S., and Pandya, D. (1983). Transparent conductors-A status reviews. *Thin Solid Films*, 102:1–46.

Mandal, S. K., Das, A. K., Nath, T. K., Karmakar, D., and Satpati, B. (2006). Microstructural and magnetic properties of ZnO:TM (TM=Co,Mn) diluted magnetic semiconducting nanoparticles. *Appl. Phys. Lett.*, 100:104315.

Mandal, S. K. and Nath, T. K. (2006). Microstructural, magnetic and optical properties of ZnO:Mn $(0.01 \leq x \leq 0.25)$ epitaxial diluted magnetic semiconducting films. *Thin Solid Films*, 515:2535–2541.

Martin, E. J. J., Yan, M., Lane, M., Ireland, J., Kannewurf, C. R., and Chang, R. P. H. (2004). Properties of multilayer transparent conducting oxide films. *Thin Solid Films*, 461:309–315.

Martin-Gonzalez, M. S., Steplecaru, C. S., Briones, F., Liopez-Ponce, E., Fernndez, J. F., Garcia, M. A., Quesada, A., Ballesteros, C., and Costa-Kramer, J. L. (2010). Microstructure, interdiffusion and magnetic properties of ZnO/MnO_x multilayers grown by pulsed laser deposition. *Thin Solid Films*, 518:4607–4611.

Mathews, S. J., Kumar, S. C., Giribabu, L., and Rao, S. V. (2007). Large third order nonlinear optical and optical limiting properties of symmetric and unsymmetrical phthalocyanines studied using Z-scan. *Opt. Commun.*, 280:206–212.

Minami, T. (2005). Transparent conducting oxide semiconductors for transparent electrodes. *Semicond. Sci. Technol.*, 20:S35–S44.

Minami, T. (2012). Impurity-doped ZnO thin films prepared by physical deposition methods appropriate for transparent electrode applications in thin-film solar cells. In *Materials science and Enginering*. IOP Publishing.

Minami, T., Miyata, T., Ihara, K., Minamino, Y., and Tsukada, S. (2006). Effect of ZnO film deposition methods on the photovoltaic properties of ZnOCu$_2$O heterojunction devices. *Thin Solid Films*, 494:47–52.

Mitra, A. and Thareja, R. K. (2001). Dependence of second harmonic generation on size of nanocrystallites of ZnO. *Modern Phys. Lett. B*, 15:515.

Mohammed, A. Q. and Palanisamy, P. K. (2006). Z-scan determination of the third-order optical nonlinearity of organic dye nile blue chloride. *Mod. Phys. Lett. B*, 20:623–632.

Morkoc, H. and Ozgur, U. (2009). *Zinc Oxide fundamentals, Materials and Device technology*. Wiley-VCH.

Moss, T. S. (1954). The interpretation of the properties of indium antimonide. *Proc. Phys. Soc. B*, 67:775.

Mott, N. F. and Davis, E. A. (1979). *Electronic Processes in Non-crystalline Materials,*. Clarendon Press, Oxford.

Neethling, P. (2005). *Determination of nonlinear properties using Z-scan*.

Neumann, U., Grunwaid, R., Griebner, U., Steinmeyer, G., and Seeber, W. (2004). Second-harmonic efficiency of ZnO nanolayers. *Appl. Phys. Lett.*, 84:170–172.

Ning, T., JiLiang, W., HengXing, X., HongYong, P., and Chao, F. (2009). Optical characterization of ZnO thin films deposited by rf magnetron sputtering method. *Sci. China Ser. E-Tech Sci*, 52:2200–2203.

Ozgur, U., Alivov, Y. I., Liu, C., Teke, A., Reshchikov, M. A., Dogan, S., Avrutin, V., Cho, S.-J., and Morkoc, H. (2005). A comprehensive review of zno materials and devices. *J. Appl. Phys.*, 98:041301.

Pandey, B., Ghosh, S., Srivastava, P., Avasthi, D. K., Kabiraj, D., and Pivin, J. C. (2008). Synthesis and characterization of Ni-doped ZnO: A transparent magnetic semiconductor. *J. Magn. Magn. Mater.*, 320:3347–3351.

Pearton, S. J., Abernathy, C. R., Overberg, M. E., Thaler, G. T., Norton, D. P., Theodoropoulou, Hebard, A. F., Park, Y. D., Ren, F., Kim., J., and Boatner, L. A. (2003). Wide band gap ferromagnetic semiconductors and oxides. *J. Appl. Phys.*, 93:1–13.

Pearton, S. J., Lim, W. T., Wright, J. S., Tien, L. C., Kim, H. S., Norton, D. P., Wang, H. T., Kang, B. S., Ren, F., Jun, J., Lin, J., and Osinsky4, A. (2008). Zno and related materials for sensors and light-emitting diodes. *J. Electron. Mater.*, 37:1426–1432.

Pearton, S. J., Norton, D. P., Ip, K., Heo, Y. W., and Steiner, T. (2004). Recent advances in processing of ZnO. *J. Vac. Sci. Technol. B*, 22.

Philip, R., Kumar, R., Sandhyarani, N., and Pradeep, T. (2000). Picosecond optical nonlinearity in monolayer-protected gold, silver, and gold-silver alloy nanoclusters. *Phys. Rev. B*, 62:13160–13166.

Poornesh, P., Umesh, G., Hegde, P. K., Manjunatha, M. G., B, M. K., and Adhikari, A. V. (2009). Studies on third-order nonlinear optical properties and reverse saturable absorption in polythiophene/poly (methylmethacrylate) composites. *Appl. Phy. B*, 97:117–124.

Prellier, W., Fouchet, A., and Mercey, B. (2003). Oxide-diluted magnetic semiconductors: a review of the experimental status. *J. Phys.: Condens. Matter*, 15:R1583–R1601.

R-Rosales, A. A., M-Saavedra, O. G., Carlos, J., and R-Moreno (2008). Variation of nonlinear refractive index in dye doped liquid crystals by local and nonlocal mechanisms. *Opt. Mater.*, 31:350–360.

Rahaman, M. N. (1995). *Ceramic Processing and Sintering*. Marcel Dekker, New York.

Ramamurthy, N., Dhanuskodi, S., Manjusha, M., and Philip, J. (2011). Low power CW optical limiting properties of bis(2-aminopyridinium)-succinate-succinic acid (2APS) single crystal. *Opt. Mater.*, 33:607–612.

Rashidian, M., Dorranian, D., Darani, S. A., Saghafi, S., and Ghoranneviss, M. (2009). Nonlinear responses and optical limiting behaviour of basic violet 16 dye under cw laser illumination. *Optik*, 120:1000–1006.

Risbud, A. S., Spaldin, N. A., Chen, Z. Q., Stemmer, S., and Seshadri, R. (2003). Magnetism in polycrystalline cobalt-substituted zinc oxide. *Phys. Rev. B*, 68:205202–202209.

Sahu, D. and Huang, J.-L. (2007). The properties of ZnO/Cu/ZnO multilayer films before and after annealing in the different atmosphere. *Thin Solid Films*, 516:208–211.

Sahu, D. R. and Huang, J.-L. (2009). Development of ZnO-based transparent conductive coatings. *Sol. Enrg. Met. Sol. C.*, 93:1923–1927.

Santana-Aranda, M. A., Armenta-Estrada, A., Mendoza-Barrera, C., Michel, C. R., Chavez-Chavez, A., Jimenez-Sandoval, S., and Melendez-Lira, M. (2007). Aluminum doped ZnO by reactive sputtering of coaxial Zn and Al metallic targets. *J. Mater. Sci.:Mater. Electron*, 18:611.

Sathiyamoorthy, K., Vijayan, C., and Kothiyal, M. P. (2008). Low power optical limiting in ClAl-phthalocyanine due to self defocusing and self phase modulation effects. *Opt. Mater.*, 31:79–86.

Sato, K. and Katayama-Yoshida, H. (2000). Material design for transparent ferromagnets with ZnO-based magnetic semiconductors. *Japan. J. Appl. Phys.*, 39:L555–L558.

Sharma, M. and Tripathi, S. K. (2012). Preparation and nonlinear characterization of zinc selenide nanoparticles embedded in polymer matrix. *J. Phys. Chem. Solids*, 73:1075–1081.

Sharma, P., Gupta, A., Rao, K., J.Owens, F., Sharma, R., Ahuja, R., Guillen, J. O., Johansson, B., and Gehring, G. (2003). Ferromagnetism above room temperature in bulk and transparent thin films of Mn-doped ZnO. *Nat. Mater.*, 3:673–677.

Sheik-Bahae, M., Said, A. A., and Stryland, E. W. V. (1989). High-sensitivity, single-beam n_2 measurements. *Opt. Lett.*, 14:955–957.

Sheik-Bahae, M., Said, A. A., Wei, T. H., Hagan, D. J., and Stryland, E. W. V. (1990). Sensitive measurement of optical nonlinearities using a single beam. *IEEE J. Quantum Elect.*, 26:760–769.

Shi, J. H., Huang, S. M., Chu, J. B., Zhu, H. B., Wang, Z. A., Li, X. D., Zhang, D. W., Sun, Z., Cheng, W. J., Huang, F. Q., and ., X. J. Y. . (2010). Effect of ZnO buffer layer on AZO film properties and photovoltaic applications. *J.Mater. Sci.:Mater. Electron.*, 21:1005–1013.

Shin, C. and Lee, H. (2000). A comparative study of third order electronic and thermally induced optical nonlinearity in a polythiophene thin film. *J. Korean Phys. Soc.*, 36:356–359.

Shin, H. H., Joung, Y. H., and Kang, S. J. (2009). Influence of the substrate temperature on the optical and electrical properties of ga-doped zno thin films fabricated by pulsed laser deposition. *J Mater Sci: Mater Electron*, 20:704–708.

Sim, K. U., Shin, S. W., Moholkar, A., Yun, J. H., Moon, J. H., and Kim, J. H. (2010). Effects of dopant (Al, Ga, and In) on the characteristics of ZnO thin films prepared by RF magnetron sputtering system. *Curr. App. Phys.*, 10:S463.

Singh, A. V., Mehraa, R. M., Yoshida, A., and Wakahara, A. (2004). Doping mechanism in aluminum doped zinc oxide films. *J. Appl. Phys*, 95:3640–3643.

Singh, P., Chawla, A. K., Kaur, D., and Chandra, R. (2007). Effect of oxygen partial pressure on the structural an doptical properties of sputter deposited ZnO nanocrystalline thin films. *Mater. Lett.*, 61:2050–2053.

Singh, P., Kaushal, A., and Kaur, D. (2009). Mn-doped Zno nanocrystalline thin films prepared by ultrasonic spray pyrolysis. *J. Alloy. Compd.*, 471:11–15.

Sittinger, V., Ruske, F., Werner, W., Szyszka, B., Rech, B., Hupkes, J., Schope, G., and Stiebig, H. (2006). ZnO:Al films deposited by in-line reactive AC magnetron sputtering for a-Si:H thin film solar cells. *Thin Solid Films*, 496:16–25.

Snure, M., Kumar, D., and Tiwari, A. (2009). Ferromagnetism in ni-doped zno films: Extrinsic or intrinsic?. *Appl. Phys. Lett.*, 94:012510.

Sofiani, Z., Derkowska, B., Dalasiski, P., Wojdyla, M., D.-Seignon, S., Lamrani, M. A., Dghoughi, L., Bala, W., Addou, M., and Sahraoui, B. (2006). Optical properties of ZnO and ZnO:Ce layers grown by spray pyrolysis. *Opt. Commun.*, 267:433–439.

Sofiani, Z., Sahraoui, B., Addou, M., Adhiri, R., Lamrani, M. A., Dghoughi, L., Fellahi, N., Derkowska, B., and Bala, W. (2007). Third harmonic generation in undoped and X doped ZnO films (X: Ce, F, Er, Al, Sn) deposited by spray pyrolysis. *J. Appl. Phys.*, 10:063104.

Somayeh, N., Esmaiel, S.-I., D., Z., and M., M. (2011). Synthesis and photoluminescent and nonlinear optical properties of manganese doped ZnS nanoparticles. *Physica B*, 406:108–111.

Soumahoro, I., Moubah, R., Schmerber, G., Colis, S., Aouaj, M. A., Abd-lefdil, M., Hassanain, N., Berrada, A., and Dinia, A. (2010). Structural, optical, and magnetic properties of Fe-doped ZnO films prepared by spray pyrolysis method. *Thin Solid Films*, 518:4593–4596.

Sreekumar, G., Milka, B. V., Muneera, C. I., Sathiyamoorthy, K., and Vijayan, C. (2007). Nonlinear refraction and optical limiting in solid films of amido black dye under cw laser illumination. *Opt. Mater.*, 30:311–313.

Srikant, V. and Clarke, D. R. (1997). Optical absorption edge of ZnO thin films: the effect of substrate. *J. Appl. Phys.*, 81:6357–6364.

Srinivas, N. K. M. N., Rao, S. V., Rao, D. V. G. L. N., Kimball, B. K., Nakashima, M., Decristofano, B. S., and Rao, D. N. (2001). Wavelength dependent studies of nonlinear absorption in zinc meso-tetra(p-methoxyphenyl)tetrabenzoporphyrin (Znmp TBP) using Z-scan technique. *J. Porphyr. Phthalocya.*, 5:549–554.

Sun, J., Liu, F.-J., Huang, H.-Q., Zhao, J.-W., Hu, Z.-F., Zhang, X.-Q., and Wang, Y.-S. (2010). Fast response ultraviolet photoconductive detectors based on Ga-doped ZnO films grown by radio-frequency magnetron sputtering. *Appl. Surf. Sci.*, 257:921–924.

Sun, X., Wang, L., and Kwok, H. (2000). Improved ITO thin films with a thin ZnO buffer layer by sputtering. *Thin Solid Films*, 360:75–81.

Sundaresan, A. and Rao, C. N. R. (2009). Ferromagnetism as a universal feature of inorganic nanoparticles. *Nano Today*, 4:96–106.

Sutherland, R. L. (2003). *Hand book of Nonlinear Optics, Second edition*. Marcel Dekker Inc.

Swanepoel, R. (1983). Determination of the thickness and optical constants of amorphous silicon. *J. Phys. E:Sci. Instrum.*, 16:1214–1222.

Swanepoel, R. (1984). Determination of surface roughness and optical constants of inhomogeneous amorphous silicon films. *J. Phys. E: Sci. Instrum.*, 17:1214–1222.

Tan, S., Chen, B. J., Sun, X. W., Fan, W. J., Kwok, H., Zhang, X. H., and Chua, S. (2005). Blueshift of optical band gap in ZnO thin films grown by metal-organic chemical-vapor deposition. *J. Appl. Phys.*, 98:013505–013510.

Tauc, J. (1974). *Amorphous and Liquid Semiconductors*. Plenum Press, London.

Thyagarajan, K. and Ghatak, A. (2011). *Lasers: Fundamentals and Applications*. Springer.

Ting, J.-M. and Lin, C.-K. (2006). Characteristics of transparent conducting nanoscaled thin films based on ZnO. *J. Am. Ceramic Soc.*, 89:3676–3680.

van Dijiken, A., Meulenkamp, E. A., Vanmaekelbergh, D., and Meijerink, A. (2000). Identification of the transition responsible for the visible emission in ZnO using quantum size effects. *J. Lumin.*, 90:123–128.

Venkatachalam, S., Iida, Y., and (2008), Y. K. (2008). Preparation and characterization of Al doped ZnO thin films by PLD. *Superlattice. Microst.*, 44:127–135.

Wang, G., Kiehne, G. T., Wong, G. K. L., Ketterson, J. B., Liu, X., and Chang, R. P. H. (2002). Large second harmonic response in ZnO thin films. *Appl. Phys. Lett.*, 80:401–403.

Wang, H., Xu, M., Xu, J., Yang, L., and Zhou, S. (2010). Effects of annealing temperature and thickness on microstructure and properties of solgel derived multilayer Al-doped ZnO films. *J. Mater. Sci.: Mater. Electron.*, 21:145–148.

Wang, J. and Blau, W. J. (2009). Inorganic and hybrid nanostructures for optical limiting. *J. Opt. A: Pure Appl. Opt.*, 11:024001–024016.

Wang, M., Cheng, X., and Yang, J. (2009). Controlled visible photoluminescence of ZnO thin films prepared by RF magnetron sputtering. *Appl. Phys. A*, 96:783–787.

Wolf, S. and Tauber, R. (2000). *Silicon Processing for the VLSI Era*, volume 1 - Process Technology. Lattice Press, California.

Xie, R. G., Zhuang, J. Q., Wang, L. L., Yang, W. S., Wang, D. J., Li, T. J., and Yao, J. N. (2003). A WO_3/ZnO nanoparticle composite system with high photochromic performance. *Chem. J. Chinese U.*, 24:2086–2088.

Xu, H. Y., Liu, Y. C., Xu, C. S., , Liu, Y. X., Shao, C. L., and Mu, R. (2006). Structural, optical, and magnetic properties of Mn-doped ZnO thin film. *J. Chem. Phys.*, 124:074707.

Yan, W., Sun, Z., Liu, Q., Li, Z., Pan, Z., Wang, J., Wei, S., Wang, D., Zhou, Y., and Zhang, X. (2007). Zn vacancy induced room-temperature ferromagnetism in Mn-doped ZnO. *Appl. Phys. Lett.*, 91:062113.

Yassin, A., Ahmad, A., Shabeeb, G. M., Abdullah, A. Q., and 122, K. M. Z. K. M. . (2011). Z-scan measurements for the nonlinear absorption and the nonlinear refraction of poly 1,4-diazophenylene-bridged-tris(8-hydroxy-quinoline) aluminium (PDPAlq3). *Optik*, 122:1885–1889.

Ye, J., Gu, S., Zhu, S., Chen, T., Hu, L., Qin, F., Zhang, R., Shi, Y., and Zheng, Y. (2002). The growth and annealing of single crystalline ZnO films by low-pressure MOCVD. *J. Cryst. Growth*, 243:151–156.

Yim, K. and Lee, C. (2007). Dependence of the electrical and optical properties of sputter-deposited ZnO:Ga films on the annealing temperature, time and atmosphere. *J. Mater. Sci.:Mater. Electron.*, 18:385–390.

Yin, Z., Chen, N., Yang, F., Song, S., Chai, C., Zhong, J., Qian, H., and Kurash Ibrahim (2005). . 135, .-. (2005). Structural, magnetic properties and photoemission study of Ni-doped ZnO. *Solid State Commun.*, 135:430–435.

Yu, B., Zhu, C., Gan, F., and Huang, Y. (1997). Optical limiting properties of in_20_3 nanoparticles under cw laser illumination. *Opt. Mater.*, 7:103–107.

Zhang, D., Fan, P., Cai, X., Huang, J., Ru, L., Zheng, Z., Liang, G., and Huang, Y. (2009). Properties of ZnO thin films deposited by DC reactive magnetron sputtering under different plasma power. *Appl. Phys. A*, 97:437–441.

Zhang, J., Skomski, R., and Sellmyer, D. J. (2005). Sample preparation and annealing effects on the ferromagnetism in Mn-doped ZnO. *J. Appl. Phys.*, 97:10D303.

Zhang, W., Wang, H., Wong, K. S., Tang, Z. K., Wong, G. K., and Jain, R. (1999). Third-order optical nonlinearity in ZnO microcrystallite thin films. *Appl. Phys. Lett.*, 75:3321–3323.

Zhang, X., Fang, H., Tang, S., and Ji, W. (1997). Determination of two-photon-generated free-carrier lifetime in semiconductors by a single-beam Z-scan technique. *Appl. Phys. B-Lasers O*, 65:549–554.

Zhang, Y., Fa, W., Yang, F., Zheng, Z., and Zhang, P. (2010). Effect of annealing temperature on the structural and optical properties of ZnO thin films prepared by solgel method. *Ionics*, 16:815–820.

Zhu, S., Su, C. H., Lehouzky, S. L., Peters, P., and George, M. A. (2000). Pressure effects in ZnO films using off-axis sputtering deposition. *J. Cryst. Growth*, 211:106–110.

Zhuge, L. J., Wu, X. M., Wu, Z. F., Chen, X. M., and Meng, Y. D. (2009). Effect of defects on room-temperature ferromagnetism of Cr-doped Zno films. *Scripta Mater.*, 60:214–217.

Zidan, M. D., Allaf, A. W., Ajji, Z., and Alltabahham, A. (2010). Optical limiting behaviour of Sudan III dye doped polymer. *Opt. Laser Technol.*, 43:531–533.

Zou, C. W., Wang, H. J., Yin, M. L., Li, M., Liu, C. S., Guo, L. P., Fu, D. J., and Kang, T. W. (2010). Room temperature ferromagnetism and ferroelectricity behavior of (Cu, Li) co-doped ZnO films deposited by reactive magnetron sputtering. *J. Cryst. Growth,*, 312:906–909.

List of Publications

List of Publications Based on this Thesis

Refereed International Journals

1. **K. K. Nagaraja,** S. Pramodini, P. Poornesh and H. S. Nagaraja, “Effect of annealing on structural and nonlinear optical properties of ZnO thin films under cw regime”, **Journal of Physics D:Applied Physics** 46:055106 (2013)

2. **K. K. Nagaraja,** S. Pramodini, A. Santhosh Kumar, H. S. Nagaraja, P. Poornesh and Dhananjaya Kekuda (2012), “Third-order nonlinear optical properties of Mn doped ZnO thin films under CW laser illumination”, **Optical Materials** 35:431-439 (2012).

International Conference Proceedings

1. **K. K. Nagaraja,** A. Santhoshkumar H. S. Nagaraja, (2011), “Aluminum doped ZnO thin films by RF sputtering of coaxial ZnO and Al targets”, **AIP Conference Proceedings,** 1391:743-745

Presentations in Conferences

International

1. **K. K. Nagaraja,** H. S. Nagaraja “Optical and Structural Characterization of Sputtered ZnO Thin Films”, *International Conference on Advancement of Nanoscience and Nanotechnology,* March 1-3, 2010, Alagappa University, Tamil Nadu, India.

2. **K. K. Nagaraja,** A. Santhoshkumar and H. S. Nagaraja “Aluminum doped ZnO thin films by RF sputtering of coaxial ZnO and Al targets”, *Optics-11 ’A conference on light’,* May 23-25, 2011, NIT-Calicut, Kerala, India.

3. **K. K. Nagaraja,** A. Santhoshkumar and H. S. Nagaraja, “Fabrication and Characterization of ZnO/Al/ZnO Multilayers by Simultaneous DC and RF Magnetron Sputtering”, *International Conference on Materials Science and Technology*, June 10-14, 2012, Pala, Kerala, India.

4. **K. K. Nagaraja,** S. Pramodini, A. Santhosh Kumar, H. S. Nagaraja, P. Poornesh and Dhananjaya Kekuda, "Third-order nonlinear optical properties of Mn doped ZnO thin films under CW laser illumination", *International Conference Solid State Science and Technology*, December 18-20, 2012, University of Malaya, Malaysia.

National

1. **K. K. Nagaraja,** H. S.Nagaraja "Optical and Structural Properties of ZnO Thin Films Deposited by DC Reactive Sputtering", *National Conference on Multifunctional Nanomaterials and Nanocomposites, Feb 4-5, 2010,* Bharathihar University, Tamilnadu, India.

List of Other Publications

Refereed International Journals

1. *Third harmonic generation process in Al doped ZnO thin films*
   M. Abd-Lefdil, A. Douayar, A. Belayachi, A. H.Reshak, A.O. Fedorchuk, S. Pramodini, P. Poornesh, **K. K. Nagaraja**, H.S. Nagaraja
   Accepted for publication in **Journal of Alloys and Compounds** (2013).

2. *Effect of Sn doping on structural, optical, electrical and wettability properties of oriented ZnO nanorod arrays*
   A. Santhosh Kumar, **K. K. Nagaraja** and H. S. Nagaraja
   In press **Journal of Materials Science Materials in Electronics** (2013).

3. *Thermally induced nonlinear optical response and optical power limiting of acid blue 40 dye*
   Pramodini S., Poornesh P and **K. K. Nagaraja**
   Current Applied Physics 13:1175-1182 (2013).

4. *Magnetron sputtered MoO_3/carbon nanotube composite electrodes for electrochemical supercapacitor*
   L. S. Aravinda, **K. K. Nagaraja**, H. S. Nagaraja, K. Udaya Bhat and B. R. Bhat
   Journal of Electroanalytical Chemistry 699:2832 (2013).

5. *ZnO/carbon nanotube nanocomposite for high energy density supercapacitors*
   L. S. Aravinda, **K. K. Nagaraja**, H. S. Nagaraja, K. Udaya Bhat and B. R. Bhat
   Electrochimica Acta 95:119-124 (2013).

6. *Magnetic domain studies of cobalt nanostructures*
   H. S. Nagaraja, **K. K. Nagaraja,** F. Rossignol, F. Dumas-Bouchiat, C. Champeaux, A. Catherinot
   J. Supercond. Nov. Magn. 25:1901-1906 (2012).

7. *Conversion of microfiltration membrane into nanofiltration membrane by vapour phase deposition of aluminium for desalination application*
   Mahesh Padaki, Arun M. Isloor, **K. K. Nagaraja,** H. S. Nagaraja and Manjunatha Pattabi
   Desalination 274:177-181 (2011).

Conference Proceedings

1. *Growth and temperature dependent electrical properties of ZnO nanostructures*
   A. Santhoshkumar, **K. K. Nagaraja,** and H. S. Nagaraja
   Recent Advances in Materials Science **AIP Conf. Proc.,** 1536:263-264 (2013).

2. *Polymer assisted synthesis and characterization of fine* $ZnWO_4$
   A. Santhoshkumar, **K. K. Nagaraja,** and H. S. Nagaraja
   Advances in Nanoscience and Nanotechnology **Advanced Materials Research** 678:22-25 (2013).

Curriculum Vitae

Full Name: Nagaraja Kodihalli Kireeti

Date of Birth: 15-07-1982

Marital status: Single

Address: No. 1675/96, I Floor, Main Road,
KH Ranganatha Extn., Davangere-577 005.

E-mail: nrajkk@gmail.com; Mobile: 91-99869 65968

Research Interests

- Experimental condensed matter physics, thin films,
- Dilute ferromagnetism in ZnO, RF and DC magnetron sputtering

Education

2005-2007	M. Sc. Physics, Jnana Sahyadri, Kuvempu University-577 451, India.
2001-2004	B. Sc. Physics, DRM Science College, Davangere-577 004, India.

Professional experience

Temporary Lecturer, 2012 Aug-2012 Dec	NITK-Surathkal, Mangalore-575 025, India. Department: Physics; Courses: PG&UG Physics Lab and Tutorials
Lecturer, 2007 Sept - 2008 Aug	S D M Institute of Technology, Ujire-574 240, India . Department: Physics; Courses: Engineering Physics
Marketing Executive, 2004 Sept - 2005 July	Kopran Limited, Mumbai, India. Department: Pharmaceutical Sales